Title
Aspects of the Physical Control of Phytoplankton Dynamics over the Southern California Bight Continental Shelf

Author
Lucas, Andrew J.

Publication Date
2009

Peer reviewed

UNIVERSITY OF CALIFORNIA, SAN DIEGO

Aspects of the physical control of phytoplankton dynamics over the Southern California Bight continental shelf

A dissertation submitted in partial satisfaction of the
requirements for the degree
Doctor of Philosophy

in

Oceanography

by

Andrew J. Lucas

Committee in charge:

Peter J. S. Franks, Chair
John L. Largier
James Leichter
Robert Pinkel
William Propp
Clinton Winant

2009

The dissertation of Andrew J. Lucas is approved, and it is acceptable in quality and form for publication on microfilm and electronically:

_____

_____

_____

_____

_____

_____
Chair

University of California, San Diego

2009

DEDICATION

This dissertation is dedicated to the memory of

Dr. Larry C. Oglesby
Professor of Biology, Pomona College.

Naturalist, mentor, and friend.

TABLE OF CONTENTS

LIST OF FIGURES

LIST OF TABLES

ACKNOWLEDGEMENTS

Multidisciplinary projects require multidisciplinary expertise. This project—in the field, in the lab, and at the keyboard—benefited from the expertise of a group of talented people. Chris L. Dupont was a major contributor to all aspects of this study (particularly those that are wrong). He helped plan and execute the fieldwork and directed the laboratory studies. He served as either a sounding board or source for many of the novel contributions described in Chapters 2 and 3. He is an excellent scientist and close friend—his contribution to this project cannot be overstated.

Vera Tai performed the flow cytometry and qPCR enumerations of the picoplankton. Melissa Carter and John Hyde provided field and diving support, and Melissa assisted with qualitative assessment of phytoplankton species. Robert Combs was the tireless intern who worked very hard despite extremely poor compensation. John Largier and Linda Rasmussen provided instrumentation. The folks at the SIO hydraulics laboratory, in particular John Lyons and Charlie Coughran, provided critical field support and ad-hoc training.

The SIO graduate department funded a good portion of the field preparation. Thank you, Denise.

Dr. Robert Pinkel's Ocean Physics Group (OPG) provided Wirewalkers and field support. In particular, Jon Pompa, who apparently drew some sort of short straw, worked with me for six months before the experiment, fabricated Wirewalkers, designed and implemented data loggers, and successfully adapted a prototype instrument for prototype multidisciplinary science. He was a rock in the field and—although he almost cracked when I showed up at his house with a busted data logger just as he was leaving on vacation—he bore the indignity of my presence like a saint and a professional.

John Largier gave me an opportunity at SIO and shaped the direction that this dissertation took. He provided ideas, advice, field equipment and encouragement from up close and afar. He took me into his home, both in La Jolla and in Bodega Bay, and made me feel welcome and part of the family. I learned a lot from John, and I look forward the next stages of our collaboration.

Clint Winant provided excellent conversation... so much so, in fact, that it turned into Chapter 4. He encouraged me to explore the coastal ocean in a way that I would

not have otherwise. He wields his knowledge and intuition gently, which makes him a pleasure to learn from.

I am in debt to Peter Franks. He was a phenomenal advisor. He taught me valuable lessons about all aspects of science and academia. His dedication to the students of SIO is remarkable and I believe under-appreciated. I like to think he has become a great friend— and he is a man I completely respect. Thank you for everything, Peter.

Jim Leichter provided a detailed and in depth review of this dissertation, and provided valuable insight on the preparation of Chapter 2.

The California Department of Boating and Waterways supported the writing phase of this project through grants to Peter Franks. I would like to specifically acknowledge the support of Ron Flick.

To my parents for the support, love and understanding: you are officially no longer the worst parents in the Western Hemisphere.

Thanks go to my fellow students and colleagues at SIO, brilliant scientists and people: Matt Craig, Sarah Glaser, David Field, Justin Kulongowski (just don't get on a boat with him), Aurelian Ponte, Jim Behrens, and Randy Buccarelli. Joel Fodrie has been a frequent collaborator and I appreciate his friendship.

And finally to my beautiful and supportive girlfriend Krista— LYF.

Chapter 2, in part, is currently being prepared for submission for publication of the material. Lucas, AJ; Dupont, CL; Franks, PJS. The hose and the sprinkler: complementary roles of horizontal and vertical internal wave-induced nitrate flux over a narrow continental shelf. The dissertation author was the primary investigator and author of this material.

Chapter 3, in part, is currently being prepared for submission for publication of the material. Lucas, AJ; Dupont, CL; Largier, JL; Franks, PJS. The green ribbon: physical control of phytoplankton dynamics over a narrow continental shelf. The dissertation author was the primary investigator and author of this material.

Chapter 4, in part, is currently being prepared for submission for publication of the material. Lucas, AJ; The barotropic forcing of the baroclinic tide over the Southern California Bight inner shelf. The dissertation author was the primary investigator and author of this material.

VITA

1998	B.A. in Biology, Pomona College
2001–2002	Staff Research Assistant I Scripps Institution of Oceanography, University of California, San Diego
2002–2009	Research Assistant Scripps Institution of Oceanography, University of California, San Diego
2004	M.S., Biological Oceanography Scripps Institution of Oceanography, University of California, San Diego.
2009	Ph.D., Biological Oceanography Scripps Institution of Oceanography, University of California, San Diego.

PUBLICATIONS

Lucas, AJ, Guerrero RA, Mianzan H, Acha MA, Lasta C. 2005. Coastal oceanographic regimes of the Northern Argentine Continental Shelf. Estuarine, Coastal and Shelf Science. 65(3): 405–420.

Hsieh CH, Glaser SM, Lucas AJ, Sugihara, G. 2005. Distinguishing random environmental fluctuations from ecological catastrophes for the North Pacific Ocean. Nature. 435(7040): 336–340.

Fodrie FJ, Herzka SZ, Lucas AJ. 2007. Intraspecific density regulates positioning and feeding mode selection of the sand dollar Dendraster excentricus. Journal of Experimental Marine Biology and Ecology. 340(2): 169–183.

Fodrie, FJ, Levin, LA, Lucas, AJ. 2009. Role of population demography in evaluating the nursery function of juvenile habitats. Marine Ecology Progress Series. 385: 39–49.

ABSTRACT OF THE DISSERTATION

Aspects of the physical control of phytoplankton dynamics over the Southern California Bight continental shelf

by

Andrew J. Lucas

Doctor of Philosophy in Oceanography

University of California, San Diego, 2009

Peter J. S. Franks, Chair

Evidence gathered three decades ago showed persistently elevated total and new primary production over the continental shelf of the Southern California Bight. This dissertation examines the mechanisms that drive the flux of nitrate necessary to support the phytoplankton productivity over the shelf. Using results gathered from an intensive field experiment, I show that strong, persistent cross-shelf gradients in phytoplankton standing stock, primary productivity and community composition result from nitrate flux due to internal waves of tidal and higher frequency. I report the first estimates of the horizontal flux of nitrate due to the internal tide, and demonstrate that it is quantitatively similar to the nitrate demand of the inner shelf phytoplankton population. The local winds, contrary to expectations based on previous research, support a biologically-relevant tilt of the nitracline. Variability in the magnitude of the cross-shore shoaling of the nitracline in turn impacts the magnitude of the internal tide mediated nitrate flux. Remotely-forced large scale variability in the offshore depth of the nitracline controls the continental shelf 'nitrate climate.' During episodes of anomalously warm ocean temperatures, a correspondingly deep nitracline can shut off nitrate supply to the conti-

nental shelf, resulting in low phytoplankton biomass. During more typical conditions, the phytoplankton community over the inner shelf is dominated by taxa capable of rapid nitrate assimilation, while offshore waters have a proportionally greater amount of oligotrophic species. The results of this dissertation indicate that relatively small changes in the offshore depth of the nitracline could account for the long-term increase primary productivity and phytoplankton biomass noted by recent studies, even in the absence of increased local wind-forced upwelling. Finally, I examine the baroclinic semidiurnal variability in currents and water column structure in the shallow water of the inner shelf. The results of this analysis demonstrate that the behavior of the semidiurnal variability is not consistent with a propagating or standing low mode internal wave. Analyses of linearized momentum balances suggest that the semidiurnal variability may result from the interaction of barotropic tidal flow, friction in the bottom boundary layer, and rotation.

1 Introduction to the Dissertation

Perhaps the most challenging aspect of understanding variability in biological processes is associating detected changes with the environmental forcing responsible.
M.J. Behrenfeld et al. 2006

The research that comprises this dissertation investigated two fundamental questions about the coastal ecosystem in the Southern California Bight (SCB): 1) What physical mechanisms control the availability of the limiting inorganic phytoplankton nutrient, nitrate, over the SCB continental shelf? and 2) What is the relationship between phytoplankton dynamics and the variability in physically-mediated nutrient delivery across a range of spatial and temporal scales?

These questions were motivated by long-standing observations in the southern SCB (SSCB, the region between the Palos Verdes Peninsula and the United State-Mexico border (Mullin 1986)) over the past 40 years. Much progress towards understanding the coupling between physical forcing and phytoplankton response in the SSCB was made in the period between the late 1970s and early 1990s, primarily through field work undertaken by the Food Chain Research Group of SIO during the Southern California Bight Study (1974-1983, SCBS, Eppley 1986, 1992, among many others). Since that time, the investigation of phytoplankton productivity in the SSCB has remained largely dormant.

1.1 Background

The ocean ecosystem is almost entirely fueled by the photosynthetic activity of free-living marine autotrophs, collectively called phytoplankton. The productivity of the

phytoplankton—typically quantified as the rate of carbon fixation [g C L^{-3} T^{-1}]— is in turn controlled by the availability of light and the elements necessary for the photosynthetic fixation of inorganic carbon: the macronutrients nitrogen, phosphorous, and silica, and the micronutrients, including trace metals. Phytoplankton draw these nutrients from two general sources: the organic ('recycled') pool and the inorganic ('new') pool. In the case of nitrogen, the organic forms include ammonia, urea, and amino acids which are excreted directly or recycled by microbial activity within the euphotic zone. The primary inorganic form of nitrogen, nitrate (NO_3^-), is formed by light-inhibited microbial degradation of organic material below the euphotic zone.

In much of the ocean—including the SSCB— phytoplankton productivity is limited by the availability of fixed nitrogen (Dugdale 1967, Eppley et al. 1979, Cullen et al. 1983, Barber and Chavez 1991, Eppley 1992, Falkowski et al. 1998). The total phytoplankton productivity in such systems is the sum of productivity due to recycled organic nitrogen and 'new' productivity due to the supply of nitrate (Dugdale and Goering 1967). The availability of nitrate depends on the physical delivery of deep nitrate-rich water into the euphotic zone (Eppley and Peterson 1979). At steady state, the amount of organic material that is removed from the phytoplankton system (through sinking or transfer to higher trophic levels) is equal to proportion of total phytoplankton productivity due to the input of inorganic nutrients (i.e. from outside the system) (Dugdale and Goering 1967). Therefore the physical mechanisms that mediate the delivery of inorganic nutrients in turn set the realizable productivity of higher trophic levels (e.g. Eppley and Peterson 1979) and act as a primary regulator of the atmospheric – ocean carbon dioxide flux (e.g. Cermeño et al. 2008).

In a seminal study, Eppley and Peterson (1979) showed that there was a robust relationship between total and new productivity. As the rate and magnitude of inorganic nitrate delivery increases, both total productivity (new plus recycled productivity) and the ratio of new : total productivity (called the f-ratio) increases. Therefore the most productive areas of the world's ocean are characterized by strong physical forcing which deliver large amounts of inorganic nitrogen. This schematic understanding of the relationship between physical mediated nutrient delivery and photosynthetic productivity, as shown in Fig. 2 of Eppley and Peterson (1979), is taught in all introductory

biological oceanography classes.

Significantly, that figure was drawn omitting data from the SCB continental shelf (depths < 200 m) as "they often fall below the line drawn in Fig. 2," even as Eppley himself had collected a vast number of SCB observations (Eppley and Peterson, 1979). The measurements of new : total productivity over the SCB shelf indicated that, although total productivity was relatively large, new productivity was smaller than expected based observations in other high productivity systems.

In the late 1970s it was not known what physical process was responsible for maintaining the high productivity of the SCB continental shelf (Eppley et al. 1979). Work being carried out by coastal physical oceanographers at roughly the same time showed that the dominant variability in SCB continental shelf currents and water column structure was due to internal waves of a range of frequencies, and that the local wind was only weakly correlated with low-frequency currents (Winant and Olson 1976, Winant and Bratkovich 1981). Eppley et al. (1979) noted a persistent tilt in the nitracline across the shelf, and showed that the depth of the nitracline was correlated to the vertically integrated primary productivity. The view arose that, unlike highly productive coastal ecosystem found elsewhere, the productivity of the SCB coastal region was not due to upwelling forced by the local winds or terrigenous runoff (Eppley and Holm-Hanson 1986). Instead, productivity was controlled by 1) whatever physical process set the depth and cross-shore tilt of the thermocline and 2) the hypothesized transport of nitrate by the ubiquitous, energetic, and presumably breaking internal waves, as had been postulated as early as 1947 (Cooper 1947).

1.2 The physical environment of the SSCB

The SSCB is an interesting example of a weakly-forced system from an oceanographic perspective. It is not under the influence of the vigorous upwelling favorable winds that characterize the majority of the California Current System and that drive strong upwelling off Central Baja California (Winant and Dorman 1997). Continental run-off is sporadic and generally absent during times of peak productivity (Eppley 1992). Nevertheless, even in the absence of mechanisms that dominate phytoplank-

ton productivity elsewhere, there is a region of elevated chlorophyll concentration and primary productivity over the SSCB shelf apparent in both satellite and in situ measurements (Eppley and Holm-Hansen 1986, Eppley 1992). This enhanced chlorophyll concentrations and primary productivity inshore of the shelf break must be a function of elevated nitrate flux to the surface waters over the shelf (Eppley 1992).

A number of studies of SSCB physical forcing demonstrate the lack of correlation between local winds and subinertial currents and temperature (e.g. Winant and Olson 1976, Winant and Bratkovich 1981, Pringle and Riser 2003). During stratified periods (April to November), the variability in the density and the current structure of the water column over the SSCB shelf is dominated by the internal wave field at frequencies from the inertial period to the local buoyancy frequency (e.g. Winant 1974, Winant and Bratkovich 1981, Lerczak 2000, Boehm et al. 2002, Lerczak et al. 2003). In stratified summer months, the baroclinic semidiurnal internal tide forces large vertical excursions of the pycnocline (>15 m in depths < 30 m), vertically sheared alongshore currents, and cross-shore currents that are 180° out of phase above and below the pycnocline (Lerczak et al. 2003). These currents are more energetic than currents at any other frequency, and are intensified over the shelf (Lerczak et al. 2003).

Associated with the internal tide, packets of strongly nonlinear high frequency internal waves (HFIWs) propagate across the shelf. These HFIWs have been implicated in the transport of meroplanktonic larvae (Shanks 1983, Pineda 1991, Scotti and Pineda 2007), the accumulation of phytoplankton (Lennert-Cody and Franks 1999), and have been shown to dissipate across the shelf, losing energy to diapycnal mixing (Lerczak 2000, Moum et al. 2007). The role of dissipating or breaking HFIWs as a nutrient pump to the euphotic zone was originally postulated over 60 years ago (Cooper 1947), and a number of field observations and numerical models since have pointed to the importance of episodic injection of nutrients into the euphotic zone by HFIWs (see Eccles 1962, Sandstrom and Elliot 1984, Holligan et al. 1985, Sandstrom and Oakey 1995, Leichter and Miller 1999, MacIntyre et al. 2001, Leichter et al. 1996, 2003, Sharples et al. 2001, 2007, Sharples 2008).

There is good evidence linking the internal tide and high frequency internal waves to primary productivity in a number of shelf seas around the world. For ex-

ample, Sharples et al. 2001 estimated that the dissipation of energy from the internal tide leads to relatively strong mixing (4-7 x 10^{-4} m^2 s^{-1}) and a diapycnal flux of nitrate of approximately 12 mmol N m^{-2} d^{-1}, contributing an estimated 100 g C m^{-2} annually to the shelf northeast of New Zealand. The baroclinic tide has been shown to influence primary productivity and phytoplankton community composition in the Celtic Sea (Pingree and Martel 1981, Sharples et al. 2007) and was implicated in nitrate delivery and primary productivity over the South African shelf (Largier 1994).

Since the work of Eppley and his collaborators was abandoned, advances in oceanographic technology revolutionized our ability to directly and quantitatively assess hypotheses regarding nutrient fluxes in the context of internal wave variability. We therefore designed a field experiment meant to examine the cross-shore variability in the physical dynamics hypothesized to control nitrate fluxes, while concurrently assessing the total and nitrate-derived productivity and the composition of the phytoplankton community across the shelf.

1.3 The Inner-shelf Productivity eXperiment (ISPX)

In the summer of 2006, I set about investigating the physical variability over the SSCB inner shelf in the context of cross-shelf gradients in new and total productivity and phytoplankton community structure. This work was undertaken with collaborators from SIO, and focused on providing the resolution necessary to elucidate the internal tide and high-frequency internal wave processes we hypothesized controlled nitrate flux to the shelf euphotic zone.

The ISPX design was informed by a pilot study I conducted in the summer of 2004, which utilized a prototype autonomous profiling system—called the Wirewalker (WW)—developed by R. Pinkel and the Ocean Physics Group at SIO (Rainville and Pinkel 2001). The results of the pilot study indicated that a densely spaced array of bottom-mounted current meters and the WW platform were capable of resolving the strong internal wave variability on the appropriate spatial and temporal scales necessary to make quantitative estimates of energy flux, dissipation and ultimately nitrate flux across the inner shelf.

The results of the pilot study motivated a number of attempts to secure funding for a more intensive field effort. Proposals were submitted to the Office of Naval Research and the National Science Foundation which, despite strong reviews, were not funded. The ISPX program was therefore completed on a very small budget, utilizing the resources made available to students by SIO and drawing from a number of different sources of equipment, expertise and money.

1.3.1 ISPX design

The ISPX study took place between 1 August 2006 and 24 August 2006 off Mission Beach, CA (Fig 2.1), and was comprised of three inter-related field and laboratory approaches, including: 1) a 24 day mooring deployment of acoustic Doppler current profilers (ADCPs), thermistors, and two WWs equipped with conductivity, temperature and depth sensors (CTDs) and fluorometers; 2) transects across the continental shelf and slope to profile with a CTD, fluorometer and in situ ultraviolet spectrophotometer nitrate sensor (ISUS) and to collect water at the surface and chlorophyll maximum using a 10 L Niskin bottle; and 3) laboratory studies, including radioisotope-labeled (^{14}C) primary productivity measurements, stable-isotope (^{15}N) nitrogen uptake experiments, pigment analysis using high-performance liquid chromatography (HPLC), cell enumeration using flow cytometric analysis, and finally traditional nutrient and chlorophyll measurements.

The mooring array that we occupied in 2006 was on the same line as the inner shelf moorings in the1996-1997 IWAVES study described in Lerczak (2000). The continental shelf is this region is characterized by simple, although steep, bathymetry with bathymetric contours running only a few degrees off of a north-south line (Fig 2.1). The simplicity in bathymetry aids the interpretation of the internal variability.

1.3.2 The structure and variability of inner shelf currents: ADCP moorings

The ISPX mooring array was designed to provide detailed cross-shore and vertical resolution of currents over the inner shelf. Five bottom-mounted Acoustic Doppler

Current Profilers (ADCPs) were deployed in 32, 22, 17, 12 and 7 m depths (below MLLW) over 24 days, and were configured for 15 s sampling at 3 vertical resolutions: 1 m (32 m and 22 m ADCPs), 0.5 m (17 m ADCP) to 25 cm (12 and 6 m ADCPs). Each ADCP was mounted on a diver-deployed sea-spider (an ADCP mooring platform) modified to accommodate a SBE MicroCat conductivity and temperature sensor, configured to report an ensemble-averaged sample every 15 s (5 samples). At the 6 m mooring, a SIO temperature logger was used in place of a MicroCat.

1.3.3 The structure and variability of density and fluorescence: Wirewalker moorings

The WW wave-powered autonomous profiler, developed at SIO by R. Pinkel and colleagues, uses the surface wind-wave field to power vertical profiling (Rainville and Pinkel 2001). The WWs are a simple and robust tool to study evolving small-scale vertical distributions of physical and biological variables. We deployed 2 WWs, at 22 and 12m, in association with ADCP/MC installations, equipped with Seabird 49 (FastCat) CTDs and Turner Designs Cyclops 7 fluorometers. The WWs sampled the upper 18.5 m and 9 m of the water column at the outer and inner WW moorings, respectively. The watch circle of the profilers had a diameter of approximately twice the water depth (40 and 25 m, respectively). Given the beam angle of the ADCPs and the WW watch circles, the WWs were moored 150 m to the north of the associated ADCP/MC installation to avoid instrument interference. Profile frequency depended on depth (and only weakly on the surface wave field); profile frequency at each mooring was essentially constant at each mooring over the length of the deployment, with 3.5 minute profile interval at the 22 m WW and a 2.5 minute profile interval at the 12 m WW. Over the course of the 3 week period, 10,301 individual profiles were collected at the 22 m WW and 10,665 individual profiles were collected at the 12 m WW (Table 1.1). The 16 Hz sample rate of the CTD and upcast velocity of the WW allowed for a maximum vertical resolution of ~ 3 cm. The data collected by the WWs are the best vertically and temorally resolved time series of concurrent water column structure and fluorescence measurements ever collected in the SCB, and perhaps anywhere.

Given battery limitations, the 3-week deployment included 2 scheduled turn-

around periods, which resulted in pre-planned gaps in water column coverage. Profiling and data acquisition were unfortunately not perfect between scheduled turn-around periods, and unplanned data gaps therefore exist in the final time series. The inner WW in particular had a number of major gaps.

1.3.4 Cross-shelf biological and physical variability: CTD transects and water sampling

The CTD, a Seabird 19plus, was equipped with a Turner Designs fluorometer and Satlantic ISUS v.2. We conducted 7 cross-shelf CTD transects between 9-August-2006 and 17-August-2006. On non-biological sampling days (9-August-2006, 10-August-2006, 15-August-2006, 16-August-2006), we occupied 8 stations between the shelf slope and the inner shelf, with approximately 1.5 km between stations. The maximum depth of each profile was approximately 90 m.

On three of the seven transects (11-August-2006, 14-August-2006, 17-August-2006), we sampled water at the surface and chlorophyll maximum (as determined by the live-wired CTD system) occurred at four stations. The sampling pattern was designed to span from the continental slope to the inner shelf, where we expected to find strong gradients in phytoplankton community composition, biomass, primary productivity and new production. On 11 and 17 August 2006, we collected water samples from the surface and subsurface chlorophyll maximum at four stations along a cross-shore transect from the slope to the inner shelf (bottom depths of 400, 100, 65, and 25 m). On 14 August 2006, we occupied a tightly spaced transect across the shelf (bottom depths of 65, 50, 25 and 15 m), intended to investigate gradients across the narrow continental shelf. The total length of each transect was $\sim$15 km on the 11 and 17 August 2006 and was $\sim$5 km on the 14 August 2006.

1.4 Outline of the Dissertation

The data gathered during ISPX permitted an analysis of the close coupling between the composition and vital rates of the phytoplankton community and spatiotemporal variability in the physically mediated delivery of nitrate. In Chapter 2, I present

an analysis of the nitrate flux to the inner shelf euphotic zone mediated by internal waves of tidal and higher frequencies. I show that the vertically integrated energy and nitrate fluxes are onshore, dictating that sinks exist over the inner shelf for both quantities. Energy is lost by mixing, and nitrate is taken up by the phytoplankton, leading to the persistent elevation of new and total productivity over the inner shelf. Estimates of nitrate flux forced by the tide compare well with our estimates of phytoplanktonic nitrate uptake based on laboratory experiments. We explicitly consider the separation between the vertical flux of nitrate, typically considered the important flux pathway, and the horizontal flux of nitrate due to the internal tide, which has not been previously examined. The enhanced importance of nitrate flux to the surface waters inshore, reflected in the surface new productivity gradients, implies that the internal tide-driven horizontal flux of nitrate is being redistributed vertically. Simple estimates of mixing based on the loss of kinetic energy across the ADCP array show that a portion of the horizontal flux is mixed upwards. The horizontal flux is essentially along-isopycnal, which, at the scale of the shelf, implies a vertical redistribution of nitrate due to the persistent onshore shoaling of the isopycnals. It appears that the onshore transport and vertical redistribution of nitrate by internal wave processes maintains the gradients in productivity observed over the SSCB shelf (Eppley 1992).

In Chapter 3, I show that the gradients in total and new productivity across the shelf are concurrent with changes in the composition of the phytoplankton community towards taxa typical of areas with moderately high levels of nitrate input. In both the surface waters and at the subsurface chlorophyll maximum, the vital rates and character of the phytoplankton community are quite different over the relatively short spatial scale of the shelf ($\sim$10 km). The internal wave mediated nitrate flux discussed in Chapter 2 appears in general to support these gradients. However, physical context of these internal wave processes can lead to large changes in the potential for nitrate flux. The local alongshore wind is well correlated with the vertical shear in subinertial alongshore velocity that balances the persistent tilt in the pycnocline and nitracline. This wind is too weak to cause large across-shelf transports—particularly given the strong onshore sea breeze—and therefore does not support the observed biological gradients alone. Instead, it acts to set up the isopycnals, thereby enhancing the biological impact of the along-

isopycnal internal wave-mediated nitrate flux. There are also large changes in the depth of the nitracline at the shelf break which are not related to local forcing. I show that this remotely-forced variability can drastically alter the nitrate climate over the shelf. For example, a re-analysis of historical records indicates that during prolonged periods of anomalously warm temperatures (e.g. El Niño events), the depression of the nitracline at the shelf edge shuts of the supply of nitrate to shelf and leads to exceptionally low standing stocks of phytoplankton.

The integrated view presented in Chapter 3 identifies the physical mechanisms responsible for the productivity and community composition of the SSCB continental shelf phytoplankton, an open issue since the 1980s (Eppley 1992). Moreover, I demonstrate that the subtle interaction across different scales of physical variability combine to establish the biological character of the phytoplankton over the SSCB shelf.

In Chapter 4, I address the nature of the semidiurnal variability over the inner shelf. I show that, contrary to previous interpretations, the semidiurnal variability in waters < 20 m appears not to result from a propagating or standing low mode internal wave, based on the sense of rotation of the baroclinic semidiurnal currents. Instead, in these shallow waters, it appears to be driven by the barotropic tide directly. I assess simplified alongshore and across-shore momentum balances, and show the importance of rotation, friction, and the cross-shore and along-shore gradients in sea level. The baroclinic semidiurnal variability behaves in a manner similar to a recent theoretical model of tidal circulation in an estuary (Winant 2007, 2008), where the cross-shelf flow is driven by an imbalance between the forcing of the cross-shelf sea level gradient and the Coriolis force associated with the vertically sheared alongshore transport. The observations do not exactly fit the theory as developed here, and further field and model investigation is required to conclusively assess the validity of this hypothesis. However, if validated, it would be a novel description of the internal tide in shallow continental seas. The view of the internal tide presented here is of a bottom boundary layer-driven frictional process. The commonly occuring coincidence of the interaction of the nitracline and bottom boundary layer over the inner shelf would act to enhance the vertical flux of nitrate.

Finally, in Chapter 5, I provide final remarks on the broader context of the ma-

jor findings of ISPX and then briefly discuss potentially fruitful future directions for research linking the physical dynamics of nutrient flux and the phytoplankton in system such as the Southern California Bight.

Table 1.1: Sampling statistics from the ISPX WW deployment, August 3 to Aug 23, 2006.

Mooring	Wire length (m)	# of profiles	Average downcast (sec)	Average upcast (sec)	Average upcast velocity (cm/s)	Native vert. resolution (cm)
22 m WW	18.5	10,301	204	45	40	2.5
12 m WW	9	10,665	102	30	27	1.7

2 The hose and the sprinkler: Complementary roles of horizontal and vertical internal wave-forced nitrate flux over a narrow continental shelf

2.1 Abstract

We used a technique adapted from internal wave energy flux measurements to estimate the horizontal, along-isopycnal flux of nitrate over the continental shelf of the Southern California Bight due to internal waves of tidal frequency (the internal tide). The magnitude of the internal tide flux was capable of supporting, on average, all the 'new' primary productivity found there. Moreover, we showed that the along-isopycnal, internal tide-driven flux is quite variable in time, potentially accounting for 0-1800 mg C m^{-2} d^{-1} (mean $\sim$450 mg C m^{-2} d^{-1}) of new productivity (NP), depending on the strength of the internal tide and the nitrate climate. The cross-shelf dissipation of high-frequency internal waves was also capable of driving a significant vertical, diapycnal flux of nitrate into the euphotic zone ($\sim$35 mg N $m^{-2}d^{-1}$, NP = $\sim$135 mg C m^{-2} d^{-1}). On occasion, the complementary modes of along and across isopycnal nitrate flux relaxed the nitrate limitation on the inner shelf phytoplankton community, leading to a rapid increase in phytoplankton concentration. At other times, weak internal wave forcing, in combination with anomalously warm, low-nitrate waters over the shelf, had the potential to shut off the supply of nitrate to the shelf. Based on the evidence presented

here, we expect that the combination of horizontal, internal tide-driven nitrate flux and vertical, high-frequency internal wave-driven nitrate flux are the sources of the persistently elevated narrow band of increased chlorophyll concentrations over the Southern California Bight shelf, apparent in satellite images and in situ data.

2.2 Introduction

In nutrient-limited oceanic environments, the rate of nutrient supply—mediated by physical processes—influences the rate of phytoplankton productivity. Nutrient supply to the euphotic zone can be separated into two categories: 1) advective, along-isopycnal fluxes and 2) mixing-driven, diapycnal fluxes. Along-isopycnal length scales in the ocean are typically 2 or 3 orders of magnitude greater than diapycnal length scales. Correspondingly, advective nutrient supply (e.g. from wind-forced upwelling) is typically stronger than mixing-driven (and ultimately turbulent) diapycnal nutrient supply, such as that from tidal mixing or breaking, nonlinear internal waves.

Internal waves of tidal frequency (the internal tide, IT) are often more energetic than internal waves at other frequencies, and mixing due to the dissipation of IT energy has been invoked as a significant driver of nutrient flux in a number of settings (Sharples et al. 2001, 2007, MacIntyre et al. 2001, Leichter et al. 2003, among others). The IT loses energy by nonlinear steepening and scattering into higher vertical and horizontal wave numbers, shedding high-frequency nonlinear internal waves, and eventually to irreversible mixing (Inall et al. 2000, Helfrich and Grimshaw 2008, Helfrich 2008). Typically, this mixing results in a vertical redistribution of mass and scalar properties. The view of IT dissipation as a vertical, diapycnal process naturally gave rise to corresponding effort to quantify the resulting vertical diapycnal flux of nutrients. Nevertheless, along-isopycnal fluxes of scalar quantities can occur in the absence of mixing, given a horizontal gradient in the uptake of the scalar. Therefore, more completely, the nutrient flux due to the internal tide consists of a diapycnal component due to mixing and an along-isopycnal component due to advection. The purpose of this study is to examine the relative impacts of along-isopycnal and diapycnal nitrate flux on phytoplankton productivity over the steep, narrow continental shelf of the Southern

California Bight (SCB). The SSCB is an ideal laboratory to study internal wave-induced fluxes—local wind forcing is weak and uncorrelated with subinertial currents (Winant and Olson 1976, Winant and Dorman 1997, Pringle and Riser 2003) and continental run-off is largely absent during the stratified and productive summer months (Eppley 1992). The internal tide and high-frequency internal waves are very energetic (Lerczak 2000, Lerczak et al. 2003) and have been implicated in the nutrient budget of the SCB by previous studies (Cooper 1947, Armstrong and LaFond 1966, Cullen et al. 1983).

2.2.1 Nutrient flux in internal-wave forced systems

A key distinction exists between horizontal and vertical fluxes of nutrients in internal wave-dominated systems. Typically, horizontal fluxes are not calculated (however, see McPhee-Shaw et al. 2007), and the diapycnal, vertical flux of nutrients through the base of the euphotic zone is assumed to control new productivity in the nutrient-limited surface waters. In many cases, this assumption is correct; however, at coastal boundaries where horizontal fluxes must go to zero, the resulting flux convergence dictates that nutrients must either build up over the inner shelf, or that a nutrient sink (i.e. phytoplankton uptake) must be present. Moreover, in regions with sloping isopycnals, along-isopycnal nutrient flux can bring nutrients into the euphotic zone, leading to increased new productivity in the absence of diapycnal mixing. This is one important cause of elevated new and total primary productivity within cold-core and mode water open-ocean eddies, for example (McGillicuddy et al. 2007, although see Ledwell et al. 2008 for a discussion of the role of diapycnal fluxes in those features).

Internal wave-induced fluxes have long been considered vertical mixing phenomena, due, for example, to the breaking of highly nonlinear internal waves or the interaction of baroclinic currents with the bottom (references above, MacIntyre et al. 1999, McPhee-Shaw and Kunze 2002, Moum et al. 2003). Diapycnal nutrient fluxes are typically quantified by estimating the intensity of the vertical mixing (as represented by the vertical coefficient of eddy diffusivity, K_z), estimating the vertical gradient of nutrients, and calculating the vertical nutrient flux as a product of those two quantities quantity (in the case of nitrate, $N_{flux} = K_z \frac{\partial [NO_3^-]}{\partial z}$).

A great deal of effort has focused on estimating the value of K_z in a number

of contexts, typically parameterized as the ratio of the dissipation of turbulent kinetic energy (ε) to stratification (N^2), multiplied by a constant mixing efficiency (Osborn 1980). Dissipation is estimated with 1) free-fall microstructure profilers or 2) from the convergence of energy flux. Free-fall microstructure measurements have the advantage of excellent vertical resolution, direct measurement of turbulent kinetic energy, and can be performed in concert with vertical nitrate profiles to provide spatially and temporally collocated estimates of K_z and the vertical gradient of nitrate (e.g. Sharples et al. 2007). However, mixing is episodic in space and time, and the temporal and spatial resolution of microstructure surveys are limited by logistics.

In contrast, a flux convergence approach uses time series of vertically resolved currents and density to estimate the change of internal wave energy across an array of moorings. Estimates of dissipation and mixing due to the convergence of energy flux have the advantage of extending for long periods of time relative to ship-based microstructure surveys and therefore account for both episodic periods of energetic mixing and more common quiescent periods. However, the estimate of dissipation calculated from the convergence of internal wave energy is an average over the domain encompassed by the mooring array. Nitrate flux calculated from these area-averaged dissipation estimates are difficult interpret as the biologically important quantity is actually the flux of nitrate into the euphotic zone.

Diapycnal nitrate flux acts to support primary productivity when nitrate is a limiting nutrient. The quantity of primary productivity supported by a particular nitrate flux—measured in grams of carbon per unit space per unit time— is most commonly calculated via the Redfield ratio, which is the fundamental measure of the quantity of carbon to nitrogen in phytoplankton. Estimates of nitrate flux and Redfield-scaled primary productivity from both flux convergence and microstructure survey techniques suggest that, regardless of the specific limitations of each approach, both appear to provide reasonable estimates of diapycnal nitrate flux (Sharples et al. 2001, 2007).

Below we describe an approach to directly estimate the horizontal, cross-shelf flux of nitrate due to the baroclinic internal tide adapted from recently developed methods to quantify internal wave energy flux (Kunze et al. 2002, Nash et al. 2005). We show that this horizontal (essentially along-isopycnal) flux of nitrate is capable of supporting

all of the 'new' primary productivity (sensu Dugdale and Goering 1967) over the narrow continental shelf of the southern portion of the Southern California Bight. In concert with the along-isopycnal nitrate flux due to the internal tide, significant diapycnal nitrate flux is forced by the dissipation of high-frequency internal waves. This diapycnal flux is alone capable of supporting approximately 25% of the measured primary productivity. Concurrent profiles of fluorescence from an autonomous wave-driven profiler show fluorescence at both the subsurface chlorophyll maximum and in the surface waters responds to the variable internal tide-driven nitrate flux. We envision that inner shelf primary productivity in the southern SCB (SSCB) is controlled by the complementary pathways of along- and across-isopycnal transport ultimately driven by the internal tide.

2.3 Experiment

The Inner Shelf Productivity eXperiment (ISPX) study took place between 1 August 2008 and 24 August 2008 off Mission Beach, CA, and was comprised of three inter-related field and laboratory approaches: 1) a 24 day mooring deployment of bottom mounted ADCPs and an autonomous, wave-driven Wirewalker profiler (WW) equipped with a conductivity, temperature and depth sensor (CTD) and fluorometer; 2) transects across the continental shelf and slope to profile with a CTD, fluorometer and in situ ultraviolet spectrophotometric nitrate sensor (ISUS, Johnson and Coletti 2002) and to collect water at the surface and chlorophyll maximum for laboratory studies; and 3) laboratory studies, including radioisotope-labeled (^{14}C) primary productivity measurements, stable-isotope (^{15}N) nitrogen uptake experiments, and nutrient and chlorophyll measurements.

2.3.1 Primary productivity and nitrogen uptake experiments

From a biological perspective, we aimed to investigate the strong across-shore gradient of surface chlorophyll often apparent in satellite images and in situ measurements (e.g. Eppley et al. 1979, Eppley 1992) and to assess whether those gradients were associated with increased total primary productivity and increased new productivity, which would require an enhanced, physically mediated nitrate delivery over the

inner shelf relative to offshore waters (see Eppley et al. 1979).

We conducted 7 cross-shelf CTD transects between 9-August-2006 and 17-August-2006. The CTD, a Seabird 19plus, equipped with a Turner Designs fluorometer and Satlantic ISUS v.2, was deployed by hand off a small boat. On three of the seven transects (11-August-2006, 14-August-2006, 17-August-2006), we sampled water at the surface and chlorophyll maximum at four stations (see Fig. 2.1 for sample locations).

For each sample, we determined primary productivity via radiotracer ^{14}C-labeled bicarbonate (HCO_3^-), based on the JGOFS protocol, in 2 hour incubations at 25% and 2% surface irradiance for the surface and chlorophyll maximum, respectively. In addition, we assessed the uptake of nitrate, ammonium, and urea with 2 hour incubations at the same light levels (Chapter 3). The relative importance of inorganic ('new') and organic ('recycled') sources of nitrogen to phytoplankton communities, the f-ratio, was calculated as the uptake rate of nitrate divided by the sum of uptake rates for all three compounds, allowing us to estimate 'new' primary productivity.

We vertically integrated the uptake rate of radiotracer-labeled carbon at the surface and chlorophyll maximum to form an estimate of water column productivity (in units of mg C m^{-2} d^{-1}) by assuming a euphotic zone depth of 20 m at all stations (consistent with Secchi disc observations), and assuming that the surface value represented the primary productivity of the surface waters (taken to be 15 m) and the chlorophyll maximum sample represented the primary productivity of the deeper 5 m of the euphotic zone. Two hour incubations were extended to 12 h (daylight) estimates, and then multiplied by a conversion factor of 1.8 (Eppley 1992), to estimate daily total productivity (for comparison to CalCOFI values). Integrated new productivity was calculated by using f-ratio measurements to estimate new productivity at the surface and chlorophyll maximum with subsequent integration as above. The vertically integrated value of primary productivity suffers from a number of uncertainties—most importantly the lack of vertical resolution—and care should be taken when comparing these values with other studies. However, the differences among sampling days, the spatial gradients, and, to a large extent, the value of integrated primary productivity, are not sensitive to the exact integration scheme. Therefore we expect that differences among the samples reported here are real, and thus the spatial and temporal gradients in the measurements represent

the natural variability of the system. Moreover, the patterns in those quantities are consistent with previously published results in the study area (Eppley et al. 1979, Eppley and Holm-Hansen 1986, Eppley 1992).

2.3.2 Wirewalker (WW) and ADCP moorings

The ISPX mooring array was designed to provide detailed cross-shore and vertical resolution of currents and density structure over the inner shelf (32 to 7 m, Fig. 2.1). Currents were rotated individually at each mooring, according to local bathymetry (National Ocean Service Hydrographic Data Base). Rotations were all in the clockwise sense between 6° and 11° (6°, 32 m; 7°, 22 m; 11°, 16 m; 9°, 12 m; 6°, 7 m).

The WW wave-powered autonomous profiler uses the surface wave field to power vertical profiling (Rainville and Pinkel 2001). We deployed a WW at 22 m, in association with an ADCP (Fig. 2.1). The WW sampled the upper 19.5 m of the water column (relative to the surface). The 3 week WW deployment included 2 scheduled turn-around periods; however, unplanned data gaps exist in the final time series. These gaps were short relative to the semidiurnal time scale and were interpolated using a low-pass interpolation scheme. This approach does not significantly impact the nature of the tidal signature in density or estimated nitrate.

The WW was suspended from a float, and always sampled a fixed depth range relative to the surface, which must be less than the depth range at the mooring at the lowest tide during the deployment. The bottom-mounted ADCP data were sampled in depth intervals relative to the bottom (meters above bottom, MAB). In order to provide collocated observations, the WW profiles were shifted from a free-surface frame of reference to a MAB frame of reference by utilizing the ADCP pressure sensor to 'de-tide' the WW profiles. Finally, by interpolating from the deepest MAB-frame of reference WW sampling point of each profile to the ADCP-mounted conductivity/temperature sensor (always < 4 m of interpolation), we produced full depth profiles of temperature, salinity and density with the same time and depth intervals as the ADCP data.

We did not measure nitrate concentrations directly at the WW mooring. However, given the strong relationship between nitrate and temperature in the SSCB (Fig. 2.2), we created a reconstructed nitrate time series ($N(z,t)$) from WW temperature

profiles by a modified linear fit between nitrate and temperature as determined by the ISUS/CTD package (n=56 stations, Fig. 2.2). Nitrate was nearly undetectable in bottle samples (< 0.1 μmol L^{-1}) at any temperature above 14.5 °C, and was certainly well-below the ISUS detection limit at those temperatures, so nitrate concentration was fit to temperature as:

$$\left[NO_3^-\right] = \begin{cases} 0 & \text{if } T > 14.5^\circ \\ \alpha T - b & \text{if } T < 14.5^\circ \end{cases}$$

where $\alpha = -4.84$ μmol N L^{-1} °C^{-1} and $b = 68.6$ μmol N L^{-1} (n=6030, r^2 = 0.95; Fig. 2.2, p < 0.01). The values of α and b compared well with those calculated from the 53-year record of temperature and nitrate on CalCOFI line 93 (Fig. 2.2). This approach has been used in the past to estimate nitrate concentration and fluxes in the SCB (McPhee-Shaw et al. 2007, Todd et al. 2009).

Finally, there was a clear evolution in time in water column fluorescence as measured by the WW fluorometer that we wish to compare to the putative nitrate flux estimates. In the context of this study, chlorophyll fluorescence is always reported in units of voltage (the measure of fluorescence) as opposed to chlorophyll concentration. Although the instrument responses were all linear over the chlorophyll ranges we encountered, the variable and important effect of fluorescence quenching in the upper water column can only be empirically addressed. As we are more interested in spatial and temporal gradients than the precise determination of chlorophyll concentration, we rely on the fact that the instruments all proved to be stable over the course of the experiment, and utilize an empirical fluorescence quenching correction adapted from Todd et al. (2009). Finally, fluorescence was vertically integrated to give a measure of bulk phytoplankton concentration for comparison with temporal variability in nitrate flux.

2.4 Spatial and temporal gradients in biological rates

Isopycnals and isopleths of nitrate were tilted across the shelf, shoaling in shallow waters of the inner shelf (Fig. 2.3). Vertically integrated primary productivity measurements showed increasing total and new productivity across the shelf, particularly

over the inner shelf (Fig. 2.4). The 14-August transect from the mid (60 m) to inner shelf (12 m) indicated that primary productivity in the surface increased four-fold over a distance of 5 km, and showed that the bulk of the difference in total and new productivity between offshore and inshore waters occurred over the mid to inner shelf (depths < 65 m, Fig. 2.4).

Total and new productivity increased between 11-August and 17-August at all sampling locations, although the offshore to onshore gradient persisted (Fig. 2.4). There was clearly a shelf-wide increase in nitrate availability during the sampling period (Fig. 2.4). As we show below, the along-isopycnal nitrate flux forced by the internal tide reached a maximum on 11-August and diapycnal nitrate flux peaked soon thereafter.

2.5 Physical variability over the inner shelf

The unfiltered observations of currents and water column structure at the 22 m ADCP–WW mooring pair showed strong semidiurnal variability, but also indicated that there was biologically relevant variability at a number of other frequencies (Fig. 2.5, Chapter 3). Nevertheless, spectral analysis (Fig. 2.6) and empirical orthogonal function analysis (Chapter 4) demonstrated that: 1) the energy in semidiurnal-band variability of currents is greater than that at any frequency observable given the duration of the experiment and 2) the coherent semidiurnal variability dominated inner shelf physical forcing during the experimental period.

2.6 Internal tide energy flux

The cross-shore energy flux of the semidiurnal internal tide ($F_E = \langle u' p' \rangle_\phi$) was calculated following Nash et al. (2005). Semidiurnal velocity variability from the 22 m ADCP and semidiurnal density variability from the WW were extracted using a band-pass filter between frequencies of 1/11 cycles h^{-1} and 1/14.5 cycles h^{-1} (Lerczak et al. 2003). Least-squares harmonic analysis (e.g. Nash et al. 2005) is not appropriate for extracting the baroclinic tidal variability in the SSCB, as previous studies showed that the phase of the baroclinic tide is not constant (Winant and Bratkovich 1981, Lerczak et

al. 2003).

Pressure perturbation was calculated by vertically integrating the semidiurnal band-passed density perturbation profiles from the WW at each time step and assuming that the waves were hydrostatic:

$$p'(z,t) = p_{surf}(t) + \int_{-H}^{0} \rho'(\hat{z},t) g d\hat{z} \tag{2.1}$$

where $\rho'(z,t) = \rho(z,t) - \bar{\rho}(z)$, and $\bar{\rho}(z)$ was the time-mean vertical density profile, and the integration was over the dummy variable $\hat{z}$. The surface pressure was calculated by requiring that the pressure perturbation be baroclinic (i.e. $\left\langle p'(z,t) \right\rangle_H = 0$).

Velocity perturbation was calculated in a similar fashion. The velocity perturbation is :

$$u'(z,t) = u(z,t) - \bar{u}(z) - u_o(t) \tag{2.2}$$

where $\bar{u}(z)$ was the time-mean vertical profile of velocity, and the time-dependent barotropic velocity $u_o(t)$ was calculated by requiring the velocity perturbation to be baroclinic (i.e. $\left\langle u'(z,t) \right\rangle_H = 0$).

The mean vertical profiles $\bar{\rho}(z)$ and $\bar{u}(z)$ must represent the water column in the absence of internal waves, which required that the averages be formed over many internal wave periods. However, the contribution of slowly evolving water column variability must be separated from the internal wave-forced variability. In the case of our data, subtidal changes to the water column were apparent throughout the three-week deployment, and $\bar{\rho}(z)$ and $\bar{u}(z)$ were therefore calculated over eight M_2 (12.42 h) periods, which assured that the contribution of low-frequency variability to the perturbation quantities was minimized.

The perturbation quantities (u', p') reflected the variability in the strength of the internal tide over the length of the deployment, as well as the changes in water column structure (Fig. 2.7). The products of the perturbation quantities ($u'p'$) showed that changes in water column structure and the strength of the internal tide impacted both the magnitude of the energy fluxes and its vertical structure (Fig. 2.7). However, $u'p'$ must be averaged over an integral number of semidiurnal periods to determine the net flux over a tidal period.

Semidiurnal internal tide energy flux was onshore over the entire course of the experiment. The vertically integrated, time mean energy flux (E_{flux}) was 2.5 W m^{-1}. The vertical structure of E_{flux} was surface and bottom intensified (Fig. 2.8), due to the dominantly mode-one structure of the internal tide in the SSCB (Lerczak et al. 2003). Single tidal period (M_2) averages of the vertically integrated energy flux were variable in time, peaking between 11-August and 12-August with a value of > 8 W m^{-1} (Fig. 2.8). Although the time series was too short to assess the relationship between spring/neap variability in the barotropic tide and the strength of internal tidal energy flux, the maximum energy flux occurred roughly two tidal periods after the spring tide. The energy flux estimates were similar to those calculated for the inner shelf of Oregon during periods of relaxation from upwelling (2-9 W m^{-1}, Torgrimson and Hickey 1979, Moum et al. 2007).

2.7 Internal tide nitrate flux

Given the predominance of semidiurnal band current variability and the onshore flux of internal tide energy over the SSCB continental shelf, we wish to analyze the internal tide-driven nitrate flux utilizing the spatially and temporally well-resolved records of temperature and current variability from the 22 m WW–ADCP pair.

The conservation of nitrate in three dimensions can be written as:

$$\frac{\partial \bar{\mathbf{N}}}{\partial t} + \nabla \cdot \bar{\mathbf{u}}\bar{\mathbf{N}} = -\nabla \cdot \left\langle \mathbf{u}'\mathbf{N}' \right\rangle_{\phi} + Q_{+} - Q_{-} \tag{2.3}$$

where $\mathbf{u} = \bar{\mathbf{u}} - \mathbf{u}'$ and $\mathbf{N} = \bar{\mathbf{N}} - \mathbf{N}'$ are the Reynolds decompositions of velocity (m s^{-1}) and nitrate concentration (μmol L^{-1}) into time mean and fluctuating components (perturbations) and Q_{+} and Q_{-} are nitrate source and sink terms. Bold indicates that velocity and nitrate are assumed to be functions of x, y, z, and time. Both the overbar averaging and bracket averaging ($\langle \ldots \rangle_{\phi}$) denote time means over ϕ integral number of wave periods (ϕ »1). In the case of the semidiurnal internal tide, these averages were calculated over an integral number of M_2 tidal periods. Equation (2.3) is equivalent to the classic advection-diffusion equation, where the second term on the left-hand side of equation (2.3) is the advective term, and the first term on the right-hand side of equation

(2.3) is the diffusive or Reynolds flux term.

The Reynolds flux term is often estimated as the product of the velocity perturbation (u') and a length scale (L') acting on the large scale gradient in the quantity of interest. That is, the nitrate perturbation, written in one dimension (vertically) for simplicity, is estimated as:

$$N' = L' \frac{\partial \bar{N}}{\partial z} \tag{2.4}$$

The Reynolds flux term becomes:

$$\left\langle w'N' \right\rangle = \left\langle w'L' \right\rangle \frac{\partial \bar{N}}{\partial z} \tag{2.5}$$

where w is the vertical component of velocity $\mathbf{u}$ and the quantity $\left\langle w'N' \right\rangle$ is the (vertical) coefficient of eddy diffusivity, typically written as K_z. This scaling is typically employed when assessing fluxes due to turbulent fluctuations because the perturbation quantities (e.g. N') are very difficult to directly observe. However, in the case of horizontal fluxes forced by relatively low-frequency and long wavelength phenomena, such as the semidiurnal internal tide, we can estimate the perturbation quantities and Reynolds flux directly.

We simplified equation (2.3) by assuming that there was no alongshore variability ($\frac{\partial}{\partial y} = 0$), that nitrate concentration was at steady-state ($\frac{\partial \bar{\mathbf{N}}}{\partial t} = 0$), and by ignoring the source term Q_+ , thereby assuming nitrification over the inner shelf was small. The mean velocity, $\bar{\mathbf{u}}$, is zero in a uniform wave field of a single frequency, which dictated that the advective term $\nabla \cdot \bar{\mathbf{u}} \bar{\mathbf{N}} = 0$.

Written in component form, equation (2.5) becomes:

$$-\left[\frac{\partial}{\partial x} \left\langle u'N' \right\rangle_\phi + \frac{\partial}{\partial z} \left\langle w'N' \right\rangle_\phi \right] = Q_- \tag{2.6}$$

In the internal tide, the ratio of vertical to horizontal velocities (wu^{-1}) is typically < 0.01, and, although the poor vertical velocity resolution of ADCP measurements precludes the calculation of $\left\langle w'N' \right\rangle_\phi$ directly, we assumed the horizontal fluxes to be much larger than the vertical fluxes for the internal tide.

As in equation (2.6), the cross-shelf flux of nitrate was calculated as $F_{nitrate} = \left\langle u'N' \right\rangle_{\phi}$. Velocity perturbation time-series were calculated as above. The reconstructed nitrate time series $N(z,t)$ was band-passed around the semidiurnal frequency as above, and decomposed into vertical time mean and fluctuating components according to:

$$N'(z,t) = N(z,t) - \bar{N}(z) \tag{2.7}$$

There is no requirement that N' be baroclinic, as nitrate concentration is not a dynamical quantity. It should be noted, however, that requiring baroclinicity in N' will not change the vertically integrated nitrate flux (Kunze et al. 2002).

The perturbation quantity $u'N'$ reflected the variability in the strength of the internal tide over the length of the deployment, as well as the changes in water column structure and nitrate availability (Fig. 2.7). The vertically integrated, time mean cross-shelf nitrate flux (N_{flux}) was 160 g N $m^{-1}d^{-1}$. The vertical structure of N_{flux} was strongest near-bottom, and reversed sign (indicating an offshore flux) at approximately the average depth of pycnocline, and was zero at the surface (Fig. 2.8). Single tidal period (M_2) averages of N_{flux} were variable in time, ranged over two orders of magnitude, from 0 to 680 g N $m^{-1}d^{-1}$, and showed coherence with the internal tide energy flux (Fig 2.8). The timing of the maximum nitrate flux preceded the maximum internal tidal energy flux by approximately one tidal period, although the increase and decrease of nitrate flux closely tracked the internal tide energy flux.

The cross-shelf nitrate flux driven by the internal tide was onshore. We calculated the equivalent vertical nitrate flux necessary to balance the onshore, cross-shelf flux as a scaling between the vertical length scale of the cross-shelf flux and the horizontal length scale of the resulting vertical flux. The ratio of those length scales, H L^{-1}, was 0.01, where H (the depth of the water column) was 20 m and L (the distance from the WW mooring to the shoreline) was 2000 m for the particular geometry of the shelf in the experimental area. Therefore, in order to facilitate comparison with the vertical nitrate fluxes estimated from the dissipation of high-frequency kinetic energy presented below, and with those values reported for other areas in the literature, we have scaled the average cross-shelf nitrate flux into an effective vertical flux by multiplying the cross-shelf flux estimates by 0.01.

Using the Redfield ratio to convert between nitrogen and carbon, and using the horizontal to vertical scaling above, the time-averaged cross-shelf nitrate flux was capable of supporting 455 mg C m^{-2} d^{-1} of new productivity over the inner shelf over the course of the 3-week experiment. This would account for approximately one half of the estimated total productivity reported in previous studies over the SSCB inner shelf (Eppley and Holm-Hansen 1986, Eppley 1992), and CalCOFI primary productivity data at the closest station (Table 2.1). Single tidal period averages of nitrate flux, when converted to potential new productivity as before, ranged from 0 to 1800 mg C m^{-2} d^{-1} (Fig. 2.8). CalCOFI total primary productivity averaged 833 mg C m^{-2} d^{-1} for observations at the nearest station (line 93.3, station 26.7, 63 m depth) in July and August (n=16, Table 2.1), so single tidal period values either represented an over-estimate of the actual nitrate flux, or, during active periods of the semidiurnal internal tide, the cross-shelf nitrate flux induced an increase in phytoplankton productivity and phytoplankton concentration.

The vertical structure of the time-mean nitrate flux was strongly onshore below the time-mean position of the nitricline (Fig. 2.8). However, above the nitricline, the time-mean flux was weakly negative (offshore). Although the use of temperature as a proxy for nitrate confounds the interpretation of this feature, it is possible that the internal tide acts to redistribute inner shelf nitrate offshore at or above the pycnocline, perhaps in a manner similar to the formation and transport of intermediate nepheloid layers due to internal wave activity (McPhee-Shaw and Kunze 2002, McPhee-Shaw et al. 2004).

2.8 High-frequency internal waves

The internal tide delivered an onshore flux of nitrate, which must be re-distrubted vertically to account for the elevated new productivity measured over the inner shelf (Fig. 2.4). High-frequency internal waves (HFIWs, periods of $\sim$30 min to the buoyancy period ($\sim$ 3 min) are commonly observed in the SSCB, and are thought to be the sink by which the internal tide transfers its energy to dissipative scales (Inall et al. 2000, Lerczak 2000, Helfrich and Grimshaw 2008). Moreover, packets of high-frequency waves

propagate coherently across the shelf, losing energy to dissipation in the shallow water of the inner shelf (Lerczak 2000, Moum et al. . 2003). If we assume that the variability in baroclinic currents between 30 min and 3 min (the average buoyancy period) was due primarily to high-frequency internal waves (Lerczak 2000), we can estimate the cross-shore convergence of high-frequency internal wave kinetic energy by constructing power spectral density estimates of kinetic energy at each ADCP mooring, integrating those spectra vertically and over the frequency band of interest, and finally assessing the degree to which kinetic energy is lost across the array.

We estimated the kinetic energy (KE) in the high-frequency band (defined as the frequency span of 0.5 cycles hr^{-1} to the buoyancy frequency (0.33 cycles min^{-1})) at each mooring individually. Kinetic energy spectra were calculated as:

$$KE_{spec} = \frac{H}{2}\bar{\rho}\left[\left\langle u(\sigma)^2\right\rangle, \left\langle v(\sigma)^2\right\rangle, \left\langle w(\sigma)^2\right\rangle\right]\Delta\sigma^{-1} \tag{2.8}$$

where H is the depth range over which the ADCP samples, $\bar{\rho}$ is the average density over the course of the deployment (taken to be 1024 kg m^{-3}) and $\Delta\sigma^{-1}$ is the frequency band-width of the spectral calculation (Lerczak 2000). The sum of the frequency- and vertically integrated KE spectra of the individual components of velocity form an estimate of the total kinetic energy (tKE) at each mooring:

$$tKE = \sum_{u,v,w}\int_{H_2}^{H_1}\int_{\sigma_b}^{\sigma_b} KE(u,v,w)d\sigma dz \tag{2.9}$$

where H_1 and H_2 are the shallowest and deepest ADCP bins, respectively, and σ_a and σ_b are 0.33 cycles min^{-1} and 0.0083 cycles min^{-1}, respectively. We formed running estimates of KE by calculating KE spectra from a sliding 24h window, forming tKE estimates every 6 h as above (dof = 8).

Although our estimates of tKE included error inherent in the ADCP measurements and suffered from the short-comings implicit in spectral analysis, we made an order-of-magnitude estimate of the dissipation rate required to balance the flux convergence of tKE between instruments across the shelf (Lerczak 2000). That is,

$$\varepsilon = \frac{\left(\frac{1}{H_1}KE_1 c_{g_1} - \left(\frac{1}{H_2}KE_2 c_{g_2}\right)\right.}{\frac{H_1}{2}\Delta x_{2-1}} \tag{2.10}$$

where $H_{(1,2)}$ is the water depth and $c_{g_{(1,2)}}$ is the group velocity at the 32 m and 7 m mooring, respectively, and the dominator is the area over which the estimates of tKE were made.

The estimated dissipation rate (ε) is subject to the assumptions that all of the tKE lost across the shelf is lost to dissipative processes, and that we can use phase speed (c_p) in place of group velocity (c_g) (at the frequencies of interest, Lerczak (2000) showed $c_p \approx c_g$). We calculated c_p based on the coherence of vertical velocity fluctuations across the shelf (which compares well to the theoretical linear formulation of phase speed, Lerczak 2000) as $c_{p_1} = 27.5$ cm s^{-1} at 32 m, $c_{p_1} = 8$ cm s^{-1} at 7 m.

Finally, we estimated the vertical eddy diffusivity (K_z) and the vertical nitrate flux based on measurements of buoyancy frequency profiles from the WW profilers, and a temperature/nitrate relationship derived from the cross-shore CTD/ISUS transects as above. K_z was estimated the usual way (e.g. $K_z = \Gamma \frac{\varepsilon}{N^2}$ where Γ = 0.2, Osborn 1980). Nitrate flux was calculated as $N_{flux} = K_z \frac{\partial [NO_3^-]}{\partial z}$, where nitrate gradients were estimated as the vertically-averaged nitrate gradient from the reconstructed nitrate field.

2.8.1 High-frequency internal wave-driven nitrate flux

Time series of mid-water column vertical velocities at the five ADCP moorings indicated that packets of high-frequency internal waves arrived twice daily and propagated coherently across the shelf, losing kinetic energy in the shallow water of the inner shelf (Fig. 2.9). Although there was a broad shoulder of elevated KE energy in all velocity components between periods of 1 hour and 3 minutes, vertical velocity was most strongly modulated by the passage of high-frequency internal waves (Fig. 2.9). This vertical velocity variability was associated with isopycnal displacement forced by the passage of packets of internal waves, where peak-to-trough displacement exceeded 5 m on timescales of minutes. The maximum energies in the vertical velocity spectra were at frequencies 0.1 cycles min^{-1} (Fig. 2.9). KE of all components of velocity decreased from offshore to onshore, consistent with the interpretation that the high-frequency internal waves lose energy as they moved across the shelf. Depth-averaged and individual bin kinetic energy estimates (not shown) also decreased from offshore to onshore, providing a more conservative demonstration that velocity variance decreases across the

shelf in the high-frequency bands.

The running estimate of tKE demonstrated that tKE decreased across the shelf, with minimum values at the 7 m ADCP. tKE varied 3-fold at the 32 m ADCP, from a minimum of 5 N m^{-1} to a maximum of > 16 N m^{-1}. The time variability in the tKE was correlated among instruments and the correlation decreased with distance between instruments. Time variability in the shallowest ADCP was similar in percentage terms to the outermost ADCP, although the total magnitude of tKE was much smaller. The running estimates of tKE peaked at the outer moorings between 9-Aug and 13-Aug, and were again elevated above the mean value between 15-Aug and 18-Aug. These periods were characterized by energetic internal tides, as would be expected if the high-frequency internal waves were ultimately driven by the internal tide (Fig. 2.8, Fig. 2.9, Fig. 2.10).

Estimates of dissipation and vertical eddy diffusivity calculated from the convergence of kinetic energy flux ranged between 0.75-1.5 x 10^{-7} W kg^{-1} and 1.8-3.5 x 10^{-5} m^2 s^{-1}, respectively (Fig. 2.10). Dissipation peaked at the same time as both the high-frequency kinetic energy and the internal tidal energy flux. The values and ranges of dissipation and vertical eddy diffusivity were similar to those previously calculated for the SSCB (Lerczak 2000) and in other shelf-seas around the world (Largier 1994, MacKinnon and Gregg 2003, Sharples et al. 2001, 2007).

Vertical nitrate flux forced by the dissipation of high-frequency internal waves followed a similar time course to the cross-shelf nitrate flux calculated for the semidiurnal tide (Fig. 2.8, Fig. 2.10). However, the magnitude of the vertical nitrate flux due to high-frequency internal wave dissipation was approximately a factor of five less than the scaled vertical nitrate flux due to the semidiurnal tide. Taken alone, the time-mean vertical nitrate flux accounted for a Redfield-scaled new productivity of 137 mg C m^2 d^{-1} over the course of the deployment, ranging from zero to 274 mg C m^2 d^{-1}. The HFIW-forced vertical nitrate flux peaked around 10-August (slightly before the peak internal tide-forced cross-shelf flux) and then again near the end of the experiment (Fig. 2.10).

2.9 Temporal variability in nitrate flux, chlorophyll fluorescence and primary productivity

We used vertically integrated fluorescence from the WW mooring as a bulk measure of phytoplankton concentration. Particulate carbon analysis from water samples confirmed that the subsurface chlorophyll maximum was also a biomass maximum, and the changes in fluorescence represented actual changes in phytoplankton biomass over the course of the experiment (Chapter 3). The time course of vertically integrated fluorescence also reflected a subsurface bloom of diatoms after 17-August-2006 (Chapter 3). Phytoplankton concentrations showed two peaks over the course of the ISPX experiment, the first subsequent to the peak of the along-isopycnal internal tide-driven nitrate flux (period I, panel b, Fig. 2.10), and the second during the final week of the deployment, when HFIW-forced nitrate flux was at a maximum (period II, panel c, Fig. 2.10).

The estimates of IT and HFIW forced nitrate flux were variable by approximately an order of magnitude over the course of the ISPX experiment. The variability was due to a combination of changes in the energy of the semidiurnal and HFIW fields, the strength of stratification, and both the vertically integrated nitrate concentration and the vertical gradient of nitrate concentration. Although care was taken to remove the contribution of large-scale, low-frequency changes to the depth of the nitricline in the calculation of the cross-shelf IT flux of nitrate, the vertical HFIW flux contained a significant contribution of that variability. This can be best seen in Fig. 2.10 during the final week of the deployment. Although HFIW energy peaked between 10-August and 11-August (coincident with the strongest IT activity, energy and nitrate flux, Fig. 2.8, Fig. 2.9), HFIW nitrate flux values were similar during the final days of the experiment to the flux calculated at the peak of HFIW kinetic energy. This was due to weakened stratification in the final week and consequently a smaller N^2 in the denominator of the eddy diffusivity calculation (Fig. 2.10). It is therefore difficult to separate changes in the vertically integrated fluorescence content of the water column due to variability in the IT and HFIW forced flux and changes in background stratification and the vertical gradient in nitrate concentrations.

The three surveys of primary productivity corresponded with the peak along-isopycnal and diapycnal internal-wave mediated nutrient flux (Fig. 2.8, Fig. 2.10). Changes among the days are consistent with the conclusions we have drawn from the mooring-based flux calculations. Our observations show an intense, stable gradient in total productivity between the outer and inner shelf (Fig. 2.4) (average gradient of 0.10 mg C m^{-3} d^{-1} between mid-shelf and the innermost sampling location). These observations suggest that, while a cross-shelf gradient of primary productivity and phytoplankton biomass is an emergent feature in this system, both primary productivity and phytoplankton concentrations over the shelf will be responsive to the temporal variability of the IT and HFIW mediated flux. For example, in as much as the internal tide shows evidence of spring/neap variability consistent with the barotropic tide, we would expect a spring/neap signal in primary productivity (e.g. Sharples 2008).

2.10 The hose and the sprinkler: internal wave mediated nitrate flux

Over the SSCB inner shelf, isopycnal tilt (Fig. 2.3), horizontal flux convergence (Fig. 2.8), and diapycnal mixing (Fig. 2.10) contributed to enhanced inner shelf productivity. The strong gradient in near-surface new productivity implies enhanced surface nitrate supply inshore, and, since measureable deviations from the temperature nitrate relationship were not observed over the inner shelf, the onshore transport of nitrate due to the IT must be partly balanced by vertical, diapycnal flux to the surface waters and subsequent phytoplanktonic uptake.

In the absence of mixing, advective fluxes are reversible. We band-passed filtered the velocity, pressure and nitrate time series around the semidiurnal frequency, a necessary step in order to estimate a net flux (Nash et al. 2005). This approach, however, had the drawback of excluding the higher harmonics of the tide, which were apparent in Fig. 2.9. These higher harmonics were likely the result of nonlinearity—and that nonlinearity ultimately must drive mixing (e.g. Moum 2003). For example, the mean internal tide energy flux over the course of the experiment was 2.5 W m^{-1}, implying an areal mean dissipation of 1.25 x 10^{-7} W kg^{-1}. We do not have any information on how

or where this energy was lost, although we expect that bottom boundary layer processes are important. The nitracline intersected the bottom in the inner shelf over the course of the ISPX experiment. Thus we hypothesize that mixing associated with the loss of internal tide energy in the bottom boundary layer was an important mechanism by which the along isopycnal flux of nitrate was redistributed vertically.

In addition to bottom boundary layer processes directly driven by the internal tide, the HFIW-forced dissipation provided another source of energy to mix nitrate to the surface from the constantly renovated sub-nitricline waters. Thus, the total nitrate available for phytoplankton consumption over the inner shelf was a product of horizontal and vertical fluxes at a number of different frequencies. The artificial separation between HFIWs and IT fluxes, required to make these estimates tractable, implies that the total nitrate flux is not simply a linear combination of the estimates presented here.

We therefore hypothesize that internal wave-driven nitrate flux to the inner shelf of the SSCB is composed of two complementary pathways: 1) horizontal (along-isopycnal) nitrate flux due to the internal tide and 2) vertical (diapycnal) nitrate flux driven by in part by mixing due to the dissipation of high-frequency internal waves and in part by mixing directly associated with the internal tide. While the along-isopycnal internal tide nitrate flux was significantly larger than the HFIW mixing-driven diapycnal flux, either mechanism can independently enhance vertically integrated primary productivity independently, given the persistently sloped isopycnals across the shelf (Fig. 2.3). For example, along-isopycnal transport can enhance productivity at the chlorophyll maximum if the inner shelf chlorophyll maximum is co-limited by light and nitrate, as is the case in the SSCB inner shelf (Cullen et al. 1983, Eppley and Holm-Hansen 1986, Eppley 1992). Mixing and diapycnal nitrate flux due to HFIW dissipation across the nutricline can enhance surface primary productivity in the absence of along-isopycnal flux, although, without renovation, sub-nutricline waters would eventually be depleted of nitrate as the water column mixed. Nevertheless, we expect that, given the dynamical connection between the internal tide and HFIWs, these mechanisms are rarely or never acting independently, and instead act together to both provide a pool of nitrate to the inner shelf (IT-forced horizontal flux) and to mix that nitrate to the surface waters (HFIW-forced diapycnal nutrient flux, Fig. 2.10).

The cross-shelf flux of nitrate forced by the internal tide is alone capable of supporting all of the new productivity over the SSCB shelf during the stratified, summer months. Moreover, based on the time course of single tidal-period estimates, cross-shelf nitrate flux forced by the semidiurnal internal tide can relieve the nitrate limitation of coastal phytoplankton populations, leading to increased phytoplankton concentration over the inner shelf (Fig. 2.8, Fig. 2.10).

Further studies, with a more extensive cross-shelf array of current and density profilers, would be required to satisfactorily separate the relative contributions of IT and HFIW fields. Moreover, profilers capable of direct measurement of the nitrate field with sufficient resolution, in combination high resolution estimates of the deviations of the nitrate-temperature relationship across the shelf, are needed to more accurately estimate the nitrate flux due to both the IT and HFIW fields.

2.11 Errors associated with the Reynolds method of calculating nitrate flux

The method used here is a simple and powerful way of estimating fluxes of nitrate due to the internal tide. However, there are several caveats, and care is required when calculating nitrate flux to avoid spurious results. The nitrate and energy flux estimates are only meaningful if the bracket averaged quantity ($\langle \dots \rangle_\phi$) is calculated over an integral number of wave periods, which requires that the wave field in question be dominated by a single frequency (Nash et al. 2005). The internal tide is perhaps one of the simplest candidates for this approach– in the SSCB, the signal is energetic and has a limited bandwidth, so that it can be effectively extracted by band-pass filtering. Conversely, the Reynolds flux approach is difficult to implement for the high-frequency internal wave band, because the bandwidth of the waves is broad (Fig. 2.9), complicating the separation into mean and perturbation quantities. It is for this reason that we do not calculate $\langle w'N' \rangle$ to estimate the vertical nitrate flux due to HFIWs directly.

Nash et al. (2005) give methods for assessing the error in energy flux estimates given incomplete sampling in time or space. The largest error in our energy flux estimate is the incomplete sampling of the near-surface with the ADCP. Measurements within

$\sim$2 m of the surface are always biased in ADCP measurements, typically because of pulse reflection from the surface and contamination by surface wave-induced velocities. Mode-1 internal waves are surface and bottom intensified, so direct measurements of near-surface velocities is important for accurate energy flux estimates. The bias inherent in energy flux estimates due to surface contamination of ADCP data is exacerbated in shallow depths, and care must be taken to assess the potential contribution of errors due to incomplete sampling in the estimates of flux.

We expect that incomplete sampling near the surface in our analysis produced an error that is approximately 15%, given the dominance of the M_2 variability found in the SSCB internal wave field. This bias is likely to be lower than the true value, so that we expect to be underestimating the energy flux based on the experimental design employed in ISPX (see Nash et al. 2005).

Estimating nitrate concentrations based on temperature is an imperfect method. On time scales that are short relative to the capability of phytoplankton to take up nutrients (< several hours), the temperature/nitrate relationship is unstable, and nitrate concentrations will be higher than the canonical value on an isotherm in a region of flux convergence. On time scales similar to those of phytoplankton uptake ($\sim$ several hours), a light-saturated but nutrient-limited phytoplankton assemblage will consume available nitrate at a rate proportional to both the phytoplankton concentration and the phytoplanktonic capacity to up-regulate nitrate uptake. This leads to a negative bias relative to the canonical nitrate/temperature relationship. Finally, at time scales where the phytoplankton population is at steady state, the consumption of nitrate is balanced by its supply and the temperature/nitrate relationship is steady.

We expect that, given the multitude of observations that verify the long-term stability of the nitrate/temperature relationship in the SSCB, temperature provided an excellent proxy for nitrate when calculating the flux over the entire duration of the experiment. Single M_2 tidal averages, however, would likely include error due to deviations from the nitrate/temperature relationship. We expect our estimates to be conservative because a fractional sink inshore (in the direction of the flux) relative to that offshore would make the true tidal-averaged flux higher than estimates based on a strictly conservative temperature/nitrate relationship (McPhee-Shaw et al. 2007). Given that the linear

fit between temperature and nitrate accounts for approximately 95% of the variability in the nitrate observations, we expect the total error of the cross-shelf flux estimates to be somewhat larger than 15%, likely biased lower than the true value in the case of single tidal average estimates.

2.12 Conclusions

We have used a novel application of Reynolds flux calculations to estimate the cross-shelf nitrate flux due to the semidiurnal internal tide. These estimates provided reasonable values for the nitrate flux based on our observations of primary productivity and new productivity over the inner shelf, and based on 20 years of CalCOFI data at a nearby station. In concert with this horizontal nitrate flux, the dissipation of high-frequency internal wave energy across the shelf drives a vertical, diapycnal nitrate flux capable of supporting significant primary productivity. Both the HFIW and the IT-forced flux varied by factor of 5 or more in time. There were periods when the nitrate flux to the inner shelf appeared to relax the nitrate limitation of primary productivity, which in turn lead to increasing phytoplankton concentrations. We expect that the horizontal flux of nitrate due to the internal tide and the diapycnal flux of nitrate due to the dissipation of HFIWs are the primary, complementary drivers of the cross-shelf gradients in phytoplankton biomass, surface chlorophyll concentrations, new and total productivity in the SSCB (Eppley 1992, Fig. 2.1, Fig. 2.4). In other continental shelf seas where velocity, density and nitrate variability is dominated by the internal wave field, most commonly in narrow and steep continental shelf systems, we expect that this mechanism would be of first-order importance. In areas with wide shelves, such as the east coast of the Americas, or areas where wind-forced upwelling or continental run-off are important, the internal wave nitrate delivery mechanism is likely of secondary importance in general, but may be the primary nitrate flux mechanism on occasion, when other forcing is absent.

Table 2.1: Vertically integrated primary productivity values from CalCOFI line 93.3 station 26.7 (63 m depth), 1984-2008, for the stratified summer and early fall months. The primary productivity values here represent estimates offshore of the ISPX inner shelf mooring array. Based on our estimates of primary productivity gradients and those made by Eppley (1992), these values may underestimate the climatological mean primary productivity over the inner shelf of the SSCB.

month	mean PP (mg C m^2 d^{-1})	σ (PP)	maximum PP	number of obs
July	889	403	1751	11
August	712	576	1629	5
September	612	302	997	4
October	838	674	2120	6

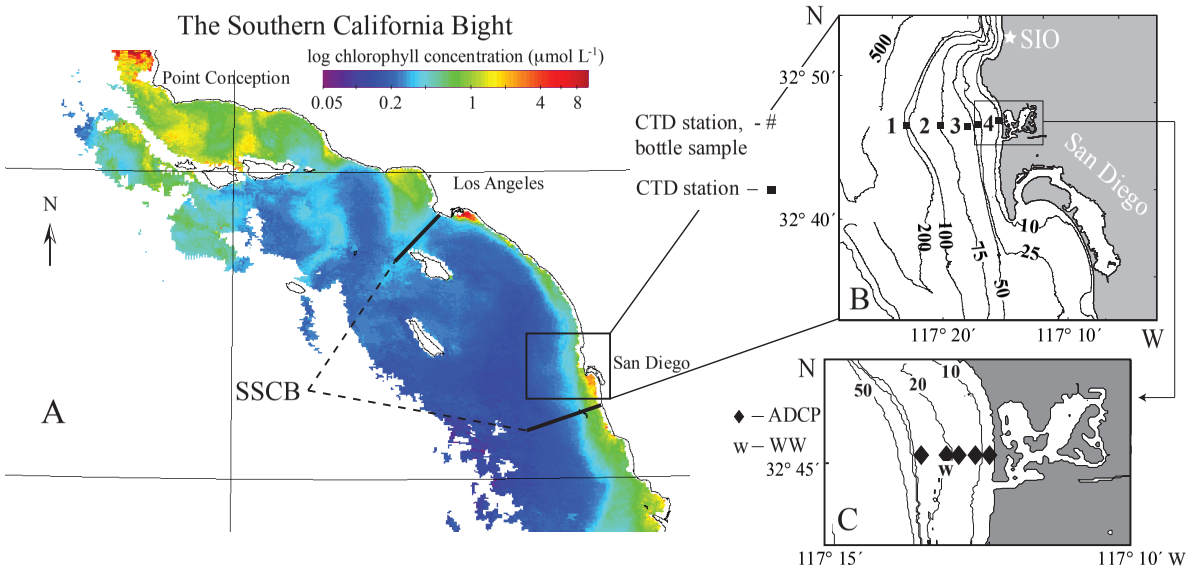

Figure 2.1: Panel A: SeaWIFS 5 day composite image of chlorophyll a in the Southern California Bight for 14-August to 18-August, 2006. The southern SCB (SSCB) region extends from the Palos Verdes peninsula to the upwelling system south of the United States–Mexico border. Chlorophyll concentrations were elevated in a narrow band over the continental shelf. This image is typical of chlorophyll a images in the region during stratified summer months (see Eppley 1992). Panels B and C: ISPX study area. The upper panel shows the locations of the cross-shelf CTD and water sampling transects. The total transect distance was ∼15km (from >400 m to 30 m depths). The lower panel shows the location of the inner shelf array of ADCPs and WW profiling moorings. The cross-shelf nitrate flux measurements were made at the ADCP-WW pair.

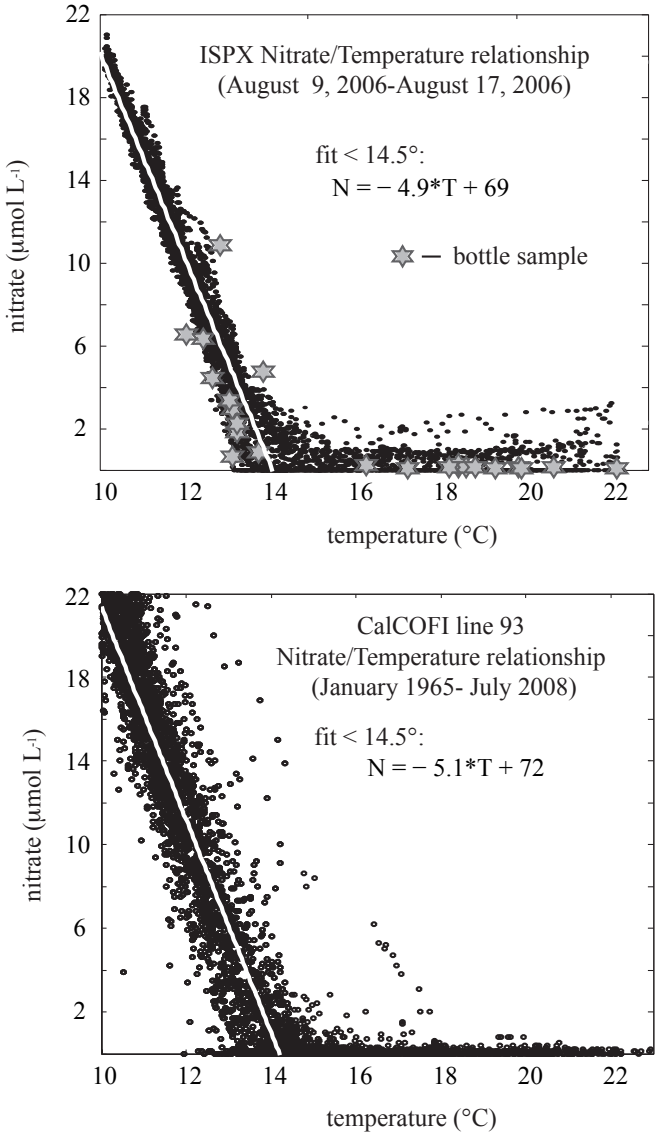

Figure 2.2: Upper panel: Nitrate–Temperature relationship from the CTD and ISUS nitrate sensor for all ISPX CTD profiles (n=56). Gray stars show nitrate and temperature determined from the bottle samples (n=24). The white line represents a linear fit of nitrate from the ISUS to temperature CTD temperature (< 14.5 °C). The ISUS has poor low-end detection, and all bottles above 14.5 °C had nitrate < 0.1 μmol L^{-1}. Lower panel: 53 years of temperature and nitrate bottle data from line 93, stations 93.30 and 93.26. (n=8394). Fit was calculated as above. The N–T relationship over the shelf and from the long-term CalCOFI record are remarkably similar, indicative of the stability of the N–T relationship.

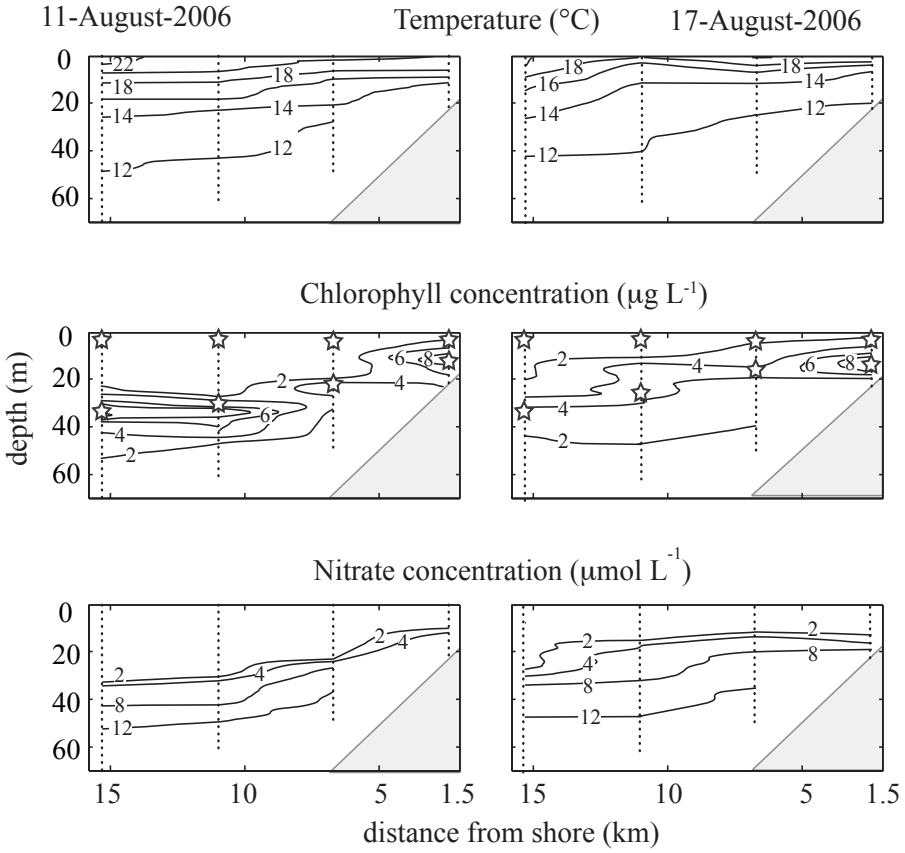

Figure 2.3: Cross-shelf transects of temperature, chlorophyll concentrations, and nitrate as measured by the ISUS nitrate sensor. Open stars show the depths and locations of the water sampling for nutrient determination and primary productivity and nitrogen uptake experiments. A strong chlorophyll maximum was present in all casts; the chlorophyll maximum and nitricline were shallower over the inner shelf than offshore. This cross-shelf shoaling of the nitracline was apparent in all cross-shelf transects (Table 3.1)

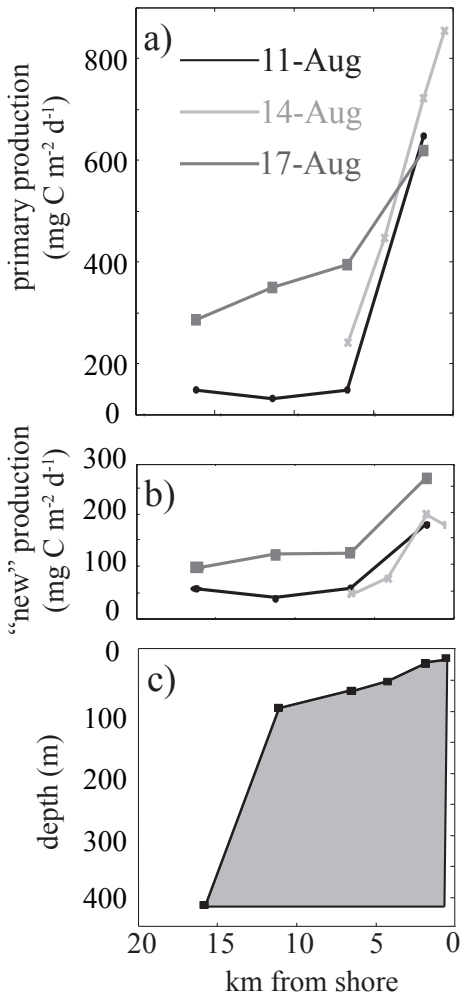

Figure 2.4: Vertically integrated a) primary productivity and b) 'new' productivity across the continental slope and shelf (c). There was a strong gradient across the shelf in primary productivity, new productivity and f-ratio, increasing inshore on all sampling days. The strongest gradient occurs between the outer and inner shelf. On 14-August, the four stations across the shelf indicated an increase of a factor of 4 in total productivity over 5 km. New productivity also increased inshore, and, although it did not account for all of the inshore increase in total productivity, these observations required enhanced delivery of inorganic nitrogen over the inner shelf.

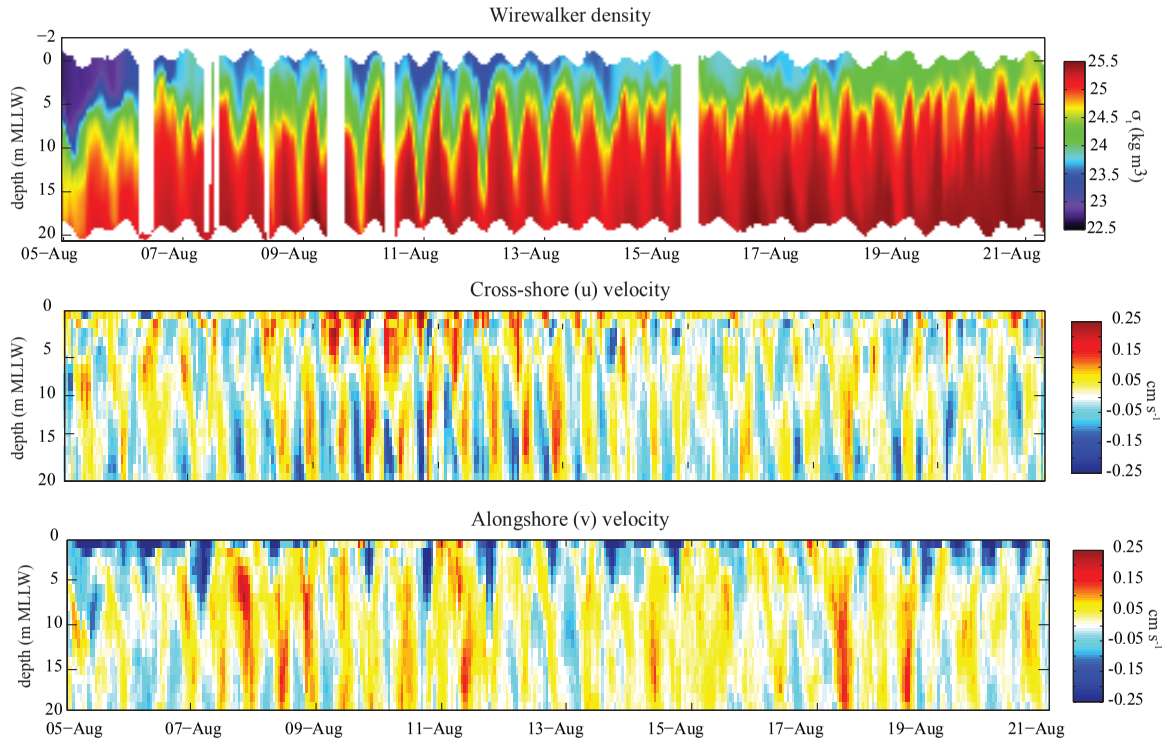

Figure 2.5: Density, cross-shore and alongshore currents measured at the 22 m WW-ADCP pair. All data was gridded into 0.25 m by 1 hr bins, and was plotted vertically in meters from the surface relative to mean lower low water (MLLW). The large vertical excursions in density are forced by the internal tide. Schematically, the internal tide forces high density water up-shelf by onshore flow near the bottom while offshore flow at the surface advects low density water offshore. In the opposite phase of the internal tide, onshore flow at the surface brings low density waters waters onshore, while offshore flow near the bottom advects high density waters down-shelf.

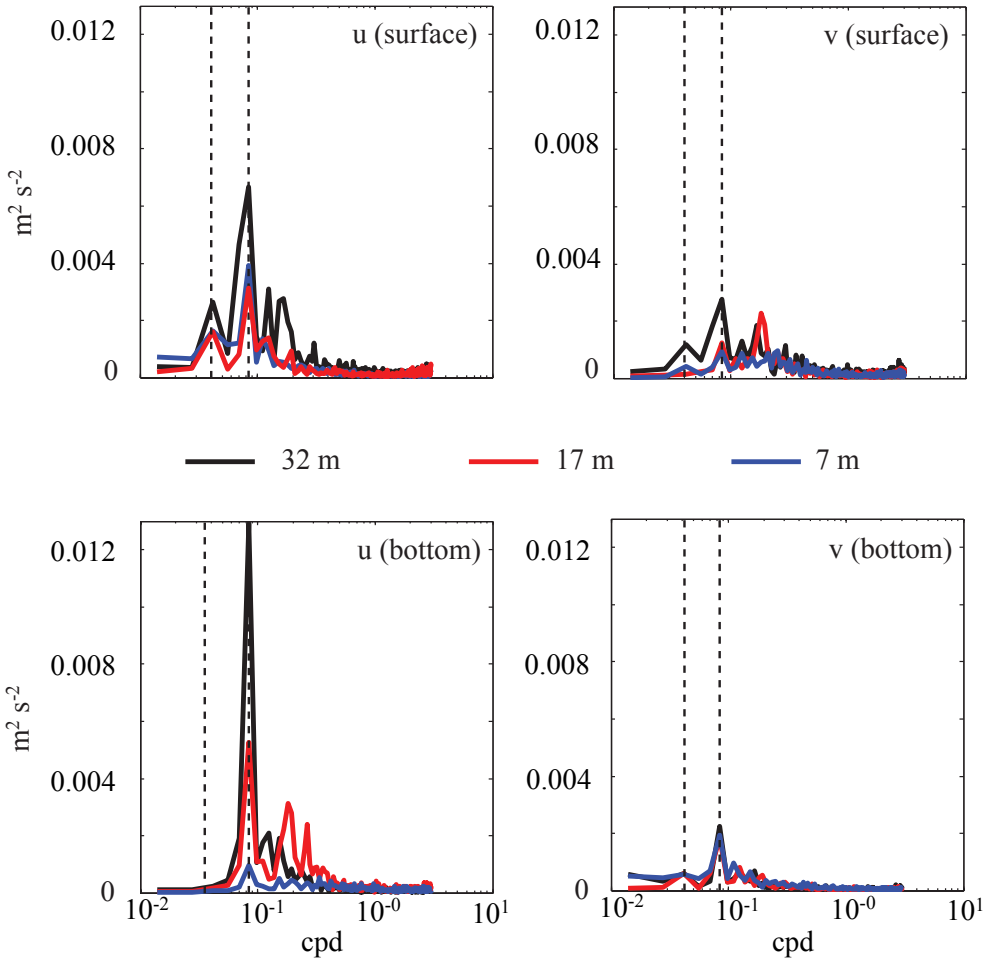

Figure 2.6: Variance-preserving power spectral density estimates of cross-shore (u) and along-shore (v) velocity from the near-surface and near-bottom, from periods of 3 days to ten minutes at the 32 m, 12 m and 7 m ADCPs. Inertial (f) and M_2 frequencies are shown as vertical dashed lines. The variability in velocity in all panels was most energetic at the semidiurnal frequency. u velocity variability is larger than v velocity variability at the semidiurnal frequency. The energy of u velocity variability decreases across the shelf, particularly at the near-bottom.

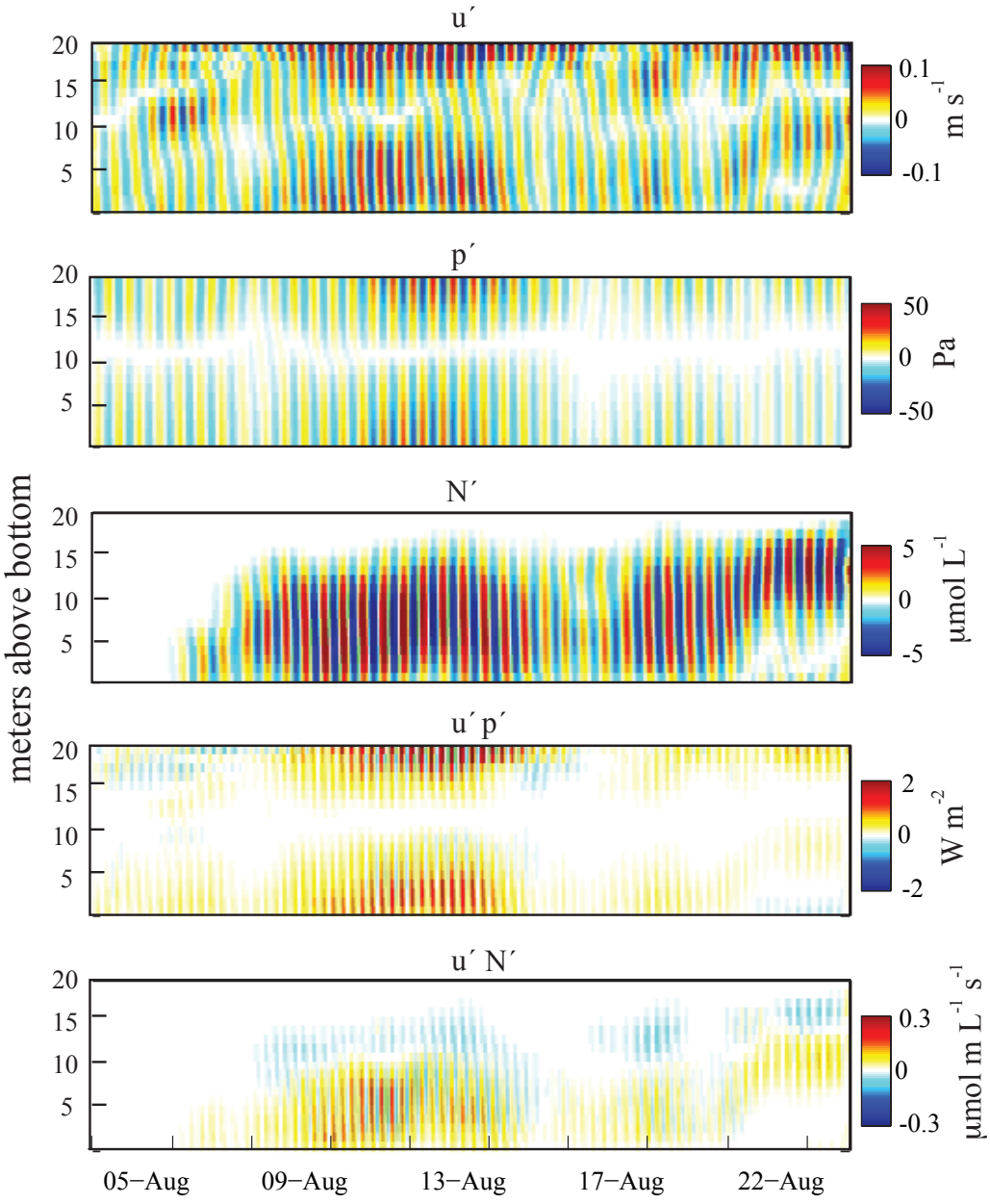

Figure 2.7: Perturbation fields of cross-shore velocity, pressure, and putative nitrate from the 22 m ADCP and WW moorings, band-passed around the semidiurnal frequency (1/11 to 1/13.5 cycles h^{-1}). Cross-shore velocity (u') and pressure (p') perturbations are dominated by the mode-1 vertical structure of the internal tide. The product of $u'p'$ and $u'N'$ are shown for heuristic purposes and to show the time variability of the vertical structure of those quantities—meaningful estimates of net energy and nitrate fluxes require averaging over integral tidal periods (Fig. 2.8)

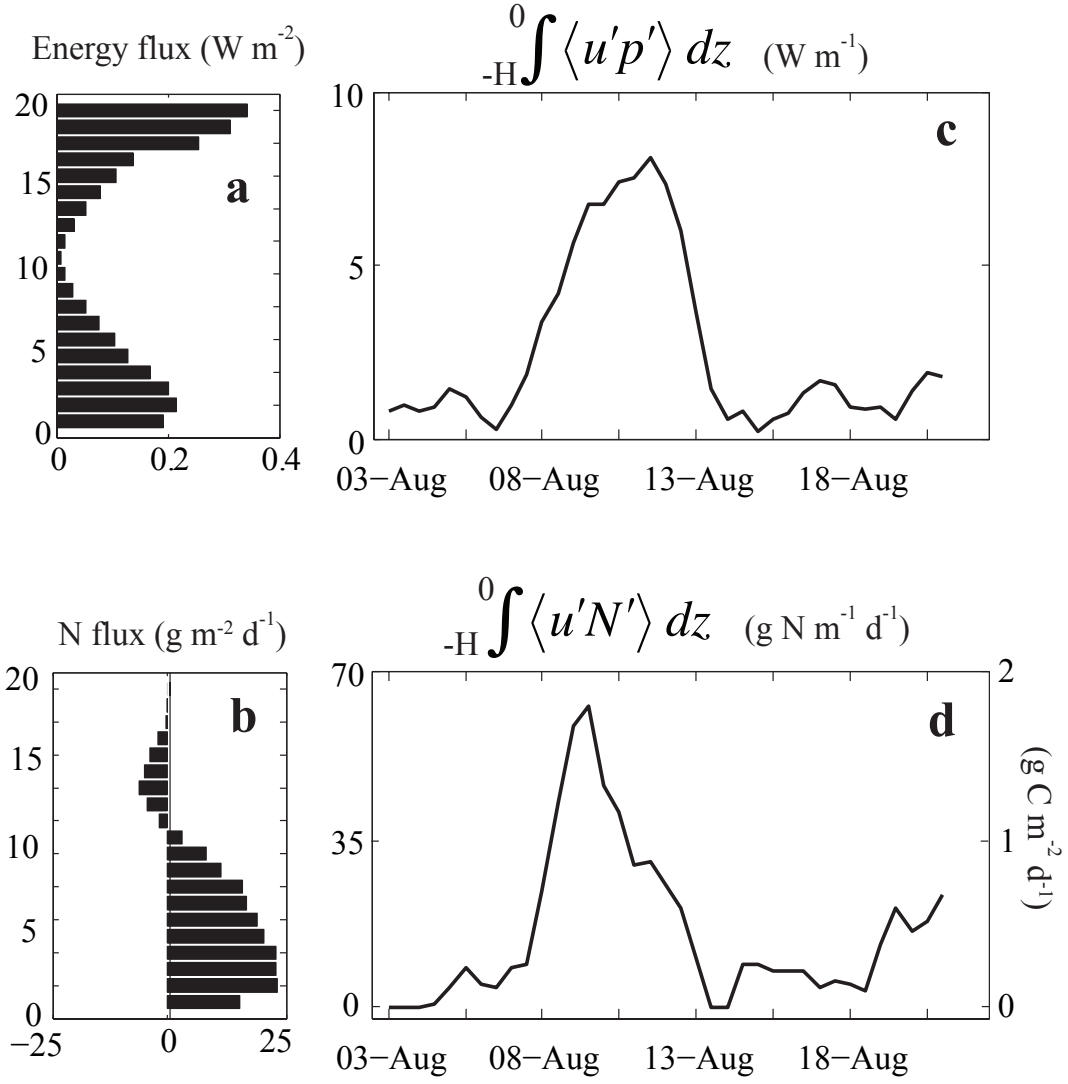

Figure 2.8: Internal tide energy and nitrate fluxes. Panels a and b show the vertical structure of energy flux (a) and nitrate flux (b) averaged over 38 M_2 (12.42 h) periods. Energy flux (a) is surface and bottom intensified, with a mid-column minimum. Nitrate flux (b) is negative (offshore) above the mid-column minimum in energy flux, and strongly positive below. Panels c and d show the vertically integrated, single M_2 period-averaged energy (c) and nitrate (d) flux. The increase in energy flux and nitrate flux are coincident; however, the vertically integrated nitrate flux peaks 2 M_2 periods before the vertically integrated energy flux. Vertically integrated nitrate flux has a secondary maximum at the end of the experiment.

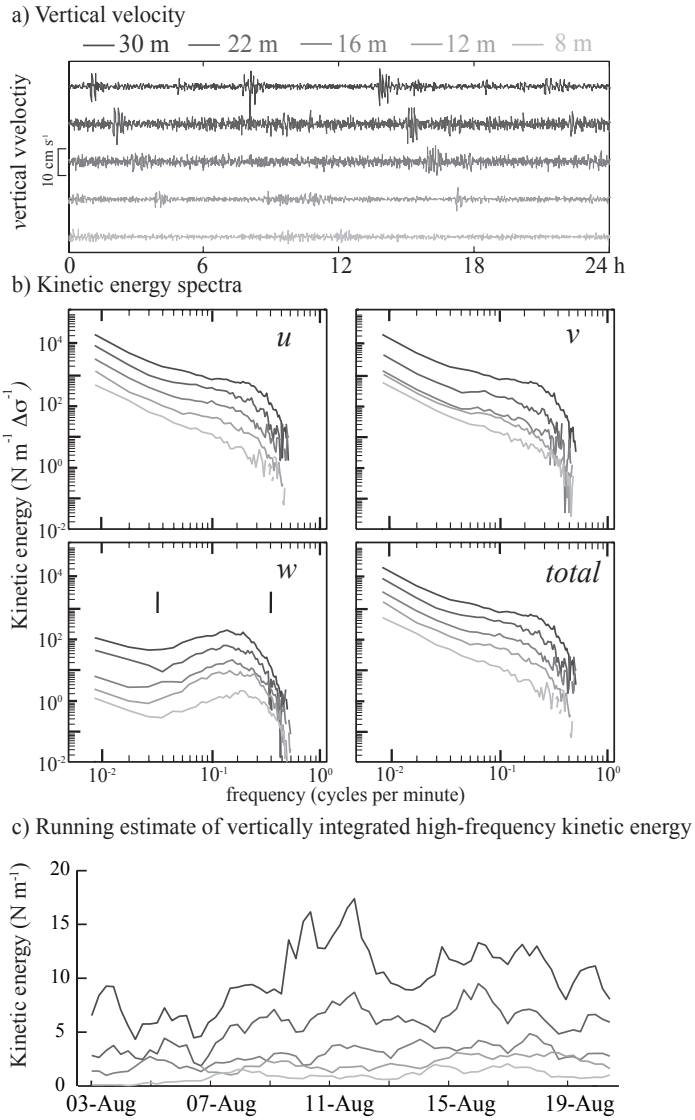

Figure 2.9: Panel a: 24 h time series of vertical velocity across the ADCP array (18-August-2006). Packets of high-frequency internal waves arrived twice daily, and were observed to propagate coherently across the array, decreasing in magnitude in shallower waters. Panel b: Vertically integrated kinetic energy spectra of cross-shore (u), along-shore (v), and vertical velocity (w). The vertical bars on the w panel represent the high-frequency internal wave band. The elevated shoulder of energy was associated with the passage of high-frequency internal waves. Panel (c): Running estimates of frequency and vertically integrated high-frequency total kinetic energy. High-frequency kinetic energy variability peaked between 10-August and 12-August, in concert with the peak internal tide energy.

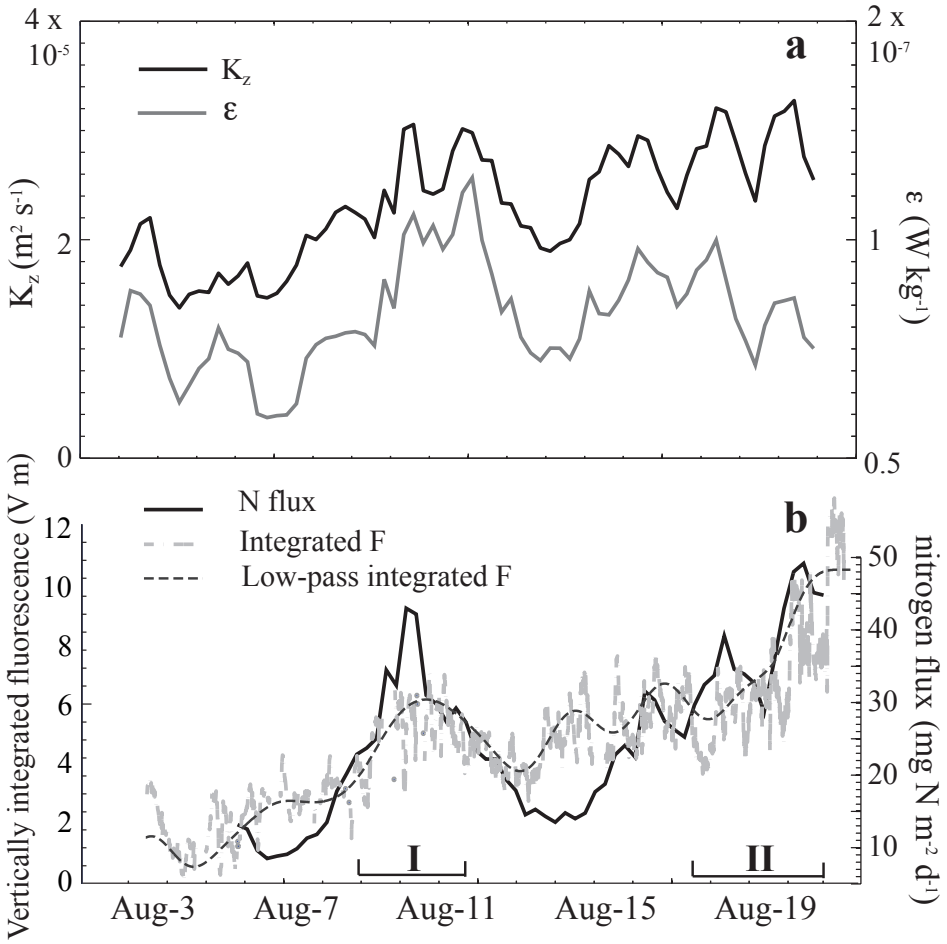

Figure 2.10: HFIW dissipation and nitrate flux in the context of vertically integrated fluorescence. Panel a: Dissipation (ε) and vertical eddy diffusivity (K_z) calculated from the cross-shore convergence of HFIW kinetic energy. Dissipation is variable over the course of the experiment by a factor of 4, and peaks on 11-Aug and decreases thereafter. K_z remains elevated through the final week of the experiment, due to the decreasing strength of stratification (N^2). Panel b: Vertical nitrate flux and vertically integrated fluorescence. Periods I and II (see text) are shown. Nitrate flux in period I was due to the largest dissipation of HFIW energy and was coincident with the largest horizontal flux due to the internal tide 2.8. Nitrate flux in period II was driven by a combination of weakening stratification and increased nitrate availability. Vertically integrated fluorescence is coherent with the estimates of vertical nitrate flux, indicating an increase in phytoplankton concentration due to increased nitrate flux.

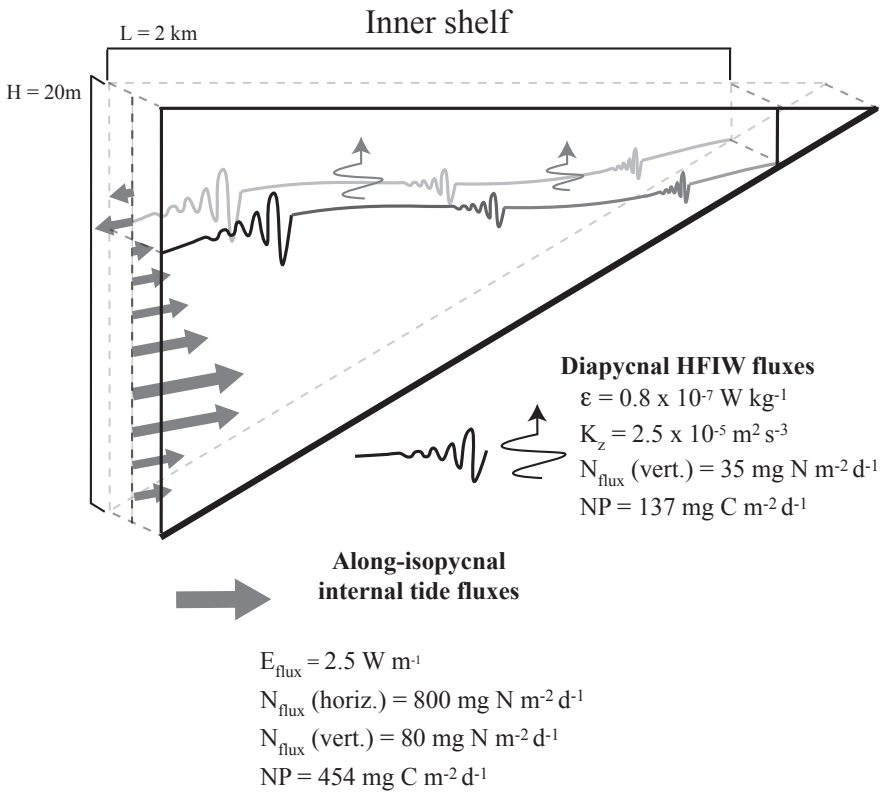

Figure 2.11: Schematic of along-isopycnal and diapycnal internal wave fluxes. The internal tide along-isopycnal nitrate flux over the ISPX experiment is capable of driving all (or an excess) of the new productivity typical of the inner shelf during stratified periods. The diapycnal HFIW flux of nitrate is significantly smaller, although still capable of supporting much of the measured new productivity over the shelf. These estimates are not independent; HFIW dissipation may act to force a portion of the vertical flux of IT horizontally-delivered nitrate, along with the effective vertical component of the along isopycnal flux due to the persistent tilt of the nitracline and mixing in the bottom boundary layer.

3 The green ribbon: physical control of phytoplankton productivity and community structure over a narrow continental shelf

3.1 Abstract

Chlorophyll concentration, phytoplankton biomass, and total and new primary productivity increase dramatically toward the coast over the 10 km wide continental shelf of the southern Southern California Bight. These gradients are accompanied by changes in phytoplankton community composition: the inner shelf is dominated by diatoms and the picoeukarote *Ostreococcus*. Across the small horizontal scale of the shelf, large changes in the vertical distribution and flux of nitrate maintain this persistent narrow band of elevated productivity, driving variability in the vertical distribution of biomass and the integrated biomass and productivity of the entire shelf. Temporal variability from hours to days in chlorophyll fluorescence as measured by an autonomous profiling vehicle demonstrates the capacity of the phytoplankton to respond vigorously and rapidly to physical variability. The interaction of physical processes at different temporal and spatial scales is responsible for these biological gradients. These include: 1) vertical shear in the alongshore currents, 2) local wind forcing, 3) the internal tide and high-frequency internal waves, and 4) remote, large scale forcing. Individual mechanisms rarely or never explain the biomass and rate gradients across the shelf alone.

These results and a re-analysis of historical data suggest new monitoring strategies that may augment our ability to predict phytoplankton rates, community composition and biomass.

3.2 Introduction

Continental shelf seas dominate the global oceanic productivity of marine photoautotrophs, and consequently are characterized by large fluxes of carbon to higher trophic levels and to the sediment (i.e. 'export production'; Eppley and Peterson 1979, Behrenfeld and Falkowski 1997, Behrenfeld et al. 2006). The taxonomic composition of phytoplankton communities is seen as exercising control over export production, in part because large species (e.g. diatoms) efficiently and rapidly transfer fixed carbon out of the euphotic zone (e.g. Michaels and Silver 1988, Boyd and Newton 1999, Bury et al. 2001, Krause et al. 2009). In coastal seas, phytoplankton communities are typically dominated by these large taxa that are adapted to rapid, large inputs of nutrients (e.g. Kudela and Dugdale 2000). Thus, the physical processes that dictate the delivery of nutrients control export production in two ways: 1) by setting the total potential for new productivity (via the bulk input of limiting nutrients) and 2) by influencing the community composition of the phytoplankton.

Long-term changes in the physical dynamics of continental shelf regions have a profound influence on the structure and function of the pelagic ecosystems found there. The global scale, long-term changes in export productivity are well correlated with climatic variability (Behrenfeld et al. 2006). However, recent evidence suggests that changes in primary productivity in some coastal systems are contrary to expectations based on simple global climate change scenarios, including those within the California Current Ecosystem (CCE) (Di Lorenzo et al. 2005, Aksnes and Ohman 2009, Kahru et al. 2009). In the Southern California Bight (SCB)—the southern, inshore portion of the CCE—the depth of the nitracline and the euphotic zone have decreased since 1980, as the mean chlorophyll concentration (Aksnes and Ohman 2009) and vertically-integrated net primary productivity (Kahru et al. 2009) have increased, particularly over the continental shelf. Presently there is no convincing dynamical explanation for the

observed biological changes, though variability in atmospheric and physical oceanographic processes are expected to be causative agents of such change. For example, although increasing sea-surface temperatures and increasing stratification would be expected to suppress nitrate delivery to the euphotic zone of the SCB (Smith and Eppley 1982, Roemmich and McGowan 1995, Di Lorenzo et al. 2005, Kim and Miller 2007), the opposite has occurred, even in the absence of a strengthening in coastal wind-forced upwelling and only weak strengthening of wind stress curl over the SCB (Rykaczewski and Checkley 2008).

The southern SCB (SSCB, south of Santa Monica Bay) ecosystem is an interesting example of a weakly forced system from an atmospheric and oceanographic perspective (Eppley and Holm-Hansen 1986). The strong upwelling favorable winds found north of Point Conception, California and south of Ensenada, Baja California are absent, and currents and temperature over the continental shelf are poorly correlated with local winds (Winant and Olsen 1976, Winant and Bratkovich 1981, Pringle and Riser 2003). Nevertheless, primary productivity, new productivity, and phytoplankton biomass are found to increase inshore, apparently due to oceanographic and not continental processes (Chapter 2, Eppley 1992).

Lucas et al. (submitted, Chapter 2) demonstrated quantitatively that the horizontal and vertical internal wave fields—in particular the internal tide and higher frequency internal waves—provided ample nitrate flux to support the vertically integrated primary productivity over the inner shelf. These fluxes were variable in time due to both fluctuations in the strength of the internal tide and to lower-frequency changes in the water column that impacted the vertical distribution of nitrate concentration and stratification.

Here we use a dataset gathered off Mission Beach, California, in the summer of 2006, to assess the patterns of phytoplankton community composition, primary productivity, and new productivity over the narrow continental shelf of the SSCB in the context of the physical variability found there. We show that over short horizontal (< 10 km), vertical (< 5 m) and temporal scales (< days), there are major changes in the phytoplankton community in terms community composition, nitrate uptake and carbon fixation, and therefore the potential for carbon export. These changes are shown to be a function of physical variability in the system, and, more specifically, to the interac-

tion of forcing mechanisms acting on very different spatial and temporal scales, which, independently, would be unlikely to force the patterns we observed. We discuss these observations in the context of the observed long-term trends in the SCB, and re-analyze some long-term records of physical and biological variability in the SSCB. Given the physical mechanisms and biological variability revealed by the ISPX study, we propose a simple monitoring strategy to better resolve these processes.

3.3 Methods

The ISPX study was conducted between 1- 22 August 2008 off Mission Beach, CA. The following measurements were made:

Cross-shelf biological and physical variability: CTD transects and water sampling

A Seabird 19plus CTD was equipped with a Turner Designs fluorometer and Satlantic ISUS v.2 for nitrate measurements. We conducted 7 cross-shelf CTD transects between 9-17 August 2006. On non-biological sampling days (9, 10, 15, 16 August), we occupied 8 stations between the shelf slope and the inner shelf, with approximately 1.5 km between stations, with the exception of the 15 August transect which focused on the mid- and inner shelf. Profiles were made to 90 m or the bottom, whichever was shallower. Profiles always captured the major vertical gradients in nitrate and chlorophyll.

On three transects (11, 14, 17 August) we acquired water samples at the surface and subsurface chlorophyll maximum (SCM, as determined by the live-wired CTD system). The 11 and 17 August samples were collected at four stations on a 15 km transect with bottom depths of 400, 100, 65, and 25 m. The 14 August 5 km transect was confined to the mid and inner shelf (bottom depths of 65, 50, 25 and 15 m). Secchi depths were obtained at some stations. Water samples were transferred to two 4L acid-washed polycarbonate bottles and placed in a dark cooler. Samples were transferred to the laboratory less than 6 hours after the initial sampling.

Particulate carbon, nitrogen and nutrient analysis

500 ml samples were filtered onto pre-combusted Whatman GF-F filters. Particulate nitrogen (PN) and particulate carbon (PC) were measured at the SIO analytical

facility by gas chromatography using standard techniques. Sample water was decanted into two 40 ml acid-washed Falcon tubes for nutrient analysis and frozen. Nutrient analyses were performed at the Oceanographic Data Facility (ODF), UCSD-SIO.

Nitrogen uptake experiments

Samples were decanted to 8 500 ml acid-washed polycarbonate bottles to provide duplicates for the 4 nitrogen treatments. Treatments were spiked with 100 nM ^{15}N-labeled nitrate, urea, ammonia, and guanidine and incubated for 2 hrs in 25% and 2% surface light intensity for the surface and SCM samples, respectively (surface illumination determined by hand-held PAR sensor). Following 2 h incubations, samples were filtered onto precombusted Whatman GF-F filters, dried under a laminar flow hood, packaged in tin, and frozen. Samples were analyzed at the UC Davis stable isotope facility, using gas chromatography and mass spectrometry, and nitrogen uptake was determined according to the relationship adapted from Dugdale and Wilkerson (1986).

Primary productivity measurements

Samples were decanted into 3 acid-washed 70 ml polycarbonate bottles (duplicate PP incubations and a single dark control), and spiked with 5 μCurie HCO_3^-. Samples were incubated for 6 h at 25% or 2% surface light intensity for the surface and SCM samples, respectively. After the 6 hr incubation, samples were filtered on to precombusted Whatman GF-F filters. The radioactivity of the filters and filtrate were determined with a scintillation counter, giving a percent ^{14}C uptake/time. This percent uptake rate was dark corrected (based on the percent uptake/time in the dark incubation) and was then multiplied by the total available DIC pool size (a function of the temperature and salinity of the sample, citation) to estimate total carbon uptake per unit time and volume.

The primary production and nitrogen uptake experiments were incubated at 25% (surface samples) and 2% (SCM samples) of surface PAR. For both conditions, this likely represents significantly lower light levels than those experienced in the natural environment. However, as the samples spent one to two hours in complete darkness between the time of sampling and the addition of the tracer, these lower light levels were

used to minimize the potential shock of a sudden return to high light. The ratio between incubation irradiances for our surface and SCM samples is likely representative of that in natural conditions. Therefore, while the exact rates themselves may not adequately reflect the natural environment, the relative trends between samples are robust.

Phytoplankton pigment analyses

One liter of seawater was gently filtered onto a Whatman GF-F filter, which was placed in a cryogenic vial and stored in liquid nitrogen until HPLC analysis as described in Goericke and Montoya (1998). For extraction of pigments, the filters were placed in 3 ml acetone, homogenized on ice with mortar and pestle, and allowed to incubate for 2 h (4°C, in the dark) following the addition of an internal standard (canthaxanthin in 50 μl of acetone). Prior to reverse-phase HPLC analysis, the filter extracts were centrifuged to remove cellular and filter debris. Samples (200 μl) of extract were manually injected onto a Waters HPLC system equipped with an Alltech Microsorp C-18 column and a UV-Vis detector (λ=440 nm). A ternary solvent system was employed for pigment separation and HPLC-grade solvents (Fisher) were used to prepare eluents A, B and C: eluent A (MeOH:0.5 mol L^{-1} ammonium acetate, 80:20), eluent B (methanol) and eluent C (acetone). The linear gradient used for pigment separation was (Time in minutes$'$ (% eluent A, % eluent B, % eluent C)): 0.0$'$ (0, 100, 0), 5$'$ (0, 85, 15), 10.0$'$ (0, 70, 30), 14$'$ (0, 20, 80), 16.0$'$ (0, 20, 80), and 18.0$'$ (100, 0, 0). The eluent flow rate was held constant at 1 ml min^{-1}. Eluting peaks were identified by comparing their retention times with those of pigment standards and algal extracts of known pigment composition. Pigments were quantified using external standard curves and the UV-Vis detector was calibrated spectrophotometrically using HPLC-purified pigment standards.

Typical optimization of HPLC data uses the differing ratios of accessory pigments to chlorophyll concentration in a multiple regression to determine the contribution of each taxonomic group to the total chlorophyll concentration (see Goericke and Montoya 1998). We normalized pigment concentration by the total chlorophyll measured from the sample to assess the spatial and temporal gradients of relative contribution of different taxa to the phytoplankton community composition. Although this approach does not permit a quantitative analysis of the community composition of each sample, we expect that particular pigments are diagnostic for the presence of phytoplankton taxa,

e.g. diatoms groups are the primary contributor to fucoxanthin concentration variability, dinoflagellates dominate the peridinin concentration variability, haptophytes dominate 19′-hexanoyloxyfucoxanthin concentration changes, and *Synechococcus sp.* dominate the zeaxanthin concentration changes (confirmed by flow cytometric enumeration of *Synechococcus* counts).

Flow cytometry and qPCR enumeration of picoplankton abundance

One milliliter samples of seawater were dispensed to sterile 1.5 ml cryogenic vials and allowed to fix for 10 min with glutaraldehyde added to a final concentration of 0.25% v/v from a stock of 25% (Sigma Chemicals) prior to immediate storage in liquid nitrogen. The samples were analyzed on a Becton Dickson FACSort flow cytometer using techniques described previously (Collier and Palenik 2003, Worden et al. 2004). Green fluorescent beads (0.9 μm-diameter, Duke Scientific) were added to a final concentration of 25-30 beads μl^{-1} as an internal standard. *Synechococcus* and picoeukarotes (presumably *Ostreococcus spp.* were identified by fluorescence characteristics and enumerated from each sample to provide a final estimate of concentration in cells ml^{-1}.

The abundance of phylogenetically distinct clades of *Synechococcus* were assessed using quantitative PCR (qPCR) exactly as described in Tai and Palenik (2009). The four most commonly found clades in this environment, clades I, II, III, and IV, were enumerated.

Water column structure and variability, fluorescence variability: WireWalker moorings

The WW wave-powered autonomous profiler, (Rainville and Pinkel 2001) was deployed in 22 m of water in association with an ADCP (Fig. 3.1) and sampled the upper 19.5 m of the water column. Battery changes and some data acquisition problems led to several data gaps in the final time series. The WW collected 10,301 vertical profiles with an average upcast velocity of 0.4 m s^{-1} and a 16 Hz sample rate, resulting in a 2.5 cm vertical sample resolution every 2.5 minutes over a 3-week period.

Wirewalker fluorescence correction

Chlorophyll fluorescence is always reported here in units of voltage (the measure of fluorescence) as opposed to putative chlorophyll concentration. Although the instruments were all linear over the chlorophyll ranges we encountered, the variable and important effect of diurnal fluorescence quenching in the upper water column could only be empirically addressed. As we are more interested in spatial and temporal gradients than the precise determination of chlorophyll concentration, we relied on the fact that the instruments all proved to be stable over the course of the experiment, and utilize a fluorescence quenching correction adapted from Todd et al. (2009), based on the covariance of fluorescence and PAR measurements collected at SIO pier. Corrected fluorescence is reported below.

Current structure and variability: Acoustic Doppler Current Profiler (ADCP) moorings

Five bottom-mounted ADCPs were deployed in 32, 22, 17, 12 and 7 m depths (below MLLW) over 24 days, and were configured for 15 s sampling at 3 vertical resolutions: 1 m (32 m and 22 m ADCPs), 0.5 m (17 m ADCP) and 0.25 m (12 and 6 m ADCPs) (Fig. 3.1). Currents were rotated according to local bathymetry (National Ocean Service Hydrographic Data Base). Rotations were all in the clockwise sense between6° and 11° (6°, 30 m; 7°, 22 m; 11°, 16 m; 9°, 12 m; 6°, 6 m). A right-hand frame of reference is used, and currents are reported as alongshore (v; positive ∼northward), cross-shore (u; positive ∼eastward) and vertical (positive upwards).

Subinertial currents

To assess the relationship between local winds and subinertial currents during the ∼3 week experimental period, we calculated the lagged cross-correlation between the alongshore and across-shore components of the SIO Pier wind stress and the three components of current velocity at each depth across the shelf for the longest concurrent record (shared by three instruments, at the 32 m, 22 m and 7 m moorings). Wind stress was calculated as:

$$\tau_{x,y} = C_D \, v_{x,y} |v_{x,y}| \tag{3.1}$$

where C_D is a drag coefficient, taken to be 1 x10^{-3} (the value of C_D does not impact the correlation calculations). $v_{x,y}$ are the across-shore (x) and alongshore (y) components

of the wind (m s^{-1}). The absolute value preserves the direction of the wind in the stress estimate. A right-hand coordinate system was used, where northward (along-coast) blowing and eastward (onshore) blowing winds are positive. The wind and current data were decimated to hourly values and filtered with the pl64t low-pass filter (see Rosenfeld 1983).

3.4 Results

3.4.1 Spatial gradients in biological properties

Persistent gradients in biological properties and rates were observed across the shelf during the ISPX field program. These gradients were observed both at the surface and at the SCM. Surface extracted chlorophyll, particulate carbon (PC), total and new productivity and f-ratio all increased as much as 5-fold from offshore to onshore (Figs. 3.2 and 3.3). These trends were not as pronounced at the SCM. While accessory pigments measured by HPLC analysis in general followed the cross-shelf trends in chlorophyll (i.e. increasing inshore), chlorophyll-normalized pigment concentration indicated these cross-shelf gradients in bulk properties were accompanied by gradients in community structure (Figs. 3.4 and 3.5). In the surface waters, chlorophyll-normalized HPLC pigments showed an increase in the proportional contribution of diatoms and picoeukarotes inshore, with decreasing importance of haptophytes, *Synechococcus*, and pelagophytes, respectively (Fig. 3.4). At the SCM diatoms (fucoxanthin concentrations) were proportionally more abundant inshore, while haptophytes (19'-hexanoyloxyfucoxanthin concentrations) were relatively enhanced offshore.

Synechococcus spp. and picoeukaroyotes (presumably *Ostreococcus* spp., Worden et al. 2004) in surface waters increased from the shelf break inshore on all sampling days. Picoeukarote adundance appeared to covary with diatoms and increased in both number and relative representation in the community between 11 and 17 Aug. *Synechococcus* clades I and IV increased across the shelf on all sampling days (Fig. 3.6) and were the numerically dominant. *Synechococcus* clades. Clades II and III, while numerically far less abundant, showed trends distinct from total *Synechococcus* and total chlorophyll. Clades II and III were most abundant in the warm offshore waters on

11-Aug, were was less abundant by 17-Aug as the offshore waters cooled (Fig 3.6c).

3.4.2 Temporal changes in biological properties

Superimposed on the persistent cross-shelf gradients in biological properties were temporal changes. In particular, there was an increase in extracted chlorophyll, PC and primary productivity from 11 to 17 August. This increase was particularly prominent at the inshore station at both the surface and SCM (Figs. 3.2 and 3.3). The increase in chlorophyll and PC between 11 and 17 August was accompanied by a concomitant increase in diatoms, haptophytes, cyanobacteria and, to a lesser extent, dinoflagellates. Dinoflagellates in particular were absent on 11 August, but had increased by 17 August (Figs. 3.4 and 3.5). The integrated cross-shore abundances of both *Synechococcus* and picoeukaryotes increased between 11 and 17 August. Diatoms were a relatively constant fraction of the total chlorophyll across the shelf on 11 August, but comprised an increased fraction by 17 August, particularly at the inner shelf SCM (Fig.3. 5). The fraction of dinoflagellates increased from 11 to 17 August; this increase was most notable in offshore waters. Picoeukaryotes also comprised a greater proportion of the inner-shelf phytoplankton community on 17 August in comparison to 11 August (Fig 3.4). In contrast *Synechococcus* accounted for proportionately less of the total chlorophyll at all stations by 17 August (Fig. 3.4). *Synechococcus* clade II abundance decreased from 11 to 17 August (Fig 3.6c), while clade III decreased from offshore to onshore on 11 August, and was only present at the offshore station on 17 August (Fig 3.6c).

3.4.3 Cross-shelf CTD sections

The cross-shelf CTD sections revealed a persistent tilt of the pycnocline, SCM and nitracline, shoaling across the shelf from $\sim$25-30 m depth offshore to as shallow as 8 m at the inshore station (Fig. 3.7). The across-shelf tilt of these properties varied between 11-17 Aug, but remained in the same sense. In contrast to the temporal variability of the tilt, the pycnocline, SCM and nitracline shoaled consistently between 11-17 Aug by $\sim$15 m over both the shelf break and outer shelf (12 and 7 km from shore respectively).

3.4.4 The spatial structure and temporal variability of chlorophyll fluorescence over the inner shelf

The WW data set revealed a great deal of variability from minutes to weeks in temperature, salinity, and chlorophyll fluorescence. For the purposes of these analyses, we highlight the low-frequency (days-weeks) variability during the ISPX study. At the beginning of the experiment, surface waters were anomalously warm, with high salinity and low chlorophyll characteristic of subtropical waters (Fig. 3.8) (Reid et al. 1956). After 7-Aug, the temperature and salinity decreased while chlorophyll concentrations in the surface and SCM increased.

The 13.5° C isotherm (shown in white on panel 1 of Fig. 3.9) was taken as the cut-off below which water always had significant nitrate (>1 μmole l^{-1}, Chapter 2). Over the 3-week course of the deployment, the mean position of the 13.5°C isotherm shoaled from >20 m to 7.5 m, leading to an increase in both the vertically integrated nitrate and fluorescence concentrations over the inner shelf.

In order to decouple changes in fluorescence intensity at depth from the vertical displacement of isopycnals due to internal wave motions (Lucas et al. submitted), we examined chlorophyll fluorescence in an along-isopycnal frame of reference (Fig. 3.9, panel c). Between 10-August and 13-August, a weak increase in fluorescence occurred on the 24.5 σ_t isopycnal (panel 3, Fig. 3.9). In deeper waters fluorescence on the 25.25 σ_t isopycnal was extremely low prior to 16-Aug. Subsequently, fluorescence on this isopycnal increased rapidly; this increase was well fit by an exponential curve, with a calculated 'net growth rate' of 0.258 d^{-1} (r^2 = 0.88). This bloom at the SCM was composed of primarily of diatoms, based on qualitative microscopic examination and HPLC analyses of the 17-Aug inner shelf sample.

3.4.5 The role of local winds

The alongshore windstress was weakly upwelling favorable over most of the ISPX experiment. The temporal and spatial structure of cross-correlation between alongshore wind stress and the cross-shore component of velocity was consistent with Ekman upwelling dynamics; however, variability in alongshore wind stress only accounted for

15% of the cross-shore velocity variability (Fig. 10). Alongshore velocity was positively correlated with alongshore wind stress throughout the water column at each mooring. The strongest correlation occurred when the wind led the velocities by$\sim$1 inertial period. Alongshore velocity was intensified in the upper 5 m and was positively correlated with alongshore wind stress ($r > 0.85$) at near zero lag. The across-shore wind stress and across-shore velocity were also highly correlated (>0.6) at near zero lag (Fig. 3.10). The vertical shear in alongshore velocity was strong (0.035 s^{-1}) and dominated by variability in alongshore wind stress (r^2=0.46).

3.5 Discussion

The strong cross-shelf gradients in phytoplankton biomass and community composition found during ISPX are consistent with earlier observations (Reid et al. 1978, Eppley et al. 1979, Eppley 1992), suggesting that these are persistent features of the SSCB. The community composition gradients indicate a shift between low nutrient supply to the surface waters offshore (dominated by cyanobacteria, haptophytes and some dinoflagellates) and a diatom- and picoeukarote-dominated assemblage inshore, typical of enhanced nitrate supply. Here we discuss the mechanisms that control the spatial and temporal variability of nitrate concentration in the shallow waters of the SSCB. The dominant forcings are the internal tide, the local wind, and remote (large-scale) control of the nitracline depth at the shelf break. No individual mechanism accounts for the patterns that we observed: it is the interaction among these physical mechanisms that regulates phytoplankton properties in the region.

3.5.1 Internal tide

Chapter 2 demonstrated that nitrate fluxes forced by the internal tide and high-frequency internal waves were variable but at times capable of accounting for all the new primary productivity over the SSCB inner shelf. The nitrate delivery by the internal tide is predominantly an along-isopycnal process, driving a net flux of nitrate from waters below euphotic zone offshore into the euphotic zone of the inner shelf. This along isopycnal flux serves to replenish the inner shelf nitrate pool which is distributed

vertically through mixing caused by the dissipation of high-frequency internal waves. In particular, due to the persistent tilt of the nitracline across the shelf (Fig. 3.7), the along-isopycnal flux has a vertical component that brings nitrate into the euphotic zone even in the absence of mixing.

3.5.2 Local winds and the cross-shelf tilt of the nitracline

Previous studies could detect little relationship between local winds and either currents (Winant and Olson 1981, Winant and Bratkovich 1981) or temperature (Pringle and Riser 2003) in the SSCB. The results of our ISPX study indicate a weak but significant relationship between local wind and SSCB shelf currents. While the local winds do not drive vigorous coastal upwelling, we show below that they support the persistent and variable cross-shelf tilt of the pycnocline.

On subinertial timescales, we expect that the horizontal gradient in density represented by the pycnocline tilt to be balanced by a vertical shear in the alongshore velocity. This relationship, the thermal wind balance, is written as:

$$f\frac{\partial v}{\partial z} = -\frac{g}{\rho_o}\frac{\partial \rho}{\partial x} \tag{3.2}$$

where f is the Coriolis frequency (7.79 x 10^{-5} s^{-1} in the study area), ρ_o is a reference density (taken to be 1024 kg m^{-3}), g is gravity, and v is alongshore velocity. With observations of the vertical shear in alongshore velocity (v), we can estimate the horizontal (cross-shelf) density gradient and hence isopycnal tilt. We estimated the vertical shear in subinertial v from the 32 m ADCP between the bottom-most bin and the bin 3 m below the surface, forming a daily estimate of the cross-shore gradient in density based on equation 1:

$$\frac{\partial \rho_{est}}{\partial x} = -\frac{\rho_o f}{g}\frac{\partial v}{\partial z} \tag{3.3}$$

The agreement between the predicted $\frac{\partial \rho_{est}}{\partial x}$ and the measured cross-shore gradient of density from the seven CTD transects was good, although the vertical shear tended to slightly underestimate the measured horizontal density gradient (Table 3.1). Thus, the local alongshore wind drove the vertical shear in alongshore velocity (Fig.

3.11), thereby regulating the observed and biologically relevant across-shelf tilt of the isopycnals and nitracline.

3.5.3 Remote forcing of the offshore depth of the nitracline

The time-course of estimated horizontal density gradient and the measured density gradient indicate that the pycnocline tilt, while always shoaling onshore, ranged over nearly order of magnitude on the time scale of a few days (Fig. 3.11, Table 3.1). While this variability is likely to be significant for biological processes on the shelf, the pycnocline slope alone does not control the nitrate availability on the shelf. For example between 11-17 August the shoaling of the pycnocline at the shelf break could not be accounted for by the local wind stress (Figs. 3.10 and 3.11). This shoaling was not evident in the shallow waters of the inner shelf, indicating that the tilt of the pycnocline and nitracline both decreased, contrary to the forcing by the local winds. Remote forcing can drive changes in the depth of the nitracline in the SSCB (e.g. Tegner et al. 1997). This can lead to large changes in the shelf-wide availability of nitrate. For example, on 10-Aug, the nitracline slope (β) was 2.4 x 10^{-3} and the depth of the nitracline at the shelf break was 32.3 m. By 17-Aug, the depth of the nitracline at the shelf break had shoaled to 15.5 m, while β had decreased to 0.3 x 10^{-3} (Table 1). These changes in the tilt and depth of the nitracline alter the proportion of the nitracline above the euphotic zone, thus changing nitrate availability over the shelf. To estimate the euphotic depth, we measured Secchi depths across the shelf on 16-Aug. It is straightforward to find analytical solutions for the area of the nitracline above the euphotic zone (i.e. for 10-Aug, the triangle formed by vertices I, II, II in Fig 3.11, panel b). These solutions relate the slopes of the bottom (α), nitracline (β) and euphotic zone (γ) and the depth of the shelf break ($H_{shelfbreak}$), nitracline (N_{depth}) and euphotic zone (E_{depth}) to the total area of the nitracline above the euphotic zone.

Given the aspect ratio of the shelf (α = 0.01), and the available measurements of the variables above from the seven CTD transects, we found the offshore depth of the nitracline (N_{depth}) had the largest influence on the euphotic zone nitrate pool over the shelf (Table 3.1). For example, although the slope of the nitracline on 17-Aug was very low and the vertical shear in alongshore velocity was also at a minimum, the area

of the nitracline above the euphotic zone was the largest of all such estimates (Table 3.1) due to the offshore shoaling of the nitracline. This shoaling cannot be explained by local winds. We hypothesize instead that the shoaling of the nitracline at the shelf break was due to remote forcing, such as mesoscale dynamics in the SCB or the influence of coastally trapped waves driven by the intense winds off Baja California (Pringle and Riser 2003).

3.5.4 The long term variability of SSCB productivity: insights from the historical record

We can investigate past fluctuations in the physical environment and phytoplankton abundances in the SSCB using historical data sets. Those include the Scripps Institution of Oceanography (SIO) pier long-term temperature record (surface, 1919 to present; bottom, 1927 to present), the SIO pier high-frequency temperature measurements ($\sim$3 m depth, 4 min data since 2005), and the 20 year record of diatom and dinoflagellate species counts collected by W.E. Allen at SIO pier (1920-1939; Sverdrup and Allen 1939).

The W.E. Allen dataset is remarkable for its duration and breadth. The time series has been analyzed previously (see Allen 1936, Sverdrup and Allen 1939, Tont 1976, and Hseih et al. 2005, among others), and the details of the record can be found in Tont (1986). We re-analyzed the Allen time series in order to assess the degree to which variability in the total diatom and dinoflagellate counts can be explained by the concurrent record of surface and bottom temperatures collected at SIO pier. We expect that periods of negative temperature anomalies would correlate with enhanced nitrate availability and therefore high numbers of diatoms and dinoflagellates. We attempted to assess the importance of the time scales of physical variability on the abundance of the two phytoplankton taxa by forming cumulative temperature anomalies, calculated as the sum of the daily temperature anomalies over a window of variable length (from 1 to 5 weeks) preceding each weekly phytoplankton observation (Fig. 3.12, Table 3.2).

Log-transformed diatom and log-transformed dinoflagellate counts (cells L^{-1}) are positively correlated (0.25, $p < 0.01$) with one another over the length of the concurrent record (1930-1939), and both records are significantly negatively correlated with

the SIO pier SST and bottom temperature anomalies (Table 3.2). While both sets of correlations are relatively weak, the diatom time series is more strongly correlated to the surface and bottom temperature anomalies than the dinoflagellate time series (Table 3.2). Stratification, as measured by the difference between the surface and bottom temperature at the SIO pier, was significantly but weakly correlated with diatom and dinoflagellate counts (Table 3.2).

Although the calculated correlations between the SIO pier temperature anomalies and the diatom and dinoflagellate records and are not particularly strong, visual inspection of Fig. 3.12 shows that long periods of elevated bottom temperature anomaly were concurrent with depressed diatom and dinoflagellate counts. For example, during the 1931-1932 El Niño, diatom counts exceeded 5,000 cells L-1 only once in a 62 week period (Fig. 3.13). Over the 20 yr length of the record nearly 42% of all weekly observations exceeded 5,000 cells L^{-1} (21.8 ± 5.2 times per 52 week year, not including 1931, n = 988), while the mean of the entire record was an order of magnitude larger than the 1931 mean. Therefore, prolonged periods of elevated bottom temperature anomaly are associated with very small diatom and dinoflagellate populations over the 1930-1939 period. These observations are consistent with the schematic representation of remote forcing in Fig. 5.1— basin scale phenomena can depress the nitracline to depths > 60 m during strong El Niños (see Fig. 4c in Aksens and Ohman 2009) and effectively cut off nutrient supply to the shelf.

3.5.5 SIO pier temperature: a comparison of the automated and manual record

The correlation between cumulative bottom temperature anomaly at SIO pier and the abundance of diatoms and dinoflagellates in the W.E. Allen is dominated by the long periods of low abundances and anomalously warm waters due to remote forcing. The lack of a stronger predictive correlation between cold temperatures and high abundance of diatoms and dinoflagellates is in part due to the unknown but nonlinear biological interactions among phytoplankton species, grazing by zooplankton, and potential indirect effects between the environmental variability and these biological interactions (Hseih et al. 2005). Nevertheless, the bottom-up forcing of the physical environment clearly sets

limits on the abundance of diatoms and ultimately must be reflected both positively and negatively in a record of their abundance.

One potential issue is that the SIO pier long-term temperature record is an extremely aliased record of the high-frequency variability found at the pier during stratified periods and tends to over-predict the daily minimum and mean temperature at depth and under-predict the maximum daily difference between surface and bottom temperature (Fig. 3.14). We expect that both diatom and dinoflagellate abundances at SIO pier are actually more predictable by temperature then demonstrated by the analysis of the Allen data above due to the aliased and therefore dynamically obscured nature of the long-term record. In particular, a long-term record of the depth and strength of stratification across the continental shelf would likely provide some insight into nonlinear 'bloom and bust' signal in both records.

3.5.6 Interacting scales of physical variability control phytoplankton rates and community structure

The schematic understanding developed in this study suggests that prediction of coastal phytoplankton productivity, community composition and the transfer of fixed carbon to higher trophic levels is tied to the detailed interaction of physical processes on a variety of spatial and temporal scales (Fig. 3.14). For maximum effect, the internal wave engine that powers inner shelf productivity depends on local winds to set up a cross-shore nitracline tilt. These winds are otherwise too weak to consistently replenish nitrate over the inner shelf. The total availability of nitrate to the inner shelf, however, is a function not only of the pycnocline tilt, but also of the offshore depth of the nitracline: deep offshore nitracline depths can cut off nitrate delivery to the inner shelf. The offshore nitracline depth is likely to be responsive to remote forcing on scales ranging from weekly (e.g. coastal trapped waves) to inter-annually (e.g. El Niño) to inter-decadal (e.g. NPGO; Di Lorenzo et al. 2008).

Aksnes and Ohman (2009) showed that, over the course of the last 25 years, the depth of the nitracline has decreased and the integrated chlorophyll concentrations have increased throughout the Bight. Similarly, Kahru et al. (2009), using satellite-derived estimates, have shown that primary productivity has increased in the SCB. Both of these

observations are surprising given the well-documented warming of the California Current and the increase in stratification, which would be expected to decrease the nitrate delivery to the euphotic zone. The temperature record at the SIO pier shows strong evidence of secular warming, and an estimate of 'nitrate availability' based on the long-term temperature record (i.e. observations below 14.5°C) shows a strong decrease over time (Lucas unpubl.).

Although the mechanism for the observed nitracline shoaling is not known, it is likely due to large-scale and not local phenomena. Increased stratification and increased productivity are not necessarily at odds: if the primary nitrate flux during stratified periods is along-isopycnal, forced by the internal tide, the shoaling nitracline would lead to enhanced productivity over the shelf regardless of stratification. In Chapter 2, I showed that the direction of the nitrate flux just above the pycnocline was offshore, even as the mean nitrate flux was strongly onshore. This may represent a horizontal redistribution of nitrate from the inner shelf to offshore waters near the depth of the chlorophyll maximum. The argument was necessarily tentative, and requires further data. It is, however, one hypothesis that may explain the seemingly paradoxical observations of increased stratification and increased primary productivity in the SCB, in particular given the lack of locally increased coastal wind forced upwelling (Rykaczewski and Checkley 2008).

3.5.7 A simple monitoring framework

Recent, commendable efforts to establish Coastal Ocean Observing Systems (e.g. the Southern California Coastal Ocean Observing System, SCCOOS, www.sccoos.org) have been predicated on the stated goal of increasing our capacity to predict changes in the coastal ocean ecosystem. The findings of this study suggest slightly revised monitoring strategies that potentially would enhance the predictability of phytoplankton biomass, productivity, and community structure. Given that the depth and slope of the nitracline exercises strong control over the nitrate flux potential of the internal tide, and that, for much of the year, the internal tide flux supports much if not all of the nitrate utilization in coastal areas of the SSCB, we suggest that the monitoring should include vertically well-resolved temperature measurements at the shelf break and mid-shelf. These measurements are relatively easy and inexpensive to gather and

transmit real-time. The temperature-nitrate relationship in the SCB is such that a very good estimate of the nitracline depth, nitracline slope, and integrated nitrate content of the euphotic zone could be made from solely from temperature. Such a record, if available for a relatively long period of time, would help address currently open questions including the role of local wind in determining the depth and slope of the nitracline over time scales longer than those assessed here, and could be used to drive predictive models of inshore phytoplankton biomass, productivity, and, potential, community composition and the relative export production potential of the SSCB continental shelf phytoplankton assemblage.

Table 3.1: The measured across-shelf gradient in density ($\frac{\partial \rho}{\partial x}$) and the predicted across shelf density gradient from the thermal wind relationship ($\frac{\partial \rho_{est}}{\partial x} = -\frac{\rho_o f}{g}\frac{\partial v}{\partial z}$). The measurements of density and nitricline depth were gathered on cross-shelf CTD transects. N_{shelf} is the depth of the nitracline at the shelfbreak (depth =120 m), and $N_{inshore}$ is the nitracline depth at the innermost station sampled on each transect. β is the slope of the nitracline. The vertical shear in alongshore velocity (v) was estimated from low-passed near-surface and bottom velocities at the 32 m ADCP. 'Nitrate area' is the proportion of the shelf euphotic zone below the nitracline, as explained in the text. *- Inner-shelf transects (14-Aug and 15-Aug) started at mid-shelf (65 m depth), and nitrate area calculations are not included as those transects did not span the shelf.

Date	$-\frac{\rho_o f}{g}\frac{\partial v}{\partial z}$	$\frac{\partial \rho}{\partial x}$	N_{shelf} (m)	$N_{inshore}$ (m)	β	nitrate area (%)
09-Aug	2.0 x 10^{-5}	7.6 x 10^{-5}	25.1	8.8	1.7 x 10-3	0.25
10-Aug	1.3 x 10^{-5}	7.5 x 10^{-5}	32.3	9.6	2.4 x 10-3	0.09
11-Aug	3.2 x 10^{-5}	6.5 x 10^{-5}	30.6	10.2	2.2 x 10-3	0.10
14-Aug	3.1 x 10^{-5}	3.7 x 10^{-5}	12.2*	14.7	-0.52 x 10-3*	xx
15-Aug	4.8 x 10^{-5}	7.5 x 10^{-5}	13.6*	11.0	0.53 x 10-3*	xx
16-Aug	3.0 x 10^{-5}	8.6 x 10^{-5}	27.5	10.3	1.8 x 10-3	0.17
17-Aug	0.97 x 10^{-5}	0.44 x 10^{-5}	15.5	12.7	0.3 x 10-3	0.39

Table 3.2: Correlation of diatom and dinoflagellates at SIO Pier, 1920-1939, with the SIO Pier surface and bottom temperature records. The diatom time series mean, maximum and standard deviation and correlations were calculated using weekly data from 1920-1939 (correlation with bottom temperature (botT) anomaly and cumulative botT anomaly from 1927-1939). Dinoflagellate time series data from 1930-1939 were used in all calculations due to the change in methodology after 1928. All correlations are significant at $p < 0.01$.

				correlations (r)		
	mean	max	std. dev.	SST	botT	cum. botT, window
diatoms	4.6×10^4	1.39×10^6	1.5×10^5	-0.35	-0.32	-0.35, 10 d
dinoflagellates	2.1×10^4	9.1×10^5	7.3×10^4	-0.22	-0.22	-0.31, 25 d

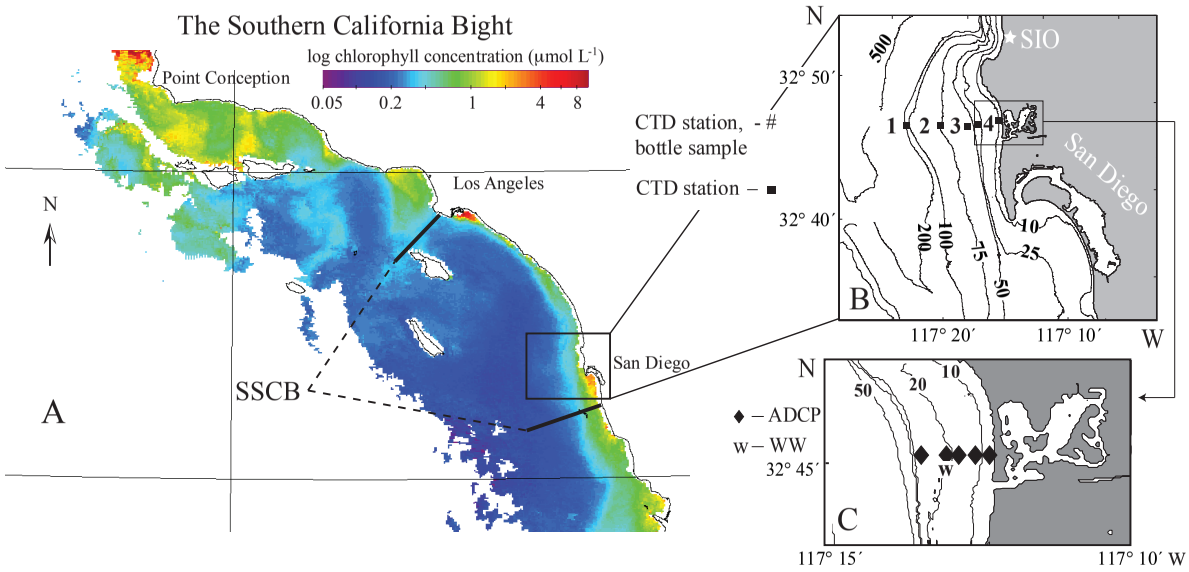

Figure 3.1: Panel A: SeaWIFS 5 day composite image of chlorophyll a in the Southern California Bight for 14-August to 18-August, 2006. The southern SCB (SSCB) region extends from the Palos Verdes peninsula to the upwelling system south of the United States–Mexico border. Chlorophyll concentrations were elevated in a narrow band over the continental shelf. This image is typical of chlorophyll a images in the region during stratified summer months (see Eppley 1992 for similar images). Panels B and C: ISPX study area. The upper panel shows the locations of the cross-shelf CTD and water sampling transects. The total transect distance is ∼15km (from >400 m to 30 m depths). The lower panel shows the location of the inner shelf array of ADCPs and WW profiling moorings. The cross-shelf nitrate flux measurements are made at the ADCP-WW pair.

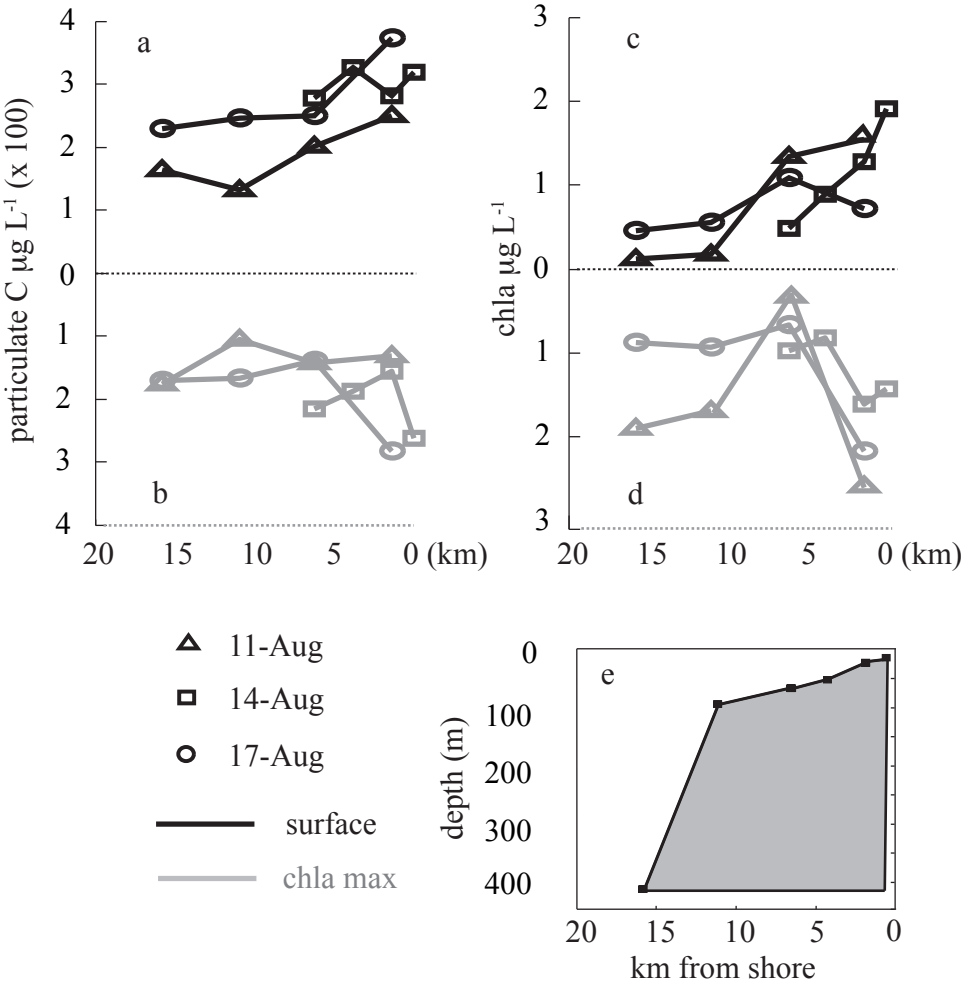

Figure 3.2: Cross-shore trends in particulate carbon (a,b) and chlorophyll concentrations (c,d) across the continental slope and shelf (e). Particulate carbon and chlorophyll were taken together as a qualitative estimate of phytoplankton biomass. Data from the surface ($\sim$2 m) in panels a and c demonstrated the increase in phytoplankton biomass across the shelf. The cross-shore variability in SCM samples (b, d) was dominated by enhanced phytoplankton biomass over the inner shelf station.

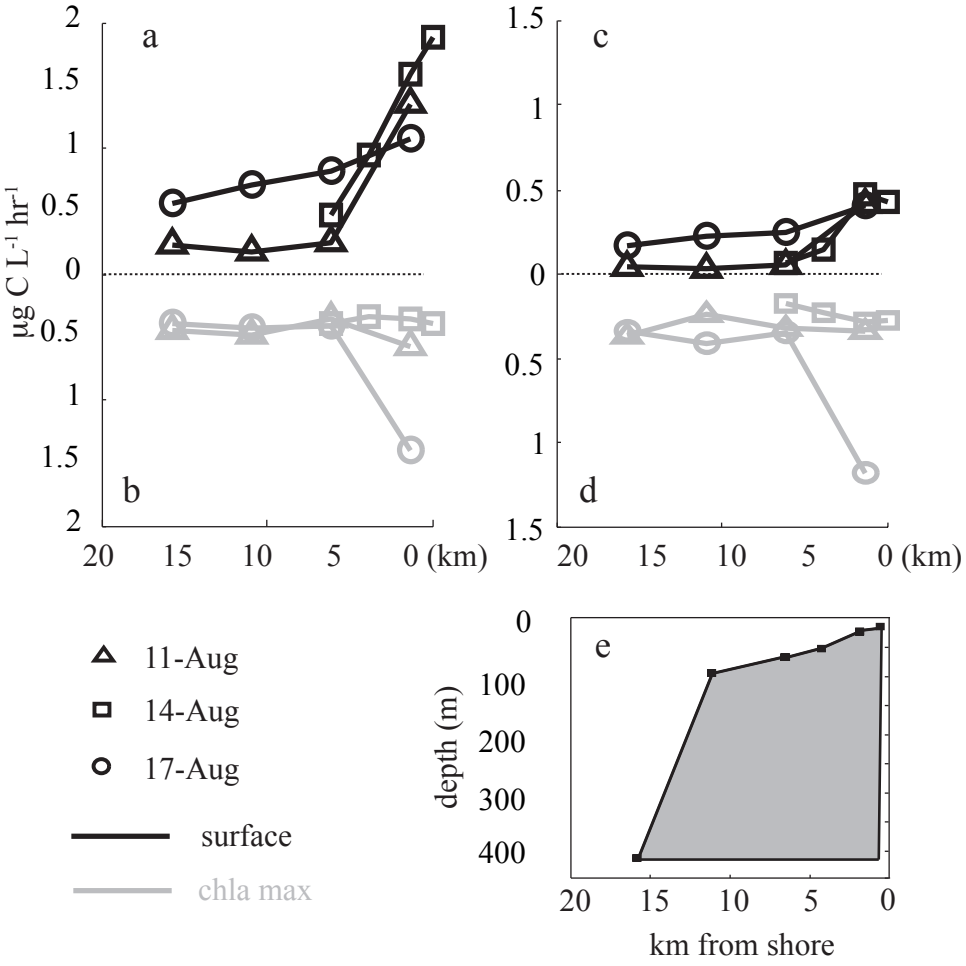

Figure 3.3: Cross-shore trends in total primary productivity (a,b) and new productivity (c,d) across the continental slope and shelf (e). New productivity was calculated as the product of the f-ratio, determined from the nitrogen incubation experiements, and total productivity. Data from the surface ($\sim$2 m) in panels a and c demonstrated the cross-shore gradient in total and new productivity and surface enhancement of productivity relative to the SCM. On 17-Aug, SCM total and new producity peaked, associated with the onset of a subsurface diatom bloom.

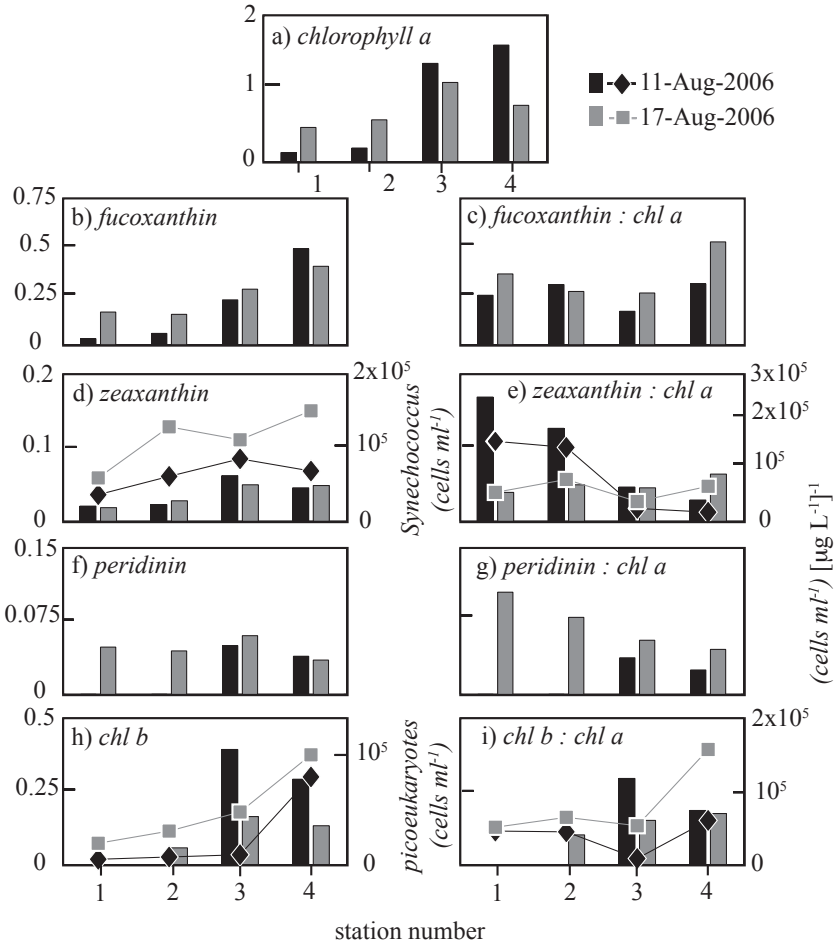

Figure 3.4: Auxiliary pigment concentrations and picoplankton abundance across the shelf in the surface waters on 11-Aug and 17-Aug. Stations 1 through 4 were offshore to onshore as in Fig. 3.1. Panel a represents the chlorophyll concentrations across the shelf. The left column is raw auxillary pigment concentrations (pigment μg L^{-1}) or picoplankton counts (cells ml^{-1}, righthand y-axis on panels d and h). The right column is the chlorophyll normalized auxillary pigment concentrations ([pigment μg L^{-1}] [chl μg $L^{-1}]^{-1}$) or picoplankton abundance (cells ml^{-1} [chl μg $L^{-1}]^{-1}$, righthand y-axis on panels e and i) Chlorophyll normalized pigment concentrations indicated that picoeukarotes and diatoms comprised a relatively larger proportion of the phytoplankton assemblage inshore which increased between 11-Aug and 17-Aug, as the *Synechococcus* and dinoflagellate contribution decreased.

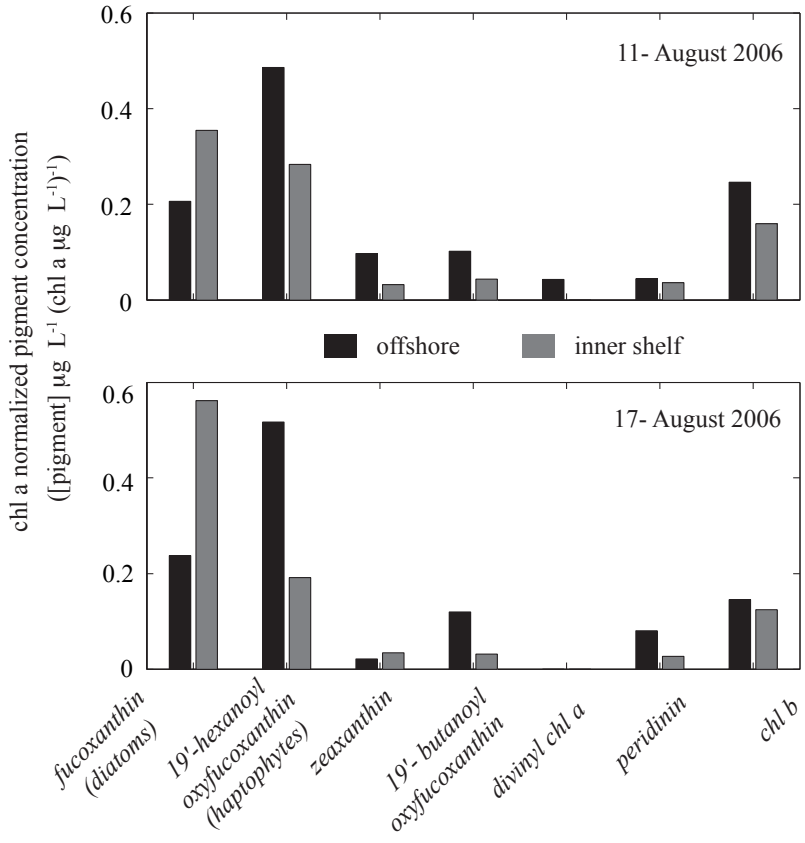

Figure 3.5: Chlorophyll-normalized SCM auxuliary pigment concentrations at the outermost and innermost stations (stations 1 and 4, Fig. 3.4) on 11-Aug and 17-Aug. Diatoms (fucoxanthin) were relatively more important over the inner shelf while haptophytes (19′-hexanoyloxy-fucoxanthin) were relatively more dominant in offshore waters. The 17-Aug inner shelf sample, taken at the beginning of a subsurface bloom, was dominated by diatoms.

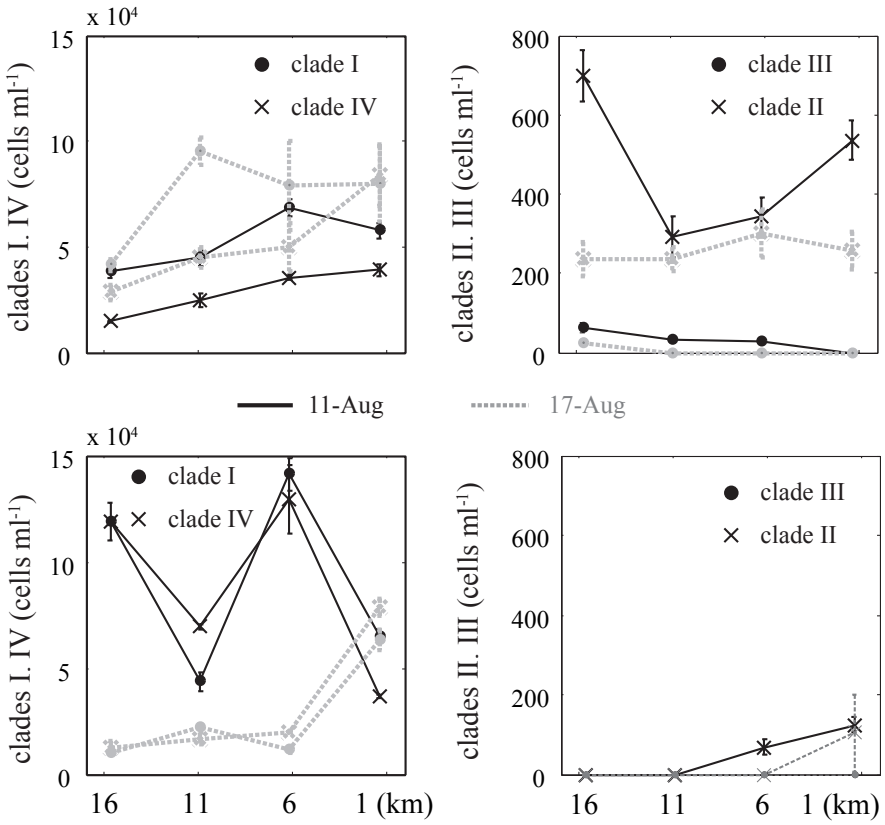

Figure 3.6: qPCR-based *Synechococcus* clade enumeration. Distance was measured from the innermost station as in Fig. 3.2 and Fig. 3.3. The shelf break was at approximately 12 km. Clades I and IV were numerically most abundant and follow the total *Synechococcus* trends estimated from flow cytometeric enumeration (Fig. 3.4). Clades II and III decreased from offshore to onshore, and between 11-Aug and 17-Aug; these clades appeared to prefer offshore oligotrophic waters and decreased in abundance as the nitracline shoaled over the course of the experiment.

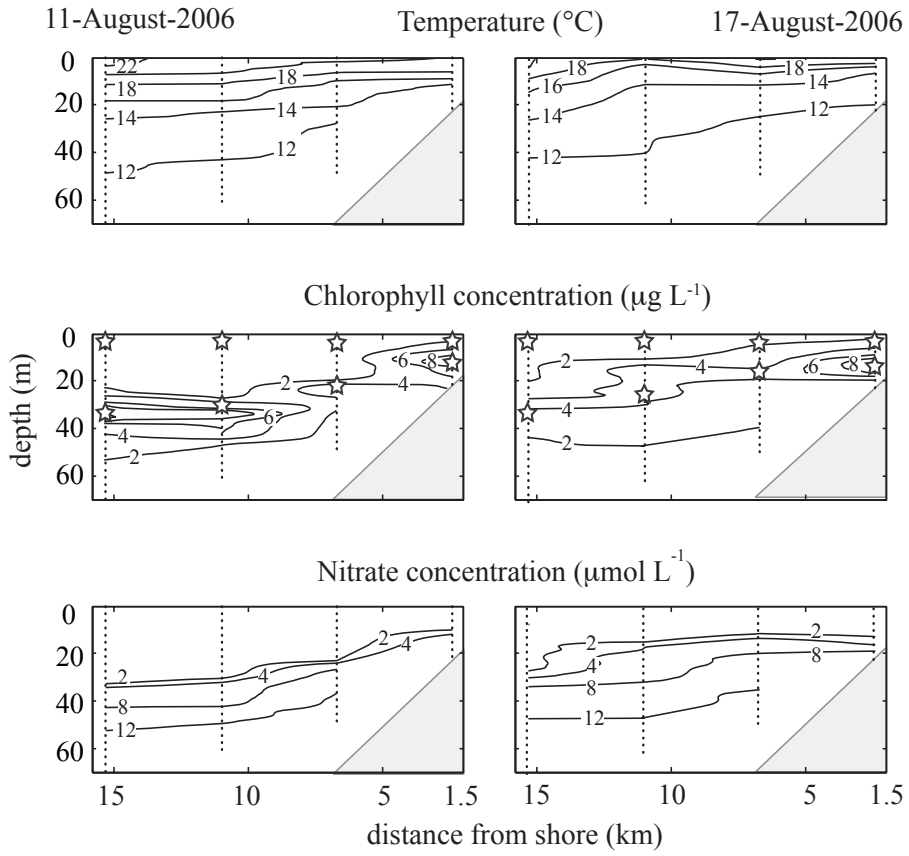

Figure 3.7: Cross-shelf transects of temperature, chlorophyll concentrations, and nitrate as measured by the ISUS in situ nitrate sensor. Open stars show the depths and locations of the water sampling for nutrient determination and primary productivity and nitrogen uptake experiments. A strong chlorophyll maximum is present in all casts; the chlorophyll maximum and nitricline are shallower over the inner shelf than offshore. This cross-shelf shoaling of the nitracline was apparent in all cross-shelf transects (Table 3.1)

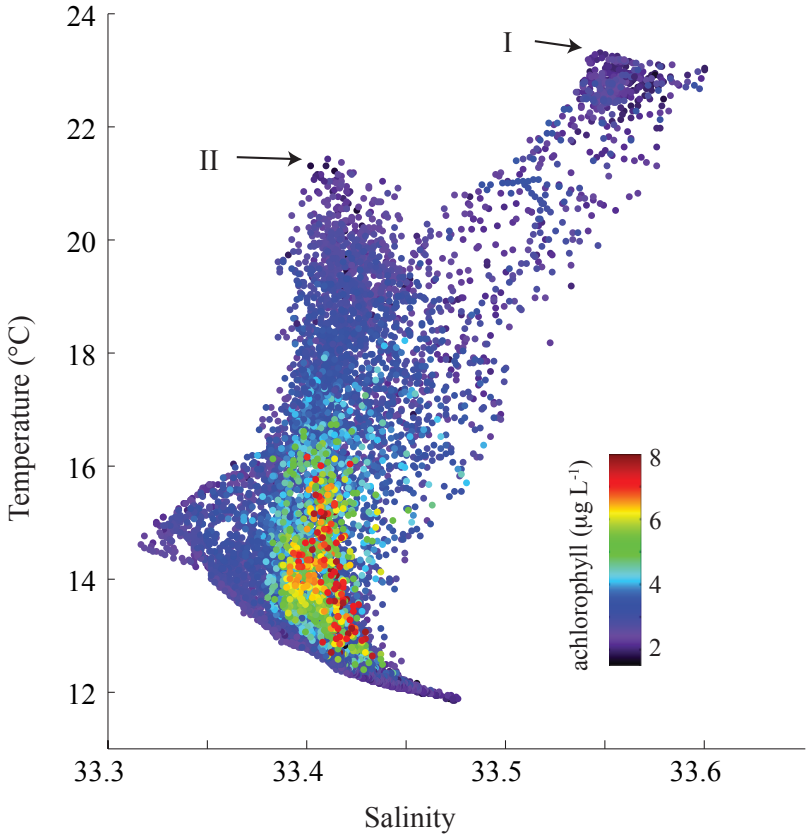

Figure 3.8: Temperature-salinity-fluorescence diagram based 10,301 WW profiles. Approximate chlorophyll concentrations based on factory calibration are shown for reference. Period I was notable for the warm temperatures, high salinity values, and near zero fluorescence, and was likely derived from subtropical sources. Period II was more typical summer conditions over the inner shelf. The highest chlorophyll values, found in the SCM, were primarily observed in waters likely to contain significant nitrate concentrations (e.g. T < 14.5°C and S > 33.35)

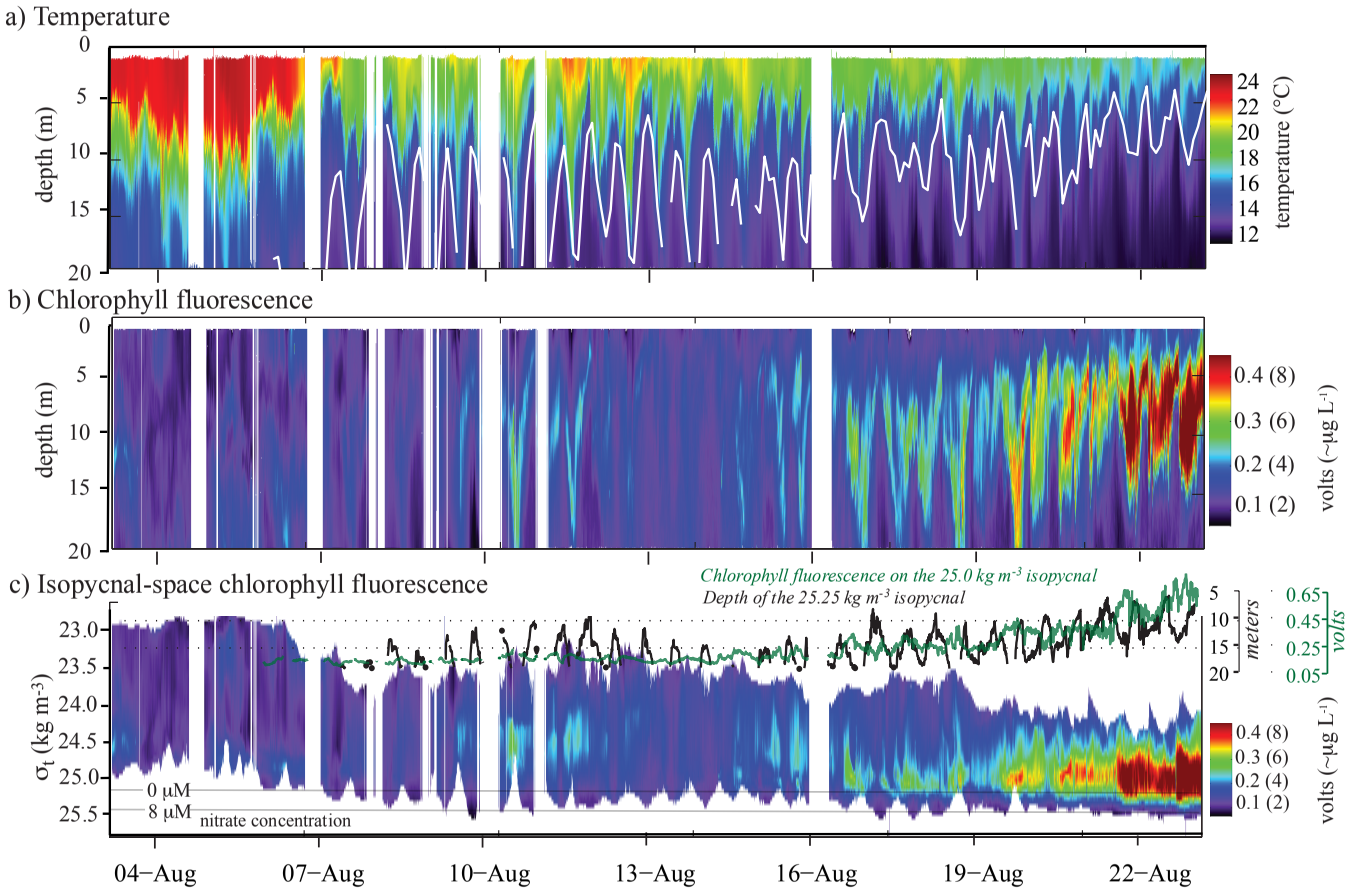

Figure 3.9: Temperature, fluorescence, and along isopycnal fluorescence from the 22 m Wirewalker profiler. The 22 m WW profiler was deployed over a period of 3 weeks. Data have been gridded to 0.25 cm by 10 min bins (panels a and b) and 0.1 kg m^{-3} by 10 min bins (panel c). The white line in panel a is the 13.5°C, at or below which waters have nitrate concentrations > 2 μmol L^{-1}. Putative chlorophyll values based on factory calibrations are provided for reference.

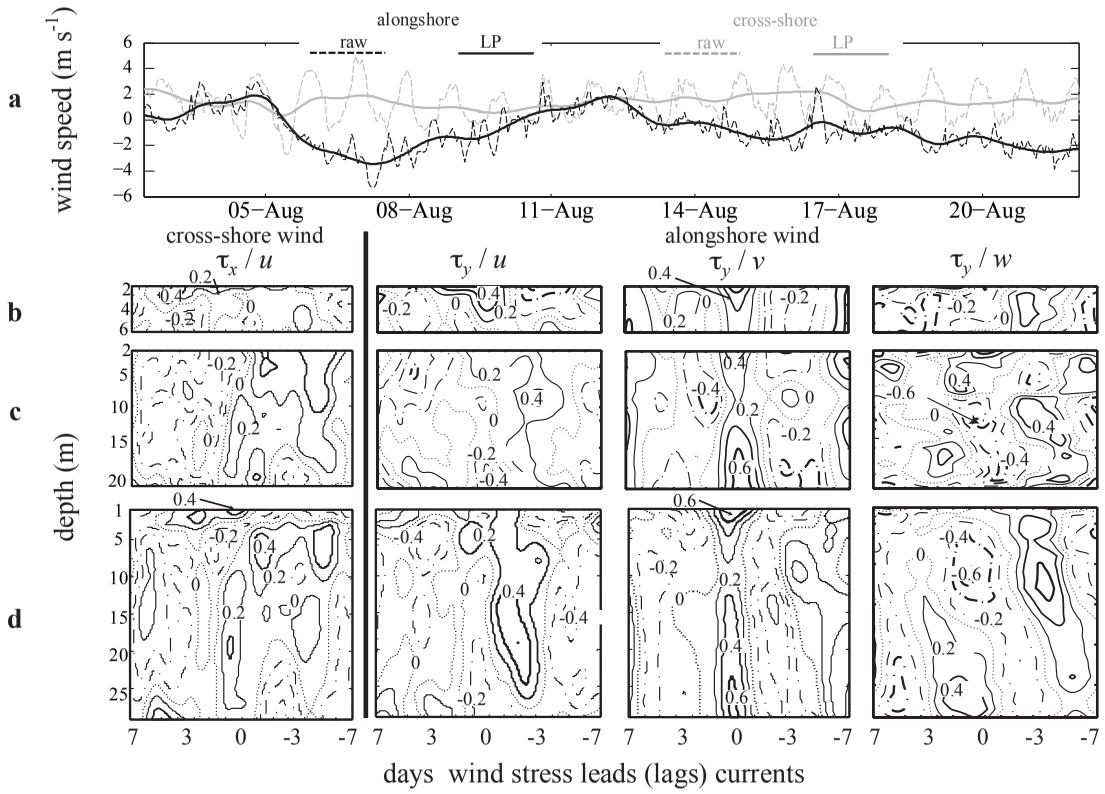

Figure 3.10: The spatial and temporal structure of correlation between wind stress and currents over the inner shelf. Panel a shows the across-shore and alongshore wind stress as hourly (raw) and low-passed (LP) values. Panels b, c, and d are the vertical and temporal wind-current correlation structure at the 7 m, 22 m, and 32 m ADCP moorings. The very near-surface velocity (< 2 m) was directly forced by the wind. Below 2 meters, the correlation structure was as expected from Ekman dynamics, with the lag for the best correlation between along-shore and across-shore flow and alongshore stress decreasing inshore. Both the subtidal cross-shore flow and the correlations with the alongshore wind were weak. Ekman dynamics, over this period, were responsible for very weak cross-shore transports.

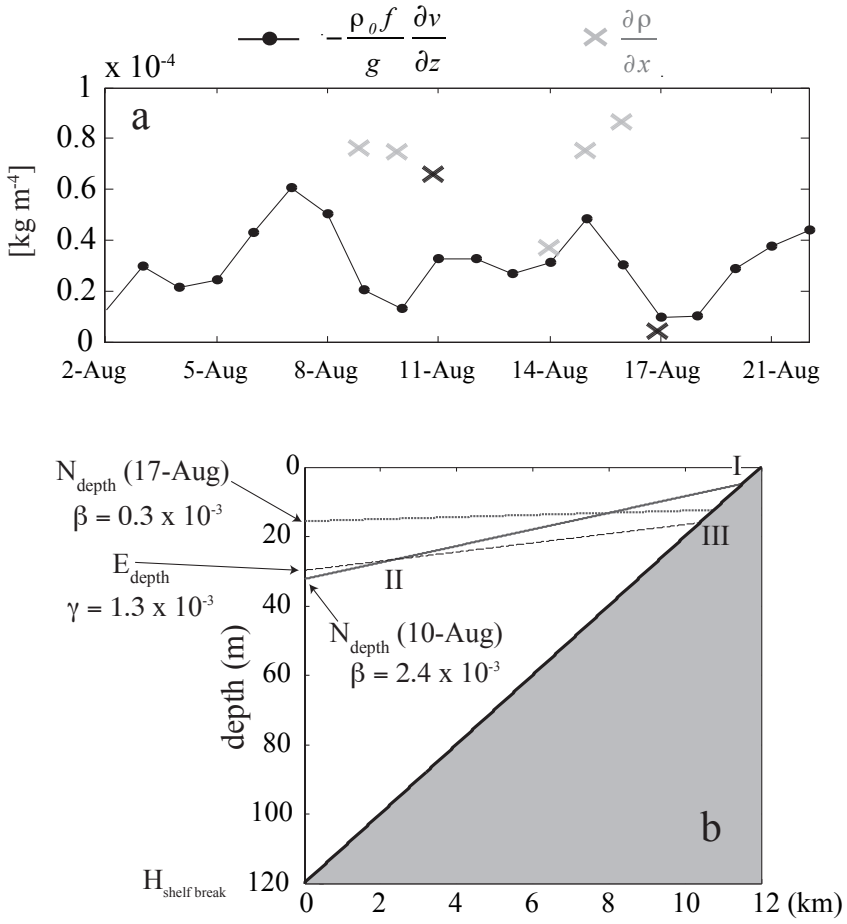

Figure 3.11: Panel a. A comparison between estimated and calculated horizontal gradients in density. The vertical shear in alongshore velocity over the shelf was capable of supporting much of the observed pycnocline tilt. Panel b: schematic representation of the shelf, with linear estimates of the slope (β) and offshore depth of the nitracline (N_{depth}) on 11-Aug and 17-Aug, in comparison to the slope (γ) and offshore depth (E_{depth}) of the euphotic zone. The proportion of the euphotic zone below the nitricline on 11-Aug was estimated as the ratio of the area of the triangle with vertices I, II, III and the total euphotic zone area. This schematic analysis indicates how vertical shear in alongshore velocity, tilt of the nitracline, and the offshore depth of the nitracline combine to drive variability in the integrated nitrate concentration of the euphotic zone. N_{depth} is dominated by remote forcing.

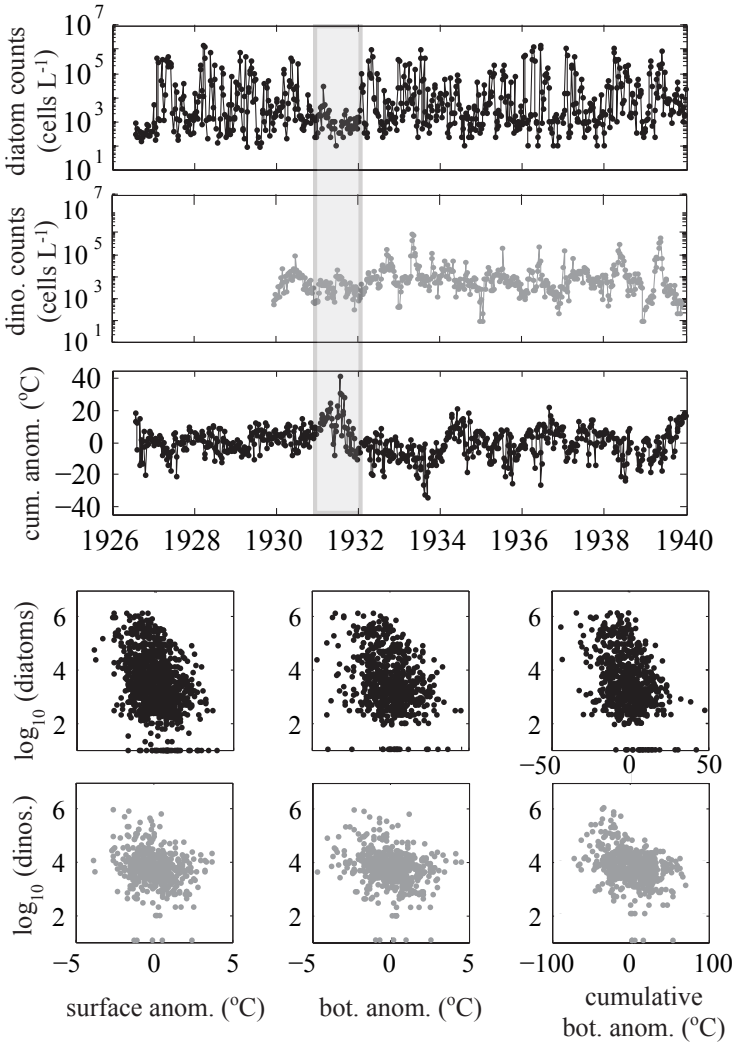

Figure 3.12: The W.E. Allen diatom and dinoflagellate time series and SIO pier temperature anomalies. The time course of log-transformed diatom and dinoflagellate counts showed coherence with the cumulative bottom anomaly (calculated with an 18 d window (Table 3.2)), in particular during extended warm anomalies, such as during the 1931-1932 El Niño (shaded), when both diatom and dinoflagellate numbers were far below their mean abundances (Table 3.2). The lower panels are scatter plots of temperature and cumulative temperature anomalies versus log-transformed diatom and dinoflagellate abundances. Correlations and optimal window sizes are reported in Table 3.2.

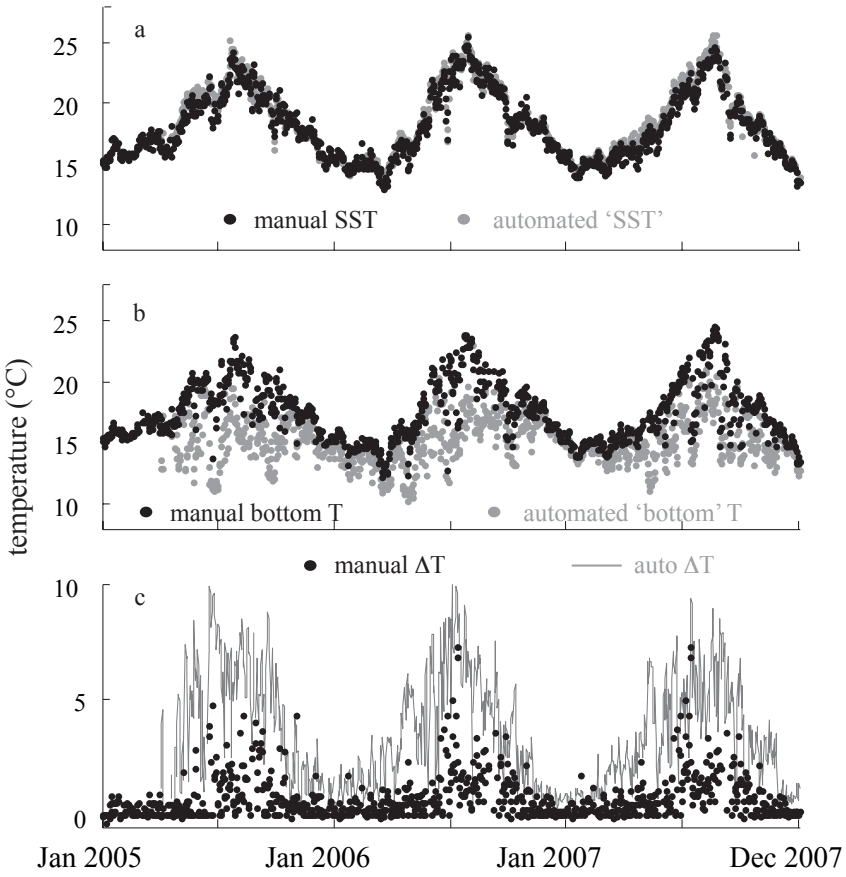

Figure 3.13: Comparison of the once daily manual SIO Pier surface and bottom temperature time series and the automated record gathered at ∼4.5 m since April 2005. Daily maximum, minimum and difference (max-min) values from the automated record are plotted against the once daily surface (panel a), bottom (panel b), and surface/bottom difference (panel c). The daily record of bottom temperature was extremely aliased by high-frequency variability, and was biased high relative to the automated record. This in turn indicated that the once daily record was not a good proxy for nitrate availability in the SSCB nearshore.

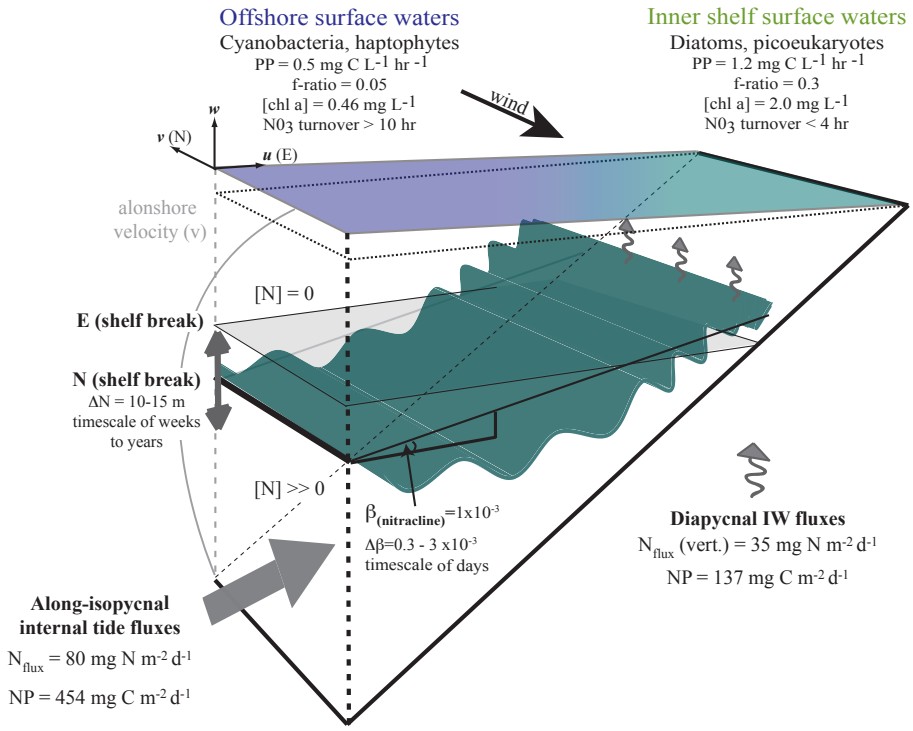

Figure 3.14: Schematic of the physical processes that control inner shelf productivity, phytoplankton biomass, and phytoplankton community composition over the shelf. The across-shore tilt of the pycnocline and nitracline are maintained by the vertical shear in subinertial alongshore velocity due ultimately to the local wind. Along isopycnal nitrate flux is dominated by the internal tide, and nitrate is redistributed vertically by the dissipation of high-frequency internal waves and bottom boundary layer processes. Remote forcing controls the offshore depth of the nitricline. Inshore phytoplankton communities are more productive than offshore waters and are dominated by taxa like diatoms adapted to enhanced nitrate flux. Large-scale forcing impacts the continental shelf phytoplankton community by modulating the depth of the nitracline offshore. During warm anomalies such as El Niño, reduced nitrate supply to the shelf causes low phytoplankton production. Decadal scale shoaling of the nitracline due to large scale forcing (e.g. wind stress curl) could account for the observations of a secular increase in phytoplankton biomass and productivity over the last $\sim$20 years.

4 The semidiurnal baroclinic variability over the Southern California Bight inner shelf

4.1 Abstract

The semidiurnal band variability of currents and density over the Southern California Bight (SCB) inner shelf was investigated using a simple theoretical framework and a set of field observations. This effort was motivated by inconsistencies between recent field observations and the long-standing view of the internal tide as a remotely generated, propagating, low-mode internal wave. We found that, in waters $<$20 m depth, the semidiurnal tidal velocities were counter-rotating at the bottom and surface, effectively precluding interpretation of semidiurnal variability as resulting from either a propagating or standing low-mode internal wave. Simple, two-layer linearized cross- and alongshore momentum balances indicated the importance of rotation, friction, and the cross-shore and along-shore gradients in sea surface slope in forcing the observed semidiurnal variability in inner shelf currents. The cross-shore transport was well correlated with the imbalance between the estimated cross-shore sea level gradient and the Coriolis force associated with alongshore transport of each layer. This imbalance arose from the vertical shear in alongshore velocity. Frictional effects were important, particularly in controlling the phase of the cross-shore transport in the bottom layer. There were inconsistencies between the observed and predicted magnitude and phase of the cross- and alongshore transports which were not satisfactorily explained by the avail-

able data. Nevertheless, over the inner shelf, these data suggest that the baroclinic tide may be forced by local processes and not exclusively driven by propagating or standing low-mode variability as previously envisioned.

4.2 Introduction

Observations of large temperature fluctuations on semidiurnal time scales in the southern Southern California Bight (SSCB) date back 50 years (Arthur 1954, Cairns 1967). Winant (1974) described this temperature variability as resulting from baroclinic tidal currents, and suggested that the internal tide represented a propagating, mode-one internal wave, generated by the interaction of barotropic tidal currents with bathymetric relief, such as undersea banks or the shelf-break, as had been proposed by Rattray (1960).

Winant and Bratkovich (1981) and Lentz and Winant (1986) provided a detailed analysis of current and temperature measurements gathered off Dar Mar, CA in 1978-1979. They showed that semidiurnal variability in currents and temperature lacked a consistent phase relationship barotropic tide. The poor correlation between the observed baroclinic variability and the regular astronomical forcing of the surface tide indicated that the baroclinic tide was remotely generated and propagated onto and across the shelf, losing its deterministic phase relationship with the original barotropic forcing due to variable background currents and temporal/spatial variability in stratification.

Lerczak (2000) and Lerczak et al. (2003) provided the most comprehensive analysis of semidiurnal variability in the SCB to date. They concluded that the baroclinic internal tide over the shelf was "mode one-like," but was neither a purely progressive nor a purely standing wave (Lerczak et al. 2003). Rather, they reported that the semidiurnal variability appeared to be a combination of standing and progressive waves where a variable reflection coefficient between different deployments was attributed to variable sub-inertial coastal flow fields and seasonal or interannual changes in stratification. Furthermore, Lerczak (2000) demonstrated that baroclinic semidiurnal variability was, in fact, as highly correlated with the surface tide as is possible given the bandwidth of the baroclinic semidiurnal variability.

Although Lerczak (2000) and Lerczak et al. (2003) interpreted the baroclinic tide as remotely generated (even hazarding a guess to its source), they indicated that the results of their analysis were not entirely consistent with a simple mode-one internal wave interpretation.

More recently, Winant (2007, unpubl.) investigated the response of three dimensional unstratified flow in a narrow, rotating basin to barotropic tidal forcing. Solutions to the non-dimensionalized equations of motion resulted in an energetic baroclinic lateral circulation under conditions of moderate friction. The baroclinic response was 180° out of phase from the surface to the bottom, and reversed sign with the phase of the barotropic tidal forcing. A similar phenomenon was observed in the currents and temperature of the Strait of San Juan de Fuca (Martin et al. 2005). Ekman transport in the bottom boundary layer resulted from an imbalance between the Coriolis force associated with the cross-strait sea level gradient and the Coriolis force associated with the vertically sheared along-strait velocity. A notable characteristic of this type of flow was that the surface and bottom velocity vectors were counter-rotating relative to one another (Winant 2007).

A narrow continental shelf such as that found in the SCB forms an approximately wedge-shaped domain, and the barotropic tidal currents are predominately oriented along-shelf (analogous to the axial direction in the Winant model; Munk et al. 1970). Given the ambiguity in the current understanding of the baroclinic internal tide over the SCB (Lerczak et al. 2003), the possibility that long-shelf flow could produce a complimentary baroclinic lateral flow in the absence of an energetic internal wave field (e.g. Martin et al. 2005, Winant 2007), and that the vertically reversing alongshore to cross-shore polarization inherent to the rotation-driven case is exclusive of a mode-one internal wave, we assessed the possibility that the baroclinic flow over the SCB inner shelf was driven directly by the barotropic flow due to the surface tide. The hypothesized forcings are shown in schematic form in Figure 4.1, which follows the observations of Martin et al. (2005) and the model of Winant (2007).

In the summer of 2006, we deployed a set of moorings, including bottom-mounted ADCPs and autonomous profiling CTDs, off Mission Beach, California. Here we show that the variability in currents at 5 locations across the shelf was dominated by semid-

iurnal band variability. Through complex empirical orthogonal decomposition of time series of cross- and alongshore velocities, we demonstrate that surface and bottom velocities were in fact counter-rotating on a alongshore/cross-shore plane in the shallow water of the inner shelf ($\sim$<15 m), effectively ruling out a propagating, mode-one internal wave. A dynamical analysis of the appropriate momentum equations indicated the importance of rotation in the momentum balance, and that, when viewed as a two layer system, the currents appeared to behave in a fashion analogous to that found in Winant (2007). The alongshore flow was well modeled by the estimated alongshore sea surface slope due to the barotropic tide, modified by friction and possibly the nonlinear advection of momentum. The two-layer cross-shore flow was induced by the imbalance of rotational acceleration of the alongshore flow and the horizontal component of sea surface slope. Although our arguments are necessarily tentative due to the limited data analyzed here, we suggest that the semidiurnal baroclinic variability observed over the shallow inner-shelf of the SCB is not a propagating internal wave feature, but is instead a direct baroclinic response to barotropic tidal forcing.

4.3 Theory

In the case of an inviscid, cross-shore propagating mode-one internal wave, the linearized momentum equation is:

$$v_t + fu = 0 \tag{4.1}$$

This balance dictates that the cross-shore velocity is 90° out of phase with the long-shore velocity and is clockwise polarized at all depths (Lerczak et al. 2003). The solutions to the linear, rigid-lid Boussinesq equations (Wunsch 1969) with the approximate geometry and the typical buoyancy frequency profile over the SSCB shelf results in u and v velocities that are each exactly 180° out of phase between the surface and bottom (Lerczak 2000).

Lerczak (2000) showed that the baroclinic residuals of alongshore and cross-shore velocity were clockwise polarized at all depths. However, since the primary semidiurnal variability in alongshore velocity over the SSCB shelf did not have a zero

mean with depth, an analysis that concurrently explores the barotropic and baroclinic components is preferable.

Below we develop simplified momentum balances in the cross- and alongshore dimensions. These balances include local forcing from the barotropic tide, rotation, and friction as the primary terms, and are shown to explain much of the observed variability over the inner portion of the shelf.

A right-hand frame of reference was used, and currents were alongshore v (positive ∼northward), cross-shore u (positive ∼eastward) and vertical w (positive upwards).

4.3.1 Alongshore momentum balance

We investigate the alongshore momentum balance using a one layer model (Figure 4.2).

$$\frac{\partial v}{\partial t}+\left[u\frac{\partial v}{\partial x}+v\frac{\partial v}{\partial y}+w\frac{\partial v}{\partial z}\right]+fu=-g\eta_y+\frac{\tau_s-\tau_b}{\rho_o H} \tag{4.2}$$

where u and v are the cross and alongshore components of velocity, η_y is the alongshore slope of sea surface height (due to the baroclinic tide), ρ_o is a reference density for the layer, H is the depth of the water column, f is the Coriolis frequency and τ_s, and τ_b are surface and bottom stresses.

Integration of the alongshore momentum equation

We integrate the alongshore momentum equations vertically and horizontally between the moorings to obtain an expression for alonshore momentum. We ignore the nonlinear terms and integrate equation (4.2) vertically from the surface to the bottom and across the array.

$$\begin{aligned}\frac{\partial}{\partial t}\int_0^{X_{in}}\int_{-H}^{0}v(z)\,dz\,dx+f\int_0^{X_{in}}\int_{-H}^{0}u(z)\,dz\,dx=\\ -g\eta_y\int_0^{X_{in}}\int_{-H}^{0}dz\,dx+\frac{\tau_s-\tau_b}{\rho_o H}\int_0^{X_{in}}\int_{-H}^{0}dz\,dx\end{aligned} \tag{4.3}$$

Equation (4.3) simplifies to

$$\frac{\partial}{\partial t}\mathbf{V} = \left[-gH\eta_y - \frac{\tau_b}{\rho_o}\right]X_{in} + f\mathbf{U} \tag{4.4}$$

where **V** and **U** are the alongshore and cross-shore transports respectively. Surface stress is assumed to be zero.

We do not have direct measurements of the alongshore slope of the sea surface height (η_y), so we estimate η_y based on the Munk et al. (1970) consideration of the barotropic tide in the Eastern Pacific. We considered a linear combination of waves at the K_1 and M_2 frequencies (1.16×10^{-5} cps and 2.24×10^{-4} cps, respectively). Munk et al. (1970) estimated the phase speed (c) of the K_1 and M_2 tides as 214 m/s and 140 m/s. We calculated the alongshore wave number of each frequency as $k_y = \frac{\omega}{c}$. Based on the alongshore wave number k_y at each frequency, we calculated an estimated alongshore sea surface slope (η_y) forced by the tide as:

$$-g\eta_y \approx -ig[k_y(K_1) * \eta(K_1) + k_y(M_2) * \eta(M_2)] \tag{4.5}$$

where i indicates a $-\frac{\pi}{2}$ phase shift in time. The sea surface variability at the K_1 and M_2 frequencies was estimated from the pressure record at the 8m ADCP by harmonic analysis. The phase of the estimated barotropic alongshore gradient in sea level is discussed in some detail below.

4.3.2 Cross-shore momentum balances

In the cross-shore, we use a 2-layer model, where the ρ_1 and ρ_2 are the density of the upper and lower layer, respectively, and the interface between the layers is initially at $-H_1$.

The momentum balances for the upper and lower layer are:

Layer 1: upper layer

$$\frac{\partial u_1}{\partial t} + \left[u_1\frac{\partial u_1}{\partial x} + v_1\frac{\partial u_1}{\partial y} + w_1\frac{\partial u_1}{\partial z}\right] - fv_1 = -g\frac{\partial \eta}{\partial x} + \frac{\tau_s - \tau_i}{\rho_1(H_1+H_2)} \tag{4.6}$$

Layer 2: lower layer

$$\frac{\partial u_2}{\partial t} + \left[u_2 \frac{\partial u_2}{\partial x} + v_2 \frac{\partial u_2}{\partial y} + w_2 \frac{\partial u_2}{\partial z} \right] - f v_2 = -g \frac{\partial \eta}{\partial x} - g \frac{\Delta\rho}{\rho_o} \frac{\partial \zeta}{\partial x} + \frac{\tau_i - \tau_b}{\rho_2 (H_2 - H_1)} \quad (4.7)$$

where u and v are the eastward (cross-shore) and northward (longshore) components of velocity, respectively ([m/s]). Subscripts refer to the upper (1) and lower (2) layers. η is sea level elevation ([m]) and ζ is the elevation of the interface between the layers (i.e. pycnocline elevation) calculated its from its undisturbed height ([m]), which we directly measured using WW profilers. $\Delta\rho$ is the density gradient across the interface. τ_s, τ_i and τ_b are the surface, interfacial and bottom stresses, respectively ([N/m^2]). ρ_o is a reference density ([kg/m^3]). H_1 and H_2 are the depth of the bottom of the upper and lower layer, respectively, and f is the Coriolis frequency ([s^{-1}]).

Integration of the cross-shore momentum equations

We integrate the cross-shore momentum equations vertically over each layer and horizontally between the moorings to obtain an expression for cross-shore momentum in each layer. We ignore the nonlinear terms (bracketed in equations (4.6) and (4.7)), which we assume to be small. This simplification is assessed later. Equation (4.6) becomes:

$$\frac{\partial u_1}{\partial t} - f v_1 = -g \eta_x + \frac{\tau_s - \tau_i}{\rho_o H_1} \quad (4.8)$$

where the subscript x represents the partial derivative in the x dimension. We integrate equation (4.8) vertically from the interface to the surface and from the offshore (0) to inshore (X_{in}) edge of the domain, in order to write (4.8) in terms of transport accelerations ([m^3 s^{-2}]).

$$\int_0^{X_{in}} \int_{-H_1}^{0} \left[\frac{\partial u_1}{\partial t} - f v_1 \right] dz\, dx = \int_0^{X_{in}} \int_{-H_1}^{0} \left[-g \eta_x + \frac{\tau_s - \tau_i}{\rho_o H_1} \right] dz\, dx \quad (4.9)$$

We can integrate equation (4.9) as

$$\frac{\partial}{\partial t} \mathbf{U}_1 - f \mathbf{V}_1 = -g \eta_x H_1 X_{in} \quad (4.10)$$

by writing the across and alongshore transports in the upper layer as $\mathbf{U}_1$ and $\mathbf{V}_1$, respectively, and assuming that the surface and interfacial stresses (τ_s, τ_i) are zero.

We do not have direct observations of sea level elevation with the precision capable of ascertaining the sea level gradient in the x-dimension over the length of the domain ($\sim$1.5 km). We must, therefore, develop an expression that relates the pressure gradient force to the velocity field. If we assert that the horizontal sea level gradient (η_x) is in instantaneous geostrophic balance with the barotropic alongshore velocity, we can write

$$-g\eta_x(t) = -f\frac{1}{N}\sum_{i=1}^{N} v(t,z) \tag{4.11}$$

where $\frac{1}{N}\sum_{i=1}^{N} v(t,z) = \bar{v}(t)$ is the mean alongshore velocity over the entire domain (e.g. H_2 to 0). Substituting equation (4.11) into equation (4.10), the simplified cross-shore momentum balance in layer 1 becomes:

$$\frac{\partial}{\partial t}\mathbf{U}_1 = -f\bar{v}H_1X_{in} + f\mathbf{V}_1 \tag{4.12}$$

2) Lower Layer:

A similar approach can be used for the lower layer. Equation (4.7) becomes (neglecting the nonlinear terms)

$$\frac{\partial u_2}{\partial t} - fv_2 = -g\eta_x - g\rho'\zeta_x + \frac{\tau_i - \tau_b}{\rho_o(H_2 - H_1)} \tag{4.13}$$

where ρ', reduced gravity, is $\frac{\Delta\rho}{\rho_o}$

We integrate equation (4.13) vertically and horizontally:

$$\int_0^{X_{in}}\int_{-H_2}^{-H_1}\left[\frac{\partial u_2}{\partial t} - fv_2\right]dz\,dx = \int_0^{X_{in}}\int_{-H_2}^{-H_1}\left[-g\eta_x - g\rho'\zeta_x + \frac{\tau_i - \tau_b}{\rho_o H_L}\right]dz\,dx \tag{4.14}$$

where $H_L = H_2 - H_1$ is the height of the lower layer. Following the substitutions outlined above, and the lower layer momentum equation becomes

$$\frac{\partial}{\partial t}\mathbf{U}_2 = f\mathbf{V}_2 - \left[(g\rho'\zeta_x + f\bar{v})H_L + \frac{\tau_b}{\rho_o}\right]X_{in} \tag{4.15}$$

where the lower layer transports are $\mathbf{U}_2$ and $\mathbf{V}_2$ and the balance of the variables are as above.

4.4 Field Experiment

4.4.1 ADCP array

The ISPX mooring array was designed to provide detailed cross-shore and vertical resolution of currents over the inner shelf (5 to 35 m; Figure 4.2). Five bottom-mounted ADCPs were deployed in 32, 22, 17, 12 and 7 m depths (below MLLW), and were configured for 15 s sampling at vertical resolutions ranging from 1 m (32 m and 22 m ADCPs) to 25 cm (12 and 6 m ADCPs). Currents were rotated to cross- and alongshore components according to local bathymetry (National Ocean Service Hydrographic Data Base). Rotations were all in the clockwise sense between 6° and 11° (6°, 32 m; 7°, 22 m; 11°, 17 m; 9°, 12 m; 6°, 7 m). The current data were decimated to hourly values and high-pass filter at the inertial frequency (1.08 cycles d^{-}1) to remove the contribution to the diurnal sea-breeze (Lerczak et al. 2001). Finally, the current data were interpolated (32 and 22 m ADCPs) or decimated (12 and 7 m ADCPs) to 0.5 m vertical bin size.

4.4.2 WireWalkers

The WW wave-powered autonomous profiler uses the surface wind-wave field to power vertical profiling (Rainville and Pinkel 2001). The WWs are a simple and robust tool to study evolving small-scale vertical distributions of physical variables. We deployed 2 WWs, at 22 and 12 m depths (sampling the upper 19.5 and 9 m, respectively). Each WW was equipped with a SBE Fastcat CTD, capable of 16 Hz measurements of temperature, salinity and pressure. Density was calculated from the equation of state. Density data were decimated to hourly values centered on the ADCP observations and

10 cm vertical resolution. Given battery limitations, the 3 week WW deployment included 2 scheduled turn-around periods, which resulted in pre-planned gaps in water column coverage. Profiling and data acquisition were unfortunately imperfect and major gaps therefore exist in the final time series.

4.5 Analysis methods

In order to assess the relative importance of the terms of the momentum balances above, we extracted coherent tidal variability from the alongshore and cross-shore velocity time series at each ADCP using an empirical orthogonal function (EOF) decomposition, and created reconstructed velocities (e.g. Rudnick and Davis 1988, Rudnick et al. 1993). EOF analysis decomposes the variability of a time series into a set of orthogonal functions which are constrained such that no other representation of the data can produce a lower mean-square error (Davis 1976). Time-domain EOF analysis decomposes variability into standing modes. In an internal tide wave field, we expect that the phase will be variable in time (Lerczak et al. 2003) and that the alongshore and cross velocity will be 90° out of phase vertically. We therefore used a complex-domain EOF decomposition to extract the coherent barotropic and baroclinic tidal variability across the array into a single mode.

The Hilbert transform EOF (HEOF) decomposition allows for the identification of propagating patterns across a spatial array (Wallace and Dickinson 1972, Horel 1984, Hannachi et al. 2007). The Hilbert transform approach has been used in meteorology and oceanography to investigate large scale phenomena like El Niño (Barnett 1983) and small scale phenoma such as coastal upwelling (e.g. Kundu et al. 1975). The Hilbert transform is functionally a filtering operation in which each spectral component of the time series is phase-shifted by $+\frac{\pi}{2}$, thus providing information about the relative phases between the elemental sinusoids which comprise the original variable. This is most easily seen in the case of a time series with only one frequency component, in which case the Hilbert transform is simply the time derivative of the original time series. Therefore, the Hilbert transform provides information about the local rate of change of a variable with respect to time, in a frequency-integrated sense (Barnett 1983, Horel 1984).

We constructed a complex representation of each velocity time series $U_j(t) = u_j(t) + i\hat{u}_j(t)$ and $V_j(t) = v_j(t) + i\hat{v}_j(t)$, where u and v were the cross and alongshore components of velocity, respectively, and $\hat{u}_j(t)$, $\hat{v}_j(t)$ was the Hilbert transform of the original time series $u_j(t)$ computed by discrete fast Fourier transform (FFT). We constructed a matrix of the Hilbert transformed velocity time series over all spatial locations (1 to J) and at all times 1 to T, such that $\mathbf{C} = [U_j(t), V_j(t)]$ is a complex matrix of dimensions T×2J. The phase of an HEOF transform is only defined to an additive constant (Horel 1984). In the case of the analysis that follows, all phases were relative to the cross-shore velocity at the bottom-most bin at the 32 m ADCP.

4.5.1 Hilbert transform EOF (HEOF) filtering

If $\mathbf{C}$ is a complex-valued T×2J matrix containing the Hilbert-transformed cross and alongshore velocities at each depth across the five ADCP array, we can reconstruct a T×2J complex matrix $\mathbf{R}$ out of the temporal mean at each spatial location ($\bar{\mathbf{U}}(\mathbf{x})$ where $\mathbf{x}_i, i = 1 \ldots 2 \times J$ and the overbar indicates a mean calculated over all T observations [m/s])) and the first K HEOF spatial modes ($\mathbf{h}_i, i = 1 \ldots \mathbf{K}$) and temporal amplitudes ($\alpha(t)_i, i = 1 \ldots \mathbf{K}, t = 1 \ldots \mathbf{T}$) by the relation (Rudnick and Davis 1988):

$$\mathbf{R} = \bar{\mathbf{U}}(\mathbf{x}) + \alpha_i \mathbf{h}_i^{\mathrm{T}} \tag{4.16}$$

where $\bar{\mathbf{U}}(\mathbf{x})$ is a T×2J matrix populated with the temporal mean $\bar{u}(x)$ at each spatial location along the columns. The units of the entries in this matrix are [m/s], while the EOF reconstruction is unitless–the resultant matrix $\mathbf{R}$ also has units [m/s]. Note that this reconstruction can be performed over any number of $\leq$ 2×J modes, where the full reconstruction (i.e. using all 2×J modes) is exactly equal to the original data matrix $\mathbf{C}$. The choice of which modes to use involves an arbitrary decision, typically facilitated by expected behavior of the process being investigated. In the case of the present study, the first HEOF mode accounted for 44.5 % of the variability in the along- and cross-shore velocity time series and was dominated by semidiurnal variability (Figure 4.3), so we limited our reconstruction to the real part of mean and first HEOF (Horel 1984):

$$\mathbf{R_{tidal}} = \mathbf{Re}\left[\bar{\mathbf{U}}(\mathbf{x}) + \alpha_1 \mathbf{h}_1^{\mathrm{T}}\right] \tag{4.17}$$

4.5.2 Assessing the terms of the momentum equation

The experimental domain was comprised of the innermost portion of the continental shelf, between depths of 18 and 7 m, encompassing three ADCPs (Figure 4.2d). The domain range and the depth of the layers were based on the HEOF reconstruction: over the course of the experiment, the surface and bottom layers were counter-rotating at those three moorings (Figure 4.7). The upper and lower layers were chosen as those ADCP bins at each mooring that were rotating counter-clockwise and clockwise respectively.

We estimated the vertical and horizontal integrals in equations (4.9), (4.14) and (4.3) as the Riemann sum of the velocity measurements, e.g.:

$$\sum_{j=1}^{3}\sum_{i=1}^{N_1} u_1(z,x)\,\Delta z, \Delta x, \tag{4.18}$$

where the inner summation was over all the ADCP bins in the layer and Δz was the bin size (in meters). The outer summation was across the three ADCPs in the domain and Δx is the separation between the instruments (in meters). The vertical resolution of the ADCPs was such that the Riemann sum was a reasonable approach to estimate the continuous vertical integral. The cross-shore separation between adjacent ADCP moorings was $\sim$500 m. The separation between the moorings was small relative to the wavelength of the internal tide ($\sim$20 km, Lerczak 2000), and therefore seemed likely to provide adequate horizontal resolution to study tidal processes. The integration scheme, while imperfect, had the virtue of being the simplest possible approach and avoided potential complications due to interpolation or projections.

Bottom friction was estimated from the quadratic drag law:

$$\tau_{b(x)} = \rho C_D * u_b * \sqrt{u_b^2 + v_b^2} \tag{4.19}$$

$$\tau_{b(y)} = \rho C_D * v_b * \sqrt{u_b^2 + v_b^2} \tag{4.20}$$

where C_D is a drag coefficient taken to be 3.0 x 10^{-3} (e.g. Geyer et al. 2000). The u_b and v_b velocities were taken as the cross-shore and alongshore velocity 2 m above the bottom at each time (Geyer et al. 2000). The choice of drag coefficient was somewhat arbitrary. We had no direct measurements of bottom stress or bottom roughness, so we have chosen a canonical value for C_D based on literature values (e.g. Geyer et al. 2000). Bottom friction was a critical component of this analysis, and a range of values of C_D and formulations of the drag were tested to assess the impact on the analysis of tidal variability.

In what follows, we describe the results of the HEOF decomposition and the sense of rotation of the reconstructed velocities. Subsequently, we compare measurements of the temporal derivatives of cross-shore and alongshore transport from the HEOF reconstruction with dynamical estimates of those equations based on equations (4.12), (4.15), and (4.4).

4.6 Results

4.6.1 The structure of coherent current variability

The variability in the raw cross-shore (u) and alongshore (v) velocities was primarily tidal and the u and v velocities were similar in magnitude, reaching a maximum of $\sim$15 cm s^{-1} (Figure 4.4 and 4.5). The variability was qualitatively coherent across the inner shelf for both components of velocity. The magnitude of the currents decreased as the water column depth decreased. The cross-shore velocity was surface and bottom intensified and the alongshore velocity was surface intensified (Figure 4.4 and 4.5).

The WW time series of density at 22 and 12 m were also dominated by semidiurnal variability due to the internal tide, and appeared to be coherent between the two moorings. Mid-water column isopycnal displacement averaged 8.5 m at the 22 m WW over the course of the experiment (Figure 4.6). Maximum mid-water column isopycnal displacement exceeded 12 m between 10-Aug and 14-Aug. Mid-water column isopycnal displacement at the 12 m averaged 5.5 m at the 12 m, and was approximately the depth of the water column between 10-Aug and 14-Aug. The pycnocline was variable in intensity and mean position over the course of the experiment at both moorings. Mean

density increased with time as the difference between surface and bottom density decreased (Figure 4.6).

4.6.2 Hilbert transform EOF analysis

The first mode of the HEOF transform accounted for 44.5% of the total variability in the cross and alongshore velocity time series over the length of the record ($\sim$ 20 d). The second mode accounted for 14% and the remainder of the modes accounted for $< 4\%$ of the variability each. The first HEOF mode accounted for 15% more variability than a time domain EOF of the cross- and alongshore velocity time series (not shown).

The structure of the first HEOF mode was consistent with previous analyses of internal tide currents over the SSCB shelf (Lerczak et al. 2003). The structure of u was surface and bottom intensified, with a minimum magnitude at the mid water column at all moorings (Figure 4.3). The surface and bottom were $\sim 180^\circ$ out of phase, with a relatively rapid transition at the mid-water column magnitude minimum and approximately constant phase in the surface and bottom layers. The structure of v was surface intensified at all moorings. The phase of v was more variable across the array than u. At the 32 and 22 m ADCP, v was 90° out of phase from surface to bottom. Inshore of 22 m, the phase shift between the surface and bottom decreased at each mooring. At the innermost mooring, the surface to bottom phase difference was $<45^\circ$ (Figure 4.3).

The near bottom bins (< 4 m above bottom) were characterized by decreasing amplitudes in both the cross-shore and alongshore components of velocities. This near-bottom decrease in the semidiurnal currents indicates the importance of frictional processes in the bottom boundary layer.

The first HEOF amplitude was characterized by semidiurnal variability, apparent in the phase of the temporal amplitude, which regularly progressed over a 2π range every semidiurnal period (Figure 4.3). The magnitude of the first HEOF amplitude was variable in time, peaking during the period between 10-Aug and 14-Aug, consistent with the WW isopycnal displacement data (Figure 4.6 and Figure 4.3).

4.6.3 Reconstructed time series of u and v velocities

The reconstructed u (u_{rc}) and v (v_{rc}) time series captured the semidiurnal variability in the raw time series. The reconstructed components of velocity were combined to assess the relative sense of rotation and ellipticity of the velocity vectors driven by the internal tide (Figure 4.7). At the 32 m ADCP, the near bottom currents were clockwise (CW) polarized and dominated by the cross-shore component. At the mid-column minimum in u_{rc} and v_{rc} the currents were counterclockwise (CCW) polarized. At the surface, the reconstructed velocity was CW polarized, and the magnitude of the u_{rc} and v_{rc} velocities were similar (Figure 4.7). Inshore of the 17 m ADCP, the reconstructed surface and bottom velocities were counter-rotating, CW polarized at the bottom and CCW polarized at the surface. The time mean temporal derivative of the reconstructed phase is a measure of the average rate of rotation, and was semidiurnal ($\frac{2\pi}{M_2}$ radians s^{-1} Figure 4.7).

The presence of counter-rotating surface and bottom velocities suggested that the semidiurnal variability over the inner portion of the array was not forced by a propagating or standing mode-1 internal wave. We used the transition between CW and CCW rotation to define the upper and lower layers in the analysis of the cross-shore momentum balances that follows, and restricted this analysis to the 17, 12 and 7 m ADCPs where the sense of rotation effectively ruled out simple mode-1 internal wave forcing.

4.6.4 Alongshore momentum balance

The terms of the alongshore momentum balance were estimated for a single layer according to equations (4.4) and (4.5). The vertically integrated estimate of barotropic alongshore sea level gradient ($-g\gamma_y$) ranged between -0.02 and 0.02 $m^3\ s^{-2}$, which was similar to the estimates of $f\mathbf{U}$ and the alongshore component of bottom stress ($\tau_{b(y)}$) (Figure 4.8). The phase of the M_2 component of sea level elevation calculated from pressure measured at the 8 m ADCP was adjusted to minimize the magnitude and tidal variability in the residual between $\mathbf{V}_t$ and the prediction of $\mathbf{V}_t$ based on equation (4.4). The best fit between the prediction and $\mathbf{V}_t$, as measured by a simple linear correlation, required a phase shift of 40°. The adjusted prediction and $\mathbf{V}_t$ showed good agreement

in phase and magnitude and were strongly linearly correlated ($r^2 = 0.59$, $p < 1 \times 10^{-5}$). The resulting residuals were only weakly correlated with $\mathbf{V}_t$, although they remained similar in magnitude to $\mathbf{V}_t$.

4.6.5 Cross-shore momentum balances

In the upper layer (layer 1), the temporal derivative of the cross-shore transport ($\mathbf{U}_t$) was strongly correlated with the prediction provided by the right hand side (R.H.S) of equation (4.12) ($\mathbf{U}_{t(pred)}$, $r^2 = 0.84$, $p < 1 \times 10^{-5}$). The magnitude of $\mathbf{U}_{t(pred)}$was smaller than $\mathbf{U}_t$, which led to residuals ($r = \mathbf{U}_t - \mathbf{U}_{t(pred)}$) that were correlated with $\mathbf{U}_t$ (Figure 4.9).

In the lower layer (layer 2), the alongshore transport term ($f\mathbf{V_2}$) was smaller in magnitude to the estimated integrated cross-shore sea level gradient$-g\eta_x = -f\bar{v}X_{in}H_2$) (Figure 4.10). The integrated bottom stress term ($\tau_{b(x)}$) was similar in magnitude to the alongshore transport and cross-shore gradient in sea-level terms. The estimated integrated cross-shore interfacial gradient term ($-g\eta_{int}X_{in}H_2$) was also similar in magnitude to the other forcing terms, although the phase and magnitude of $-g\eta_{int}$ was more variable in time than the terms calculated from the reconstructed velocities. The temporal derivative of the cross-shore transport ($\mathbf{U}_t$) was correlated with the prediction provided by the R.H.S of equation (4.15) ($\mathbf{U}_{t(pred)}$, r^2=0.19, $p < 1 \times 10^{-3}$), calculated without the $-g\eta_{int}X_{in}H_2$ term given the gaps in WW coverage. The $\mathbf{U}_{t(pred)}$, calculated without $-g\eta_{int}X_{in}H_2$, was smaller than the observed values of $\mathbf{U}_t$. Including $-g\eta_{int}X_{in}H_2$ increased the magnitude of $\mathbf{U}_{t(pred)}$. However, the phase of the$\mathbf{U}_{t(pred)}$ lagged the phase of the observed $\mathbf{U}_t$, as estimated by correlation coefficients calculated over a range of lags (best $r^2 = 0.60$, $p < 1 \times 10^{-5}$ at an optimal lag of $\frac{\pi}{6.2}$ M_2 periods). This lag resulted in large residuals that were correlated with $\mathbf{U}_t$ (Figure 4.10). The residuals between the phase adjusted prediction and the lower layer $\mathbf{U}_t$ is shown in bottom panel of Figure 4.10. The residuals are smaller with the optimal lag, although the $\mathbf{U}_{t(pred)}$ is still imperfect and the residuals were relatively large (>0.05 $m^3\ s^{-2}$) and correlated with $\mathbf{U}_t$.

4.7 Discussion

The interpretation of semidiurnal baroclinic variability as a propagating low-mode internal wave is supported by open ocean observations and models. Those observations include tracking the propagation of baroclinic tides from mid ocean archipelagoes such as the Hawaiian Islands (Rudnick et al. 2003, Rainville and Pinkel 2006a, Rainville and Pinkel 2006b), and observations over continental shelves in the northeast Atlantic Ocean (Pingree et al. 1986, Sherwin 1988, Sharples et al. 2007) and in the southwest Pacific (Sharples et al. 2001). Although there is no direct evidence of offshore generation of the baroclinic tide in the SCB, semidiurnal baroclinic variability in continental shelf currents and temperature is universally believed to be associated with remote generation and propagation through a variable coastal ocean (Winant 1974, Lerczak 2000, Lerczak et al. 2003, Boehm et al. 2005). The disagreements between theory and observation (e.g. Lerczak et al. 2003) have been attributed to the difficult-to-observe degrees of freedom in the ocean: temporal and spatial variability in stratification and subtidal currents on all scales, as well as the important nonlinear and nonhydrostatic processes acting in shallow water.

4.7.1 The rotation of semidiurnal baroclinic currents

The HEOF decomposition of the u and v velocities conclusively demonstrated that much ($>$40%) of the total variability in both components of shelf currents was due to coherent semidiurnal variability. The spatial structure of this coherent variability was consistent with previous characterizations of the internal tide over the SSCB, and was therefore likely to represent the internal tide. The advantage of the HEOF approach was that it allowed for propagating modes, which provides a more concise representation of the baroclinic variability than a time-domina EOF analysis. It also allows for the possibility of counter rotating variability in a single mode, something time domain and vector ($u+iv$) EOFs do not.

The reconstructed velocity time series demonstrate that the surface and bottom baroclinic variability was in fact counter-rotating in the shallow water of the inner-shelf (Figure 4.7), and that there was apparently a transition between CW-polarized and

counter-rotating modes around the depth of the pycnocline. This transition was driven by the change in relative phase of the near-surface v velocity across the shelf. The vertically counter-rotating nature of the baroclinic currents over the inner shelf dictates that something other than simple, inviscid mode-1 dynamics is driving shallow water baroclinic variability in the SSCB.

4.7.2 Semidiurnal baroclinic variability over the inner shelf

In narrow estuaries where the seaward end is subject to forcing by the barotropic tide, a lateral flow develops that is baroclinic and approximately 20% of the magnitude of the axial (and barotropically driven) flow. The slowing of barotropic flow in the bottom boundary layer due to friction causes a reduction in the Coriolis force and a lateral Ekman transport (Winant 2007). The combined flow field, when viewed at a point where friction is important (i.e. in shallow water), is much like the observations presented above: a vertically sheared axial (alongshore) velocity and a reversing lateral (cross-shore) flow, where the current vectors reverse polarization with depth (Martin et al. 2005, Winant 2007, unpubl.). The inclusion of stratification complicates the situation: free waves are formed which can propagate in any direction and the baroclinic structure of the flow field becomes more complex (Winant, unpubl.).

The simple, single-layer alongshore momentum balance does well in predicting the acceleration of the alongshore transport. The primary uncertainty in this analysis is the estimate of the alongshore sea surface gradient $-g\eta_y$, which is based on rather simple assumptions about the nature the barotropic tide. The phase of the K_1 and M_2 tidal constituents from the 8 m ADCP was adjusted to minimize the residual between the predicted and observed transport acceleration, which, given the uncertainty in the estimate of $-g\eta_y$, seemed to be a reasonable approach. It can be argued, however, that this simply forces the sea level gradient to behave as we require it, and does not provide strong proof of the barotropic tide driving the along shore transport.

It was somewhat surprising that $f\mathbf{U}$ was a significant term in the alongshore momentum balance. Our ADCPs lacked near-surface resolution, which may account for the non-zero vertically integrated cross-shore transport. Presuming that the non zero-transport was real, the large contribution of the $f\mathbf{U}$ term implies that both the barotropic

(tidal) and baroclinic (local) components of $-g\eta_y$ are important in driving the alongshore velocity.

The observed behavior of $\mathbf{U}_t$ in both the surface and bottom layers was in general well modeled by the simplified cross-shore momentum balances derived above. Much of the variability in $\mathbf{U}_t$ in each layer was due to the imbalance between the estimated sea level gradient ($f\bar{v}X_{in}H$) and the rotationally modified alongshore transport of each layer ($f\mathbf{V}$). This is imbalance results from the sheared alongshore flow which has depth-dependent rotational modification, and the depth-independant forcing by the cross-shore sea-level gradient. Frictional effects were important in the bottom layer, particularly in controlling the phase of $\mathbf{U}_{t(pred)}$. The observations of the stress due to the interfacial elevation were unfortunately incompletely sampled, which precluded isolating the coherent semidiurnal variability in that stress by an HEOF decomposition. The raw data were noisy, and the water column was rather more uniformly stratified than separated in two layers, as assumed in the theoretical treatment. Nevertheless, $-g\eta_i$ appeared to contribute by augmenting the acceleration of the cross-shore transport.

The significant deviations in magnitude (upper and lower layer) and phase (lower layer) between the simplified cross-shore momemtum balances and observations may be explained by comparison to the analytical solutions proposed by Winant (2007). In the upper layer, the terms in equation (4.12) predicted the phase of $\mathbf{U}_t$ well, but not the magnitude, which was underestimated by approximately 80%. This under-estimation is due to the fact that, unlike the case considered in Winant (2007) where the lateral flow was only 20% of the axial flow, the relative magnitudes of the cross and alongshore reconstructed velocities were similar. Therefore, there must be a forcing term not considered here contributing to the cross-shore transport. One potentially important term neglected in the analysis above is the role of surface and interfacial stresses in the upper layer momentum balance. In addition, lower frequency forcing (such as near inertial waves forced by the local sea breeze) could potentially play a role in the flux of cross-shore momentum and materially alter the balances discussed here.

The phase offset between the predicted and observed lower layer $\mathbf{U}_t$ was driven primarily by the slowly varying phase of both u and v in both layers. That is, as opposed to the simplified case in which u is exactly in phase within each layer and exactly π

radians out of phase between the layers, the variability within the layers (as well as the lack of near surface velocity measurements) meant that $\mathbf{U}_1$ and $\mathbf{U}_2$ were not π radians out of phase. Requiring that the bottom velocity be exactly out of phase with the surface velocity yielded the same phase shift as calculated by the lagged correlation approach to minimize the lower layer residuals (Figure 4.10), which indicates that the layer separation approach used here is not entirely satisfactory.

4.7.3 The nonlinear contribution

Lacking alongshore moorings and greater cross-shore resolution, it is impossible to directly estimate the x- and y- partial derivatives of u and v and therefore the contribution of the nonlinear terms to the momentum balances. We expect, however, that those contributions may be large.

Using the domain defined in Figure 4.2, the horizontal, cross-shelf flux of alongshore momentum into the domain can be estimated as:

$$\sum_{i=1}^{N} uv\delta z \tag{4.21}$$

where N is the number of vertical bins and δz is the bin size, calculated at the 17 m ADCP. The flux out of the domain can be estimated in a similar fashion using the measurement at the 8 m ADCP. The alongshore momentum flux divergence:

$$\sum_{i=1}^{N} \left[uv\delta z\right]_a - \sum_{i=1}^{N} \left[uv\delta z\right]_b \tag{4.22}$$

where a and b are the left and right sides of the domain, respectively (Figure 4.2). Equation (4.22) is a measure of the nonlinear contribution to the alongshore momentum balance. The nonlinear flux of momentum decreases across the shelf. The contribution of the nonlinear terms to the alongshore momentum balance as estimated by equation (4.22) is significant (Figure 4.11). The nonlinear flux was modulated by the variability in the baroclinic tide and acted to increase the magnitude of $\mathbf{V}_{t(pred)}$. The frequency content of the nonlinear contribution is double the semidiurnal period, due to the relative phasing of the u and v velocity, and therefore reduced the correlation between $\mathbf{V}_t$ and

$\mathbf{V}_{t(pred)}$. Nevertheless, this simple analysis showed that the nonlinear contribution was of the same order of magnitude as the other forcing terms in the alongshore momentum balance, and that the baroclinic variability over the inner shelf is likely to have a large nonlinear component.

4.8 Conclusions

The counter-rotating surface and bottom velocities over the inner shelf preclude interpretation of the semidiurnal variability observed there as either a propagating or standing mode-1 internal wave. We assessed simplified cross and alongshore momentum balances to test whether the baroclinic variability observed over the inner shelf was in fact directly driven by the barotropic tide in a manner analogous to the tidal flow in narrow estuaries (Winant 2007),

The simplified momentum balances we have considered here support the hypothesis that the baroclinic variability over the shallow inner shelf is directly forced by the alongshore sea level gradient due to the barotropic tide, friction in the bottom boundary layer, and rotation. In slightly deeper water (20 m) the current rotation in the surface and bottom layers was in the sense predicted by simple linear internal wave theory. It appears probable that both propagation of a remotely generated internal tide and local forcing due to the barotropic tide, friction and rotation were responsible for the observed semidiurnal variability over the SCB continental shelf. Considerable uncertainty remains given the specific behavior of the estimated terms in the momentum balances, the relative magnitude of the cross and alongshore velocities, the phase relationships between terms, and finally the potential for a nonlinear contribution to the cross and alongshore momentum balances. Conclusive demonstration of the validity of direct barotropic forcing of the baroclinic tide hypothesis awaits future modeling and field efforts.

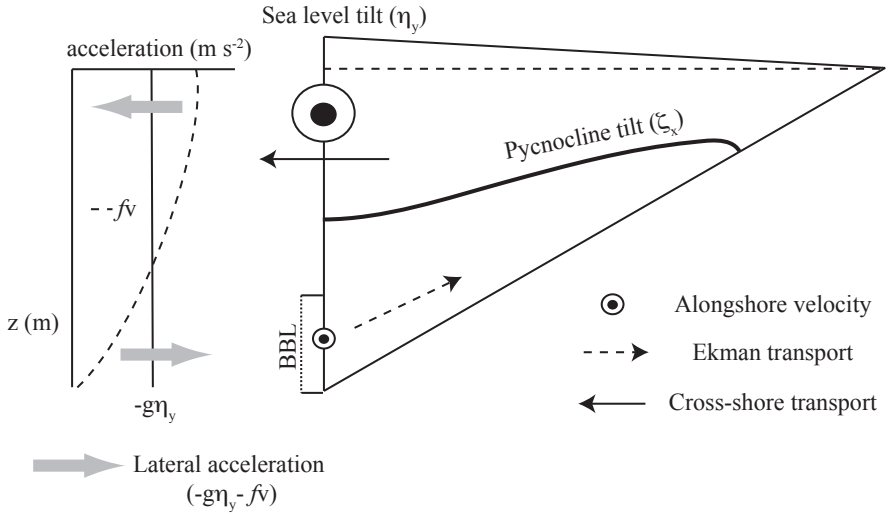

Figure 4.1: Schematic representation of the hypothesized forcing of semidiurnal variability over the inner shelf (following Martin et al. 2005, Winant 2007, 2008). Alongshore velocity (in this example, out of the page) is driven by the barotropic tide, and is vertically sheared due to friction in the bottom boundary layer (BBL). The sea level gradient is balanced by the Coriolis force acting on the mean alongshore velocity. In the lower layer, friction slows the alongshore velocity leading to an imbalance in Ekman forcing and an onshore Ekman transport in the lower layer. Assuming no alongshore variability, continuity requires that the onshore flow near the bottom is balanced by offshore flow in the upper layer. On the opposite phase of the tide, the pattern is reversed. One notable characteristic of this type of flow is that over a tidal cycle, the surface and bottom current vectors are counter-rotating on an *x*-*y* plane.

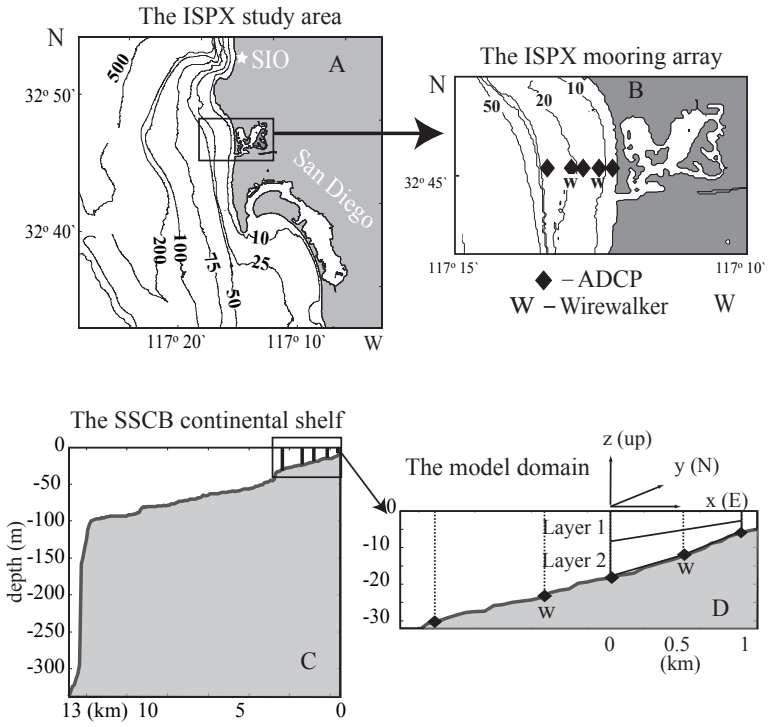

Figure 4.2: Map of the southern portion of the Southern California Bight and ISPX study area. The model domain is defined by the sense of rotation of the HEOF analysis (Figure 4.7) and is shown in panel d.

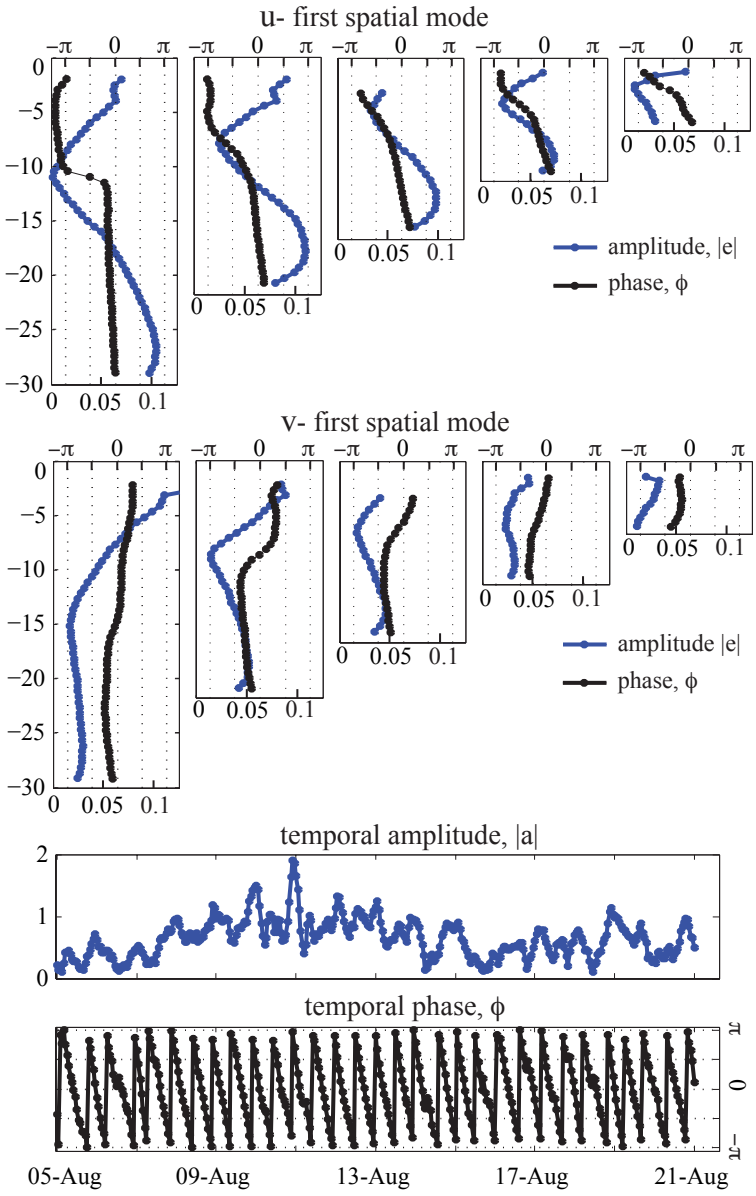

Figure 4.3: First mode of the HEOF decomposition of cross-shore and alongshore velocity across the shelf. The first mode accounted for 42% of the variability in the combined time series. The spatial structure (magnitude and phase) and temporal variability (amplitude and phase) reflected the semidiurnal baroclinic variability on the shelf. The structure and phase relationship were consistent with previous studies of the internal tide in the study area (Lerczak et al. 2003)

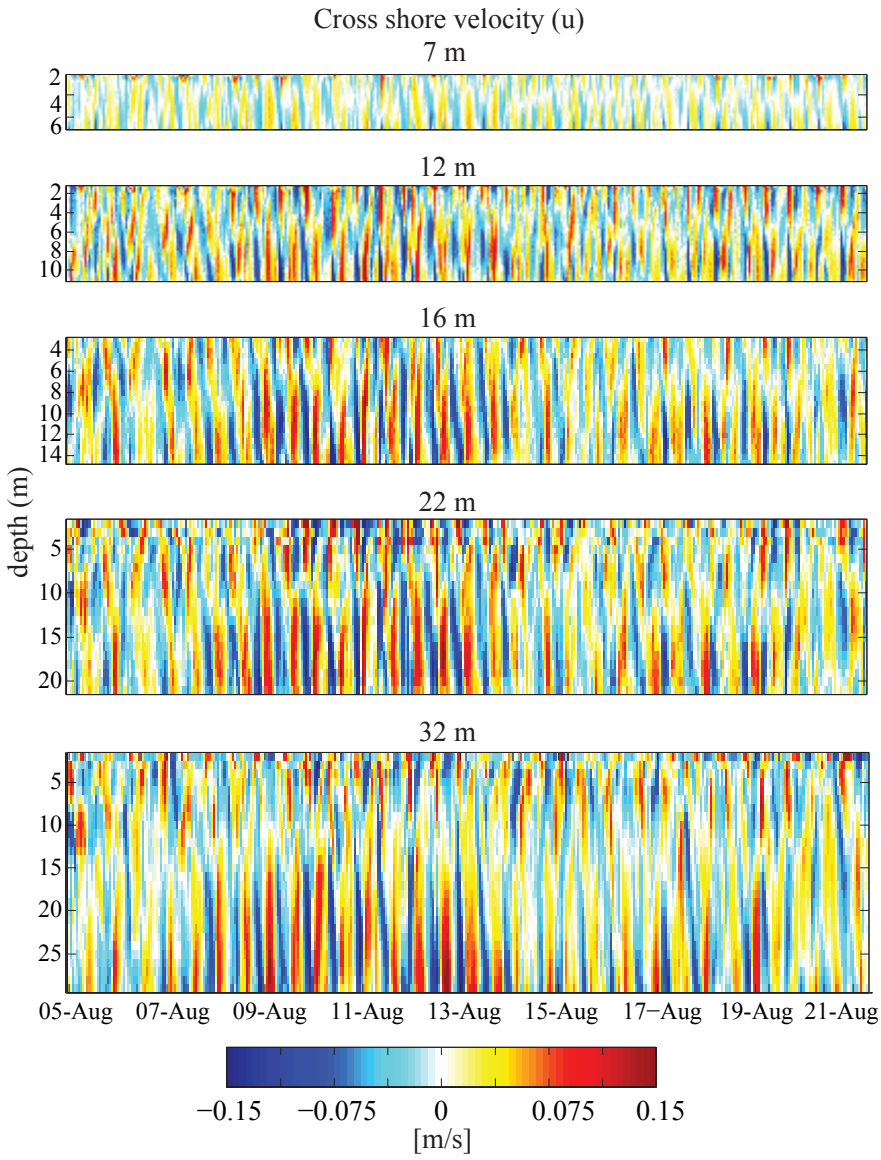

Figure 4.4: Cross-shore velocities at 5 locations over the SSCB inner shelf. Subinertial variability ($<$ 1.08 d) was removed by high pass filter to eliminate wind-driven variability in the upper $\sim$3 m at each current meter location.

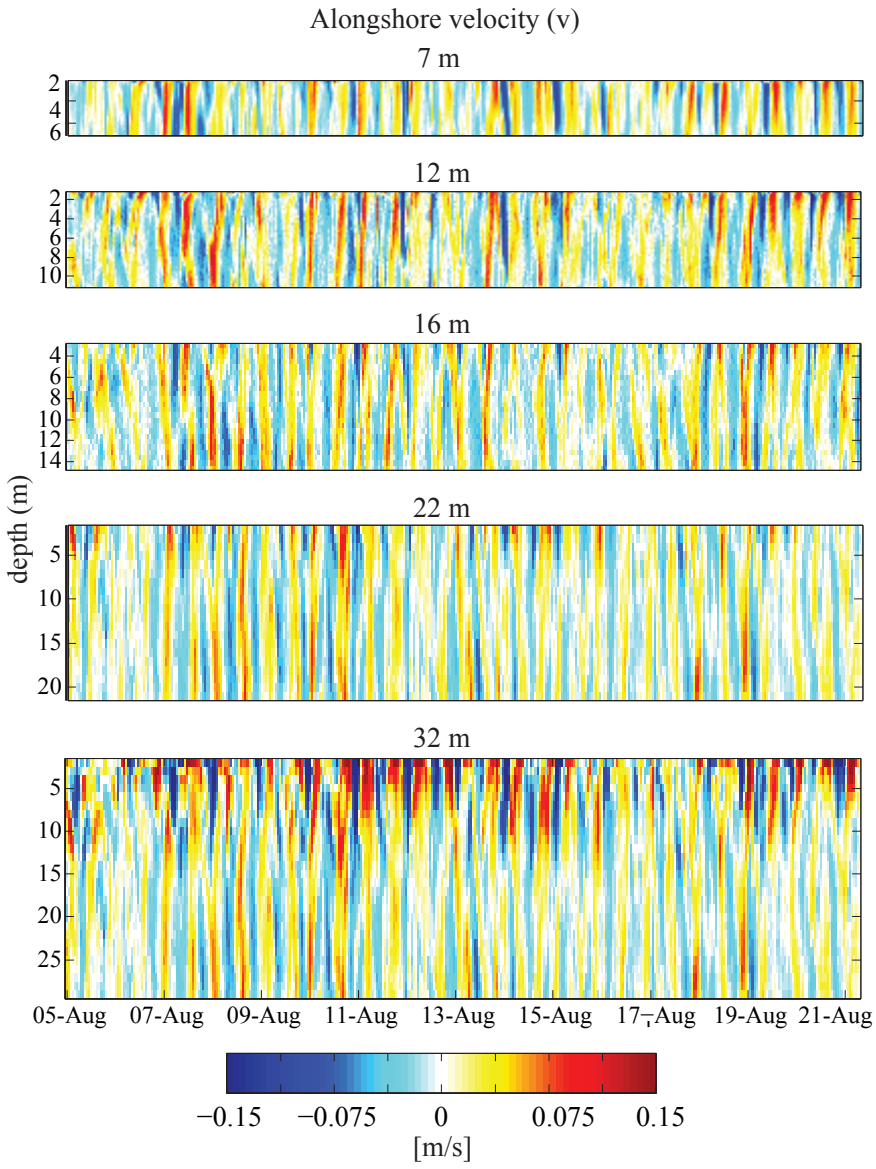

Figure 4.5: Alongshore velocities at 5 locations over the SSCB inner shelf. Subinertial variability ($<$ 1.08 d) was removed by high pass filter to eliminate wind-driven variability in the upper $\sim$3 m at each current meter location.

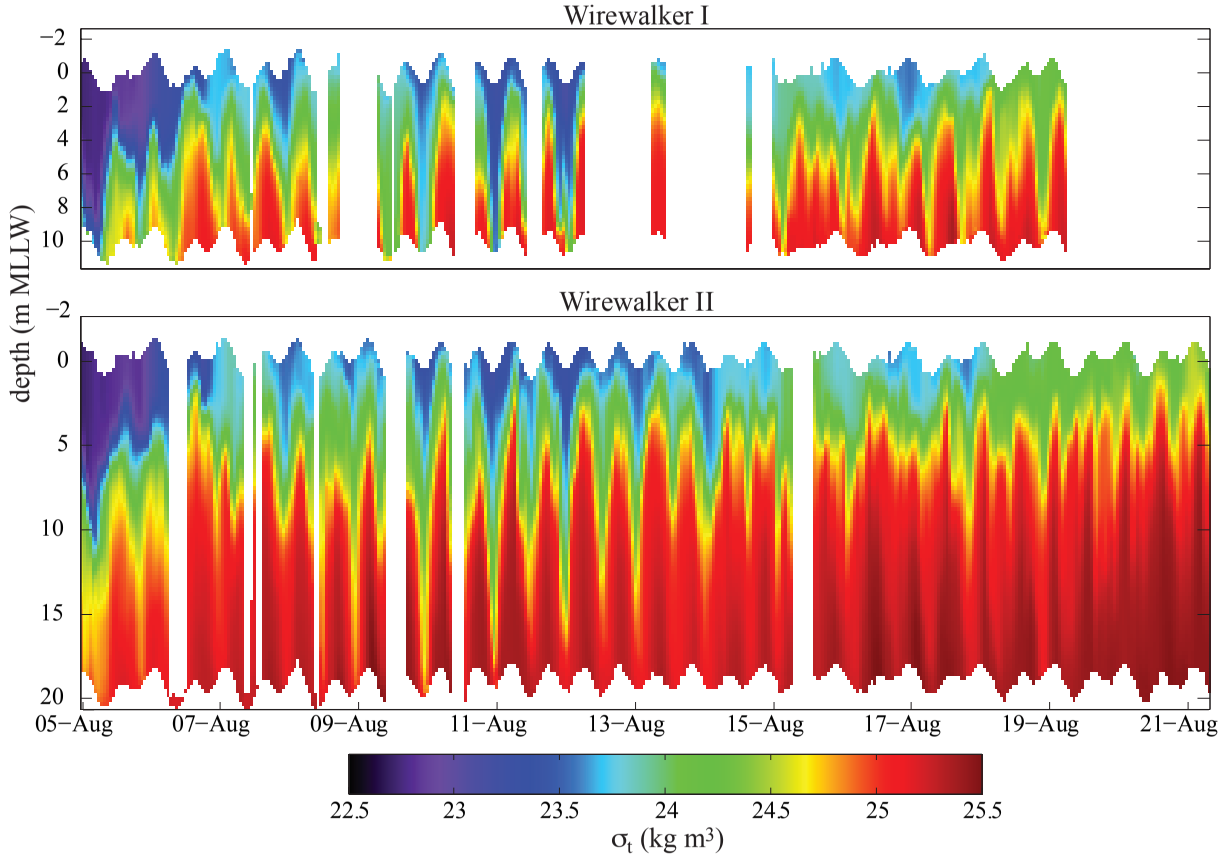

Figure 4.6: Density at two profiling moorings across the shelf. Gaps in the data were due to scheduled turn-arounds and unplanned interruptions. Vertical variability in density was dominated by semidiurnal baroclinic fluctuations. The intensity of fluctuations in the depth of the pycnocline was variable over the course of the experiment, peaking between 9-August and 14-August

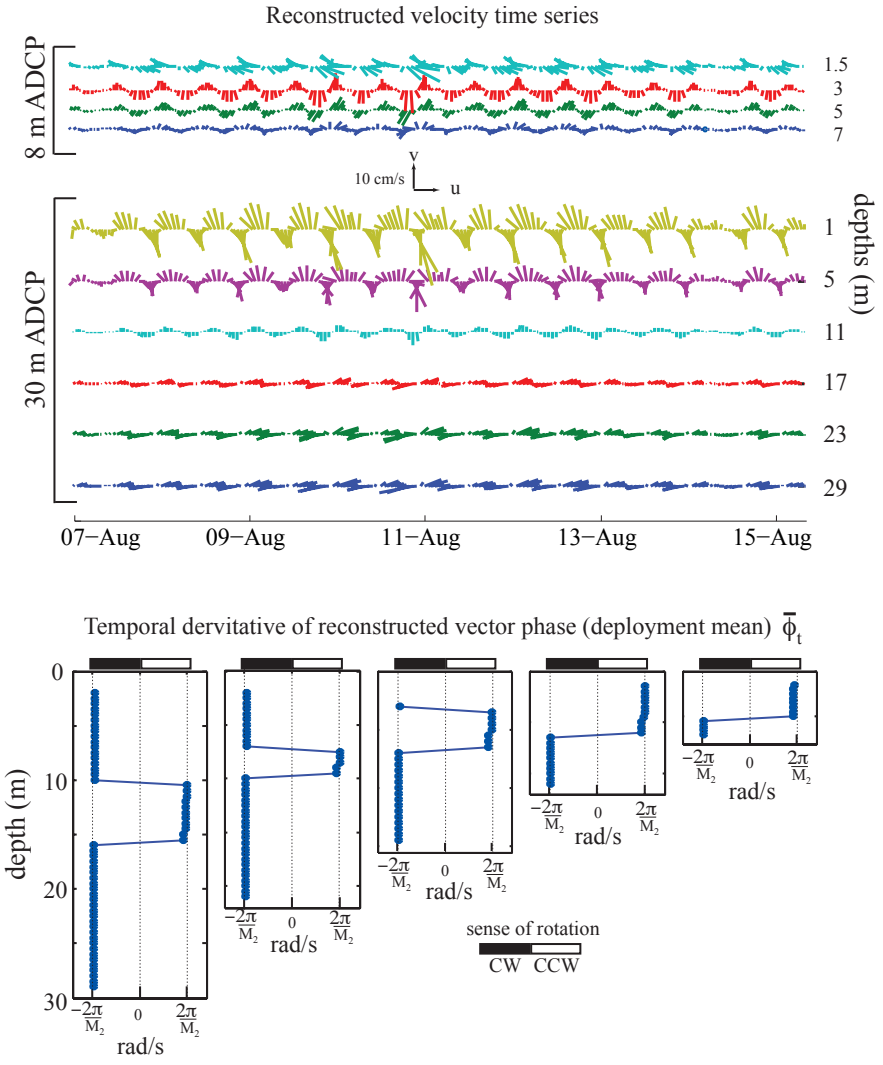

Figure 4.7: Sense of rotation of the reconstructed velocities. Reconstructed u and v velocities were assessed in vector form $u + iv$ to investigation the sense and rate of rotation. The outer 2 moorings were characterized by CW rotating modes in the surface and bottom layers. Inshore of $\sim 20m$ the surface velocities were CCW rotating. The rate of rotation, averaged over the length of the deployment (392 h), demonstrated the M_2 variability in the reconstructed velocities (i.e. one rotation (2π radians) per M_2 period (12.42 h)

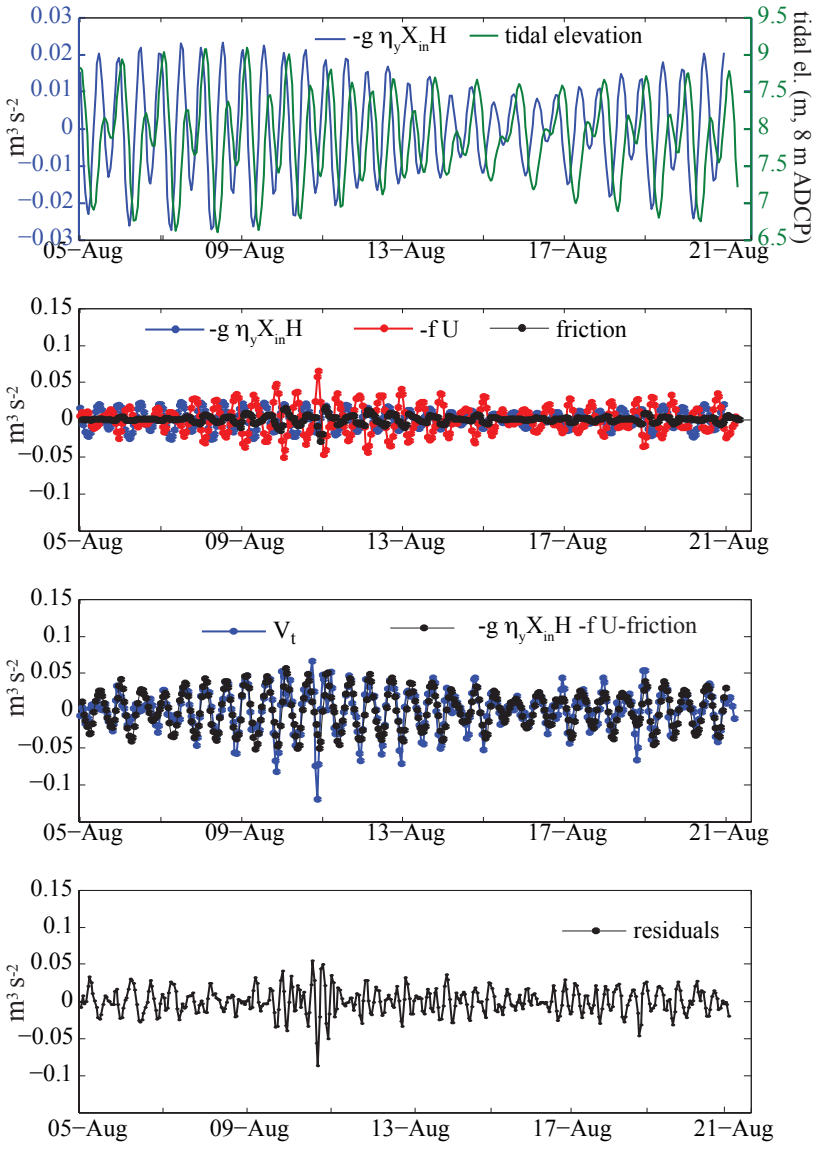

Figure 4.8: Alongshore momentum balance. The predicted $\mathbf{V}_{t(pred)}$, driven by the estimated alongshore gradient in sea surface slope, acceleration of the cross-shore transport, and friction, is strongly correlated with the observed $\mathbf{V}_t$. The structure of the residuals $(\mathbf{V}_t - \mathbf{V}_{t(pred)})$ was tidal, which indicated that some process variability was unaccounted for in this analysis.

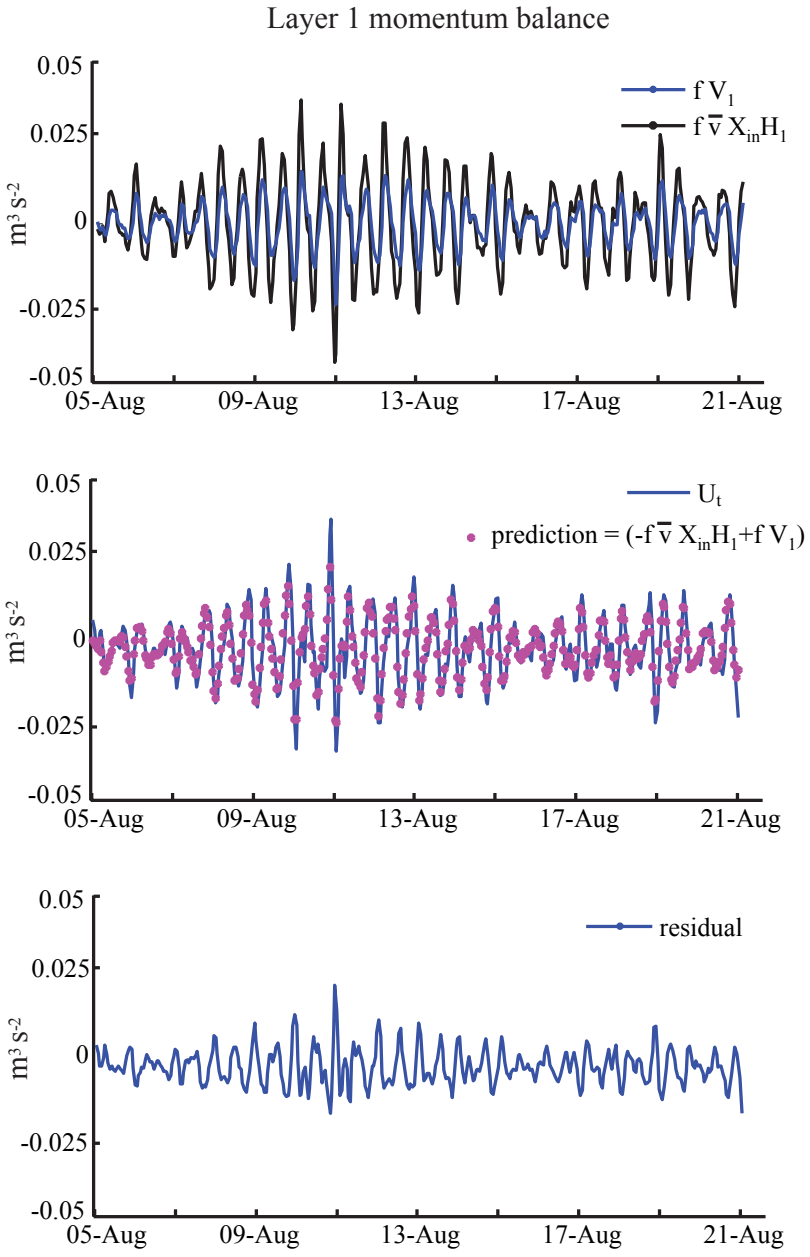

Figure 4.9: Cross-shore momentum balance, upper layer. The predicted $\mathbf{U}_{t(pred)}$, driven by the imbalance between the estimated cross-shore pressure gradient and the acceleration of the alongshore transport in the upper layer is strongly correlated but weaker than the observed $\mathbf{U}_t$. The structure of the residuals $(\mathbf{U}_t - \mathbf{U}_{t(pred)})$ was tidal, which indicated that some process variability was unaccounted for in this analysis.

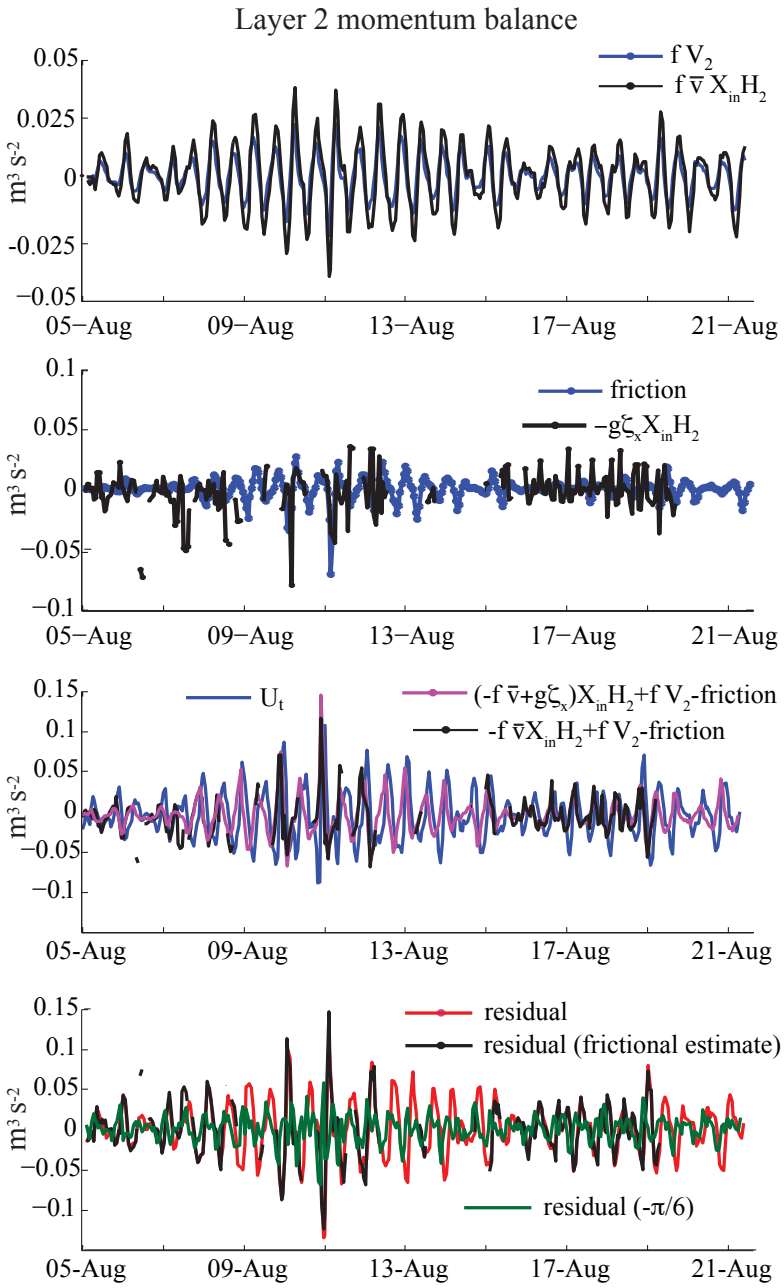

Figure 4.10: Cross-shore momentum balance, lower layer. The predicted $\mathbf{U}_{t(pred)}$, driven by the imbalance between the estimated cross-shore pressure gradient and the acceleration of the alongshore transport in the upper layer is correlated but weaker and slightly out phase with than the observed $\mathbf{U}_t$. The structure of the residuals ($\mathbf{U}_t - \mathbf{U}_{t(pred)}$) was tidal, which indicated that some process variability was unaccounted for in this analysis. In green in the final panel is the residual with an adjusted phase of $\frac{\pi}{6}$, as described in the text.

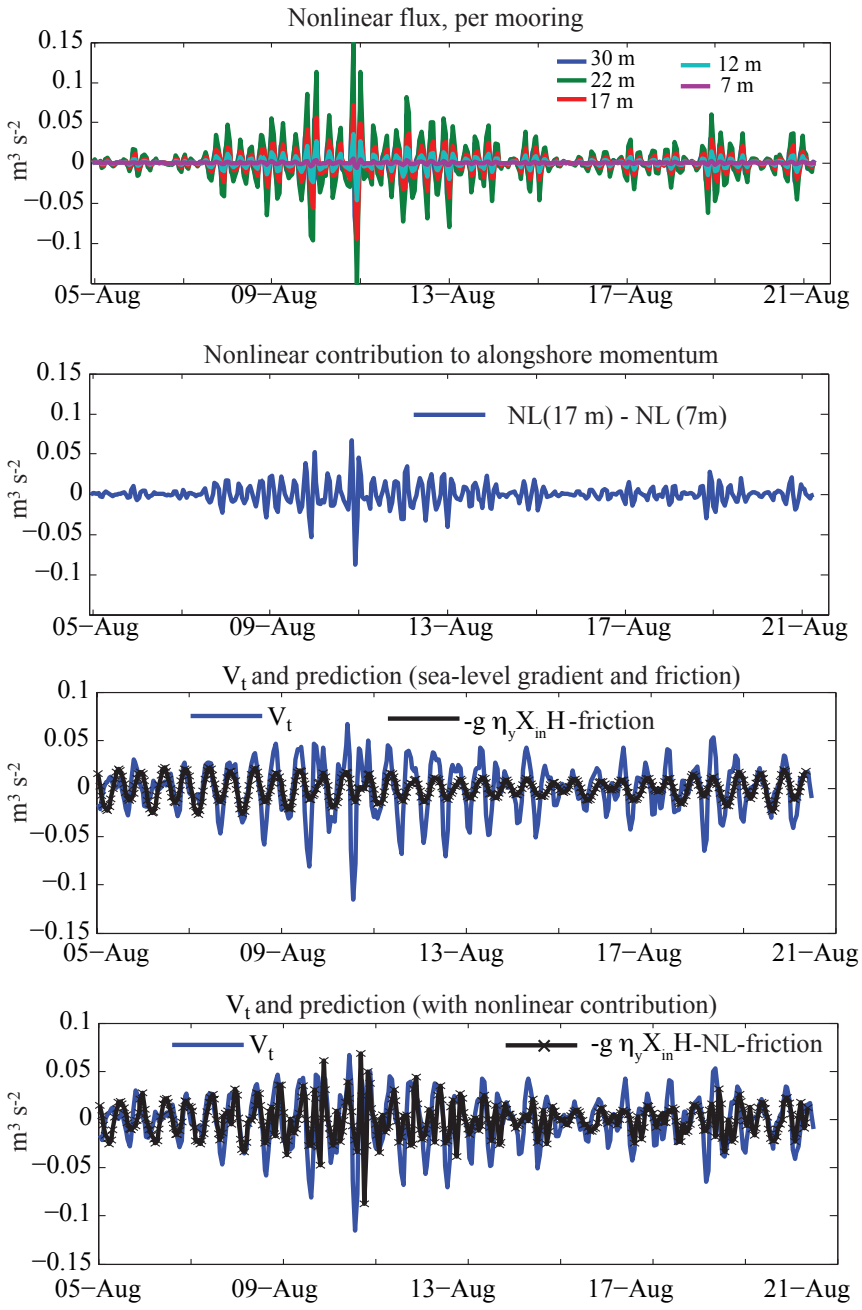

Figure 4.11: Nonlinear contribution to the alongshore momentum balance. The convergence of nonlinear momentum flux was as large as the other forcing terms in the momentum balance. $\mathbf{V}_{t(pred)}$, calculated with the nonlinear contribution was significantly less correlated to $\mathbf{V}_t$ than the prediction calculated without the NL terms, due to the $2M_2$ frequency content of the NL terms.

5 Concluding remarks and future challenges

5.1 Concluding remarks

The findings of ISPX confirm that variability in nitrate supply leaves a major imprint on the coastal phytoplankton community. The physical forcing in the SSCB is subtle; surface nitrate concentrations were always at or below detection in this study, as had been found in previous work (Eppley 1992). Nevertheless, significant fluxes of nitrate do occur, primarily through the delivery of nitrate-rich water through the base of the euphotic zone and vertical mixing at the nitracline. These fluxes are intensified over the inner shelf and are variable in time due to variability in: 1) the strength of the baroclinic tide (7-10 d timescale), 2) the local winds (2-5 d timescale), and 3) remote forcing (days to decades timescale). The schematic cartoon of the SCB shelf (Fig. 5.1) illustrates the interacting scales of variability and their impact of nitrate availability. It is probable that the ratio of new : total productivity is low over the SCB continental shelf (relative to Eppley and Peterson (1979), Fig. 2) precisely because of the interaction of the independent modes of variability in physical forcing. Large inputs of nitrate to the surface are very rare (e.g. wind-driven upwelling); however, along-isopycnal and diapycnal fluxes of nitrate through the base of the euphotic zone are constantly occurring—although variable in strength—with the exception of large, basin-scale warm anomalies such as El Niño.

This integrated mode of nitrate supply to the SCB shelf has several important ecological implications that may be shared by other shelf seas around the world. Twomey et al. (2007) referred to this background, subsurface nitrate flux at moderate

levels as ‘cryptic upwelling,’ and noted it fueled relatively high vertically integrated primary production without an obvious surface signature. In particular, the community nitrate uptake response in these systems appears to be different than the case of wind forced upwelling, where communities are observed to ‘shift up’ their nitrate uptake rates after large nitrate input to the euphotic zone (Dugdale and Wilkerson 1989, Smith et al. 1992, Kudela et al. 2000), and thus respond at a lag to nitrate injection. In the ’shift up’ model, the rate of increase of nitrate uptake is a linear function of the initial concentration of nitrate upon cessation of the upwelling event, while the instantaneous uptake rate is either uncorrelated or negatively correlated to the instantaneous nitrate concentration (Dugdale and Wilkerson 1989, Dugdale et al. 2000).

The ISPX nitrate uptake rates are positively correlated with in situ nitrate concentration (r^2 = 0.88, Fig. 5.2) and are therefore not consistent with the "shift up" model. This lack of a lag between nitrate availability rate and nitrate uptake rate, in contrast to communities that shift-up nitrate uptake, implies that the communities over the SSCB inner shelf are primed or quasi-permanently shifted up for nitrate uptake as it is episodically available, similar to the results of Twomey et al. (2007) over the Northwest Australian shelf and Lomas et al. (2009) in the Sargasso Sea. The rates of uptake of the major recycled sources of nitrogen are likewise positively correlated with each other (Fig 5.2), implying that, during periods with less nitrate flux, the communities are capable of maintaining high levels of primary productivity because they are utilizing a suite of organic nitrate sources (see Eppley et al. 1979, Azam 1986).

Diatoms are major players in the SSCB inner-shelf and, along with picoeukarotes, dominated the inner shelf phytoplankton community during ISPX. The nitrate uptake experiments suggest that these diatoms and picoeukarotes are capable of very rapid response to increased nitrate concentrations, as was borne out during the subsurface bloom at the 22 m WW, subsequent to an offshore shoaling of the nitracline (Chapter 3). Diatoms are considered to be primary contributors to export production, given their large size and rapid sinking rates (e.g. Michaels and Silver 1988, Boyd and Newton 1999, Bury et al. 2001). The contribution of diatoms to the coupled ocean/atmosphere carbon dioxide flux is therefore thought to be important (Falkowski and Barber 2003, Cermeño et al. 2008; however, see Richardson and Jackson 2007 for the importance of the pi-

coplankton fraction). The physical processes which control nitrate availability over the SSCB continental shelf modulate both the rate of carbon fixation and appear, at least in certain combinations, to favor taxa with the capacity for significant export carbon flux.

Over the last 40 years, SCB chlorophyll concentration has increased as the euphotic depth has decreased (Aksens and Ohman 2009). Over the last 20 years, total primary productivity in the SCB has increased as well (Kahru et al. 2009). Both of these results are surprising given the well-documented increase in SCB sea surface temperatures and stratification, which were expected to decrease nitrate availability in the euphotic zone (e.g. Roemmich and McGowan 1995). The dynamical explanation for these trends is not obvious, particularly considering coastal wind forcing in the SCB has apparently not changed much in the last 50 years (Rykaczewski and Checkley 2008).

The results of this dissertation shed some light on the seemingly paradoxical observations of increased stratification and increased productivity. Given that the cross shelf internal tide pump is presumably always on, and that the weak local winds typically induce a tilt in the nitracline, low-frequency changes to the depth of the nitracline at the shelf break would directly impact the euphotic zone biomass and primary productivity regardless of increased stratification (Fig. 5.2). In that sense, a weak, low-frequency increase in the amount of wind stress curl over the SCB, as observed by Rykaczewski and Checkley (2008), could cause large changes in the character of the SCB shelf euphotic zone in terms of productivity, community composition, biomass, and the capacity to export carbon. This effect is not due to the weak vertical velocities associated with the curl-induced Ekman pumping, but because the mean nitracline depth shoals as Ekman pumping increases. That nitrate could then be redistributed by the internal wave processes outlined above.

5.2 Future challenges

The ISPX study demonstrated that the detailed and complex interaction between coastal flow fields and phytoplankton ecology can be investigated on a small budget with limited logistic support. Ideally future investigations along these lines will benefit from dedicated sources of funding. Nevertheless, I believe it is clear that significant

advances in our understanding of the ocean can come from small projects such as ISPX. The novel results in this dissertation resulted from the implementation of relatively new technology in a multidisciplinary context, and serve as a reminder that even the ocean directly adjacent to one of the largest and oldest oceanographic institutions in the world still awaits significant discoveries.

5.2.1 Some open questions

The mechanisms of nitrate flux that support the patterns and intensity of biological productivity over the SSCB shelf are sensitive remotely forced variability which is at present poorly understood. Pringle and Riser (2003) suggest that variability in temperature over the shelf on weekly timescales is related to northward propagating coastally trapped waves forced by winds in Central Baja. These waves, if they do in fact impact the water column structure, would be expected to influence not only temperature but also the phytoplankton biomass, productivity, and community composition over the shelf. Other low-frequency forcing clearly impacts nitrate availability over the shelf. A monitoring strategy that estimates the low-frequency nitrate climate of the shelf in real time (Chapter 3) would allow for directed sampling effort to address these open questions.

The detailed nature of nitrate flux due to episodic, transient mixing events associated with breaking high frequency internal waves was not examined during ISPX. Nor was an explicit consideration of the role of the bottom boundary layer in the internal tide forced vertical redistribution nitrate attempted. The development of models which explicitly consider these nonlinear phenomena will advance our understanding of the coupling between the community level phytoplankton response to these episodic events.

Focusing exclusively on the importance of nitrate delivery, while justified by the patterns we observed, is a significant simplification. Perhaps most importantly, significant biological interactions among the phytoplankton themselves—and between the phytoplankton and zooplankton—will act to modulate both the composition of the phytoplankton community and the carbon export potential. Very little is known about the timescales of pelagic succession and predation in the context of variable physical conditions. Ecosystem models of shelf assemblages have demonstrated the importance of

pulsed nutrient delivery in the realized size structure of the phytoplankton and zooplankton. The SCB is an excellent laboratory to investigate episodic nutrient supply and the influence on biological interactions in a system that is less energetic and dispersive than vigorously forced upwelling systems.

In Chapter 4, I approached a long-standing assumption about the nature of semidiurnal baroclinic variability over the inner shelf from a new direction. The results of that analysis were necessarily tentative. While the shallow inner shelf appears to be subject to forcing that is not necessarily due to a low mode propagating internal wave, a number of uncertainties remain. Understanding the detailed dynamics of inner-shelf variability is not just interesting from a physical perspective, but has obvious biological importance given the results of Chapters 2 and 3.

Finally, the ultimate goal of coastal observing systems is to collect the appropriate types of data to predict the future state of the coastal ecosystem (e.g. www.sccoos.org). This goal requires a mechanistic understanding of the coastal ocean that does not yet exist. The fundamental dependence of the biological systems in the ocean on the extremely complex patterns of physical flow demand interdisciplinary approaches. Nevertheless, coupled biological and physical field programs need not necessarily be giant undertakings—significant advances can be achieved with limited resources.

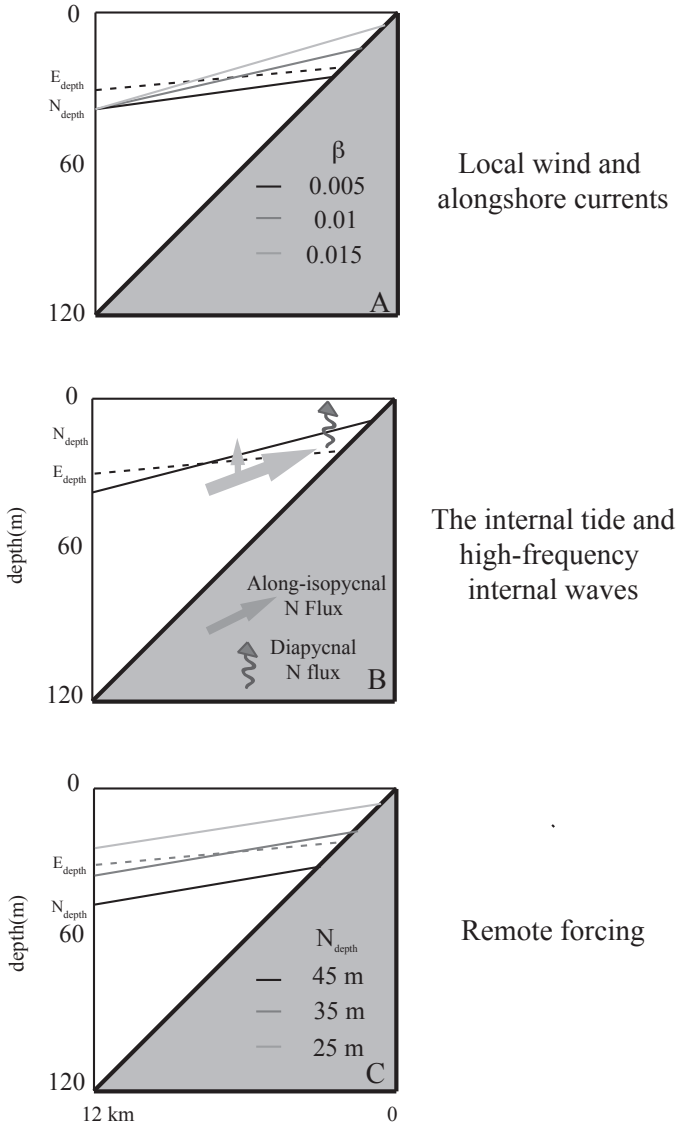

Figure 5.1: Schematic cartoon of the interacting physical mechanism responsible for control phytoplankton vital rates and community composition over the SCB continental shelf. The tidal 'pump' is variable but always on. Remote forcing controls the total availability of nitrate over the shelf and therefore impacts the tidal nitrate flux. Variability in local winds and alongshore current shear modulates the amount of nitrate in the shelf euphotic zone and controls the vertical component of the along-isopycnal tidal flux.

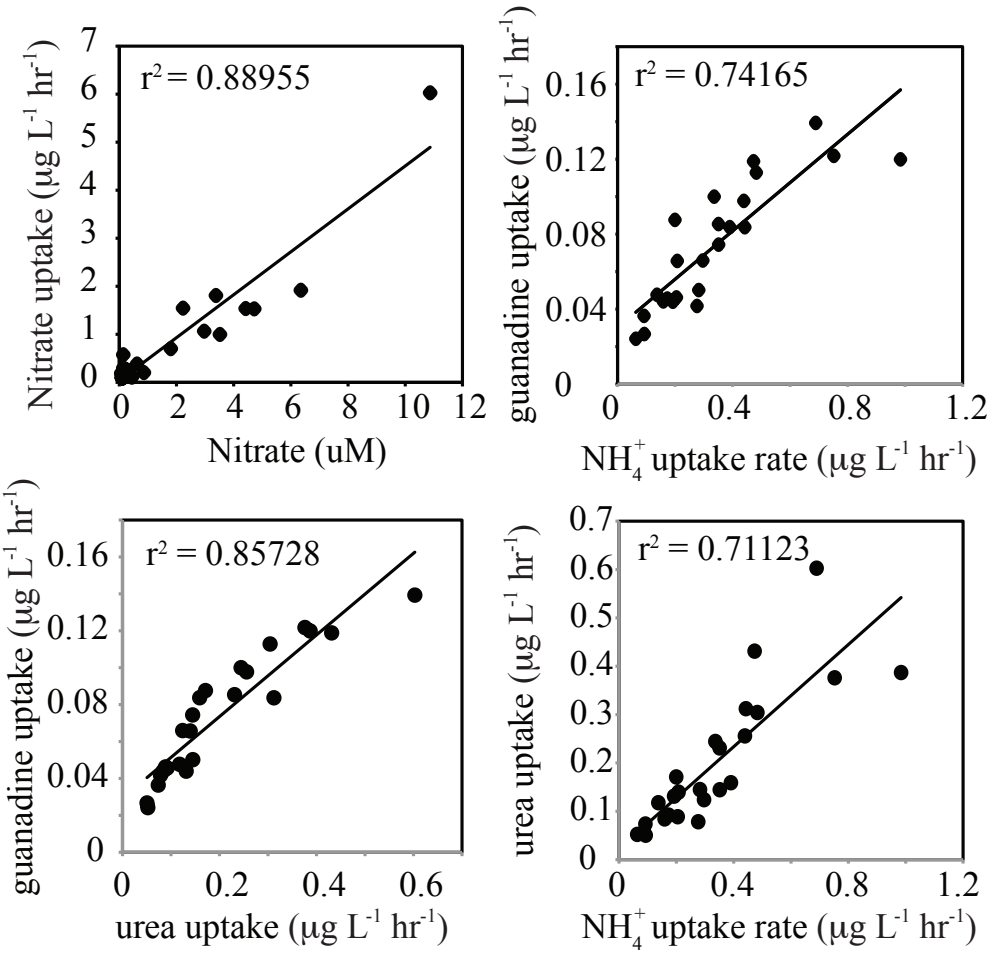

Figure 5.2: The relative uptake of nitrate and recycled nutrients. Panel a: nitrate uptake is well correlated with nitrate concentration, which is not typically observed in highly productive upwelling systems. One inference from this relationship is that the phytoplankton over the SSCB are being constantly supplied with variable levels of nitrate, leading to a quasi-permanent up-shifted state. Recycled production is paramount in the SSCB coastal environment– the uptake of all recycled nutrients that we surveyed were well correlated, indicating the the plankton rely heavily on each of these organic sources of nitrogen

References

[1] D.L. Aksens and M.D. Ohman. Multi-decadal shoaling of the euphotic zone in the southern sector of the california current system. *Limnol Oceanogr*, 54(4):1272–1281, May 2009.

[2] W.E. Allen. Occurrence of marine plankton diatoms in a ten-year series of daily catches in southern california. *Am J Bot*, 23(1):60–63, Jan 1936.

[3] F.A.J. Armstrong and E.C. Lafond. Chemical nutrient concentrations and thier relationship to internal waves and turbidity off southern california. *Jour. Phys. Ocean.*, 11(4):538–547, 1966.

[4] R. S. Arthur. Oscillations in sea temperature at scripps and oceanside piers. *Deep-sea Research*, 2(2):107–121, 1954.

[5] F. Azam. *Microbial recycling of nutrients in the Southern California Bight euphotic zone*, pages 216–286. Plankton dynamics in the Southern California Bight. Springer Verlag, 1986.

[6] W.M. Balch, B.C. Bowler, and C.F. Byrne. Sea surface temperature gradients, baroclinicity, and vegetation gradients in the sea. *Journal of Plankton Research*, 19(12):1829–1858, Jan 1997.

[7] R. T. Barber and F. P. Chavez. Regulation of primary productivity rate in the equatorial pacific, Dec 1991.

[8] T.P. Barnett. Interaction of the monsoon and pacific trade wind system at interannual time scales. *Monthly Weather Review*, 111:756–773, 1983.

[9] C.J. Bassin, L. Washburn, M. Brzezinski, and E. McPhee-Shaw. Sub-mesoscale eddies observed by high frequency radar: A new mechanism for delivering nutrients to kelp forest in the southern california bight. *Geophys. Res. Letters*, 32:L12604, 2005.

[10] M.J. Behrenfeld and P.G. Falkowski. Photosynthetic rates derived from satellite-based chlorophyll concentration. *Limnol Oceanogr*, 42(1):1–20, Jan 1997.

[11] M.J. Behrenfeld, R.T. O'Malley, D.A. Siegel, C.R. McClain, J.L Sarmiento, G.C. Feldman, A.J. Milligan, P.G. Falkowski, R.M. Letelier, and E.S. Boss. Climate-driven trends in contemporary ocean productivity. *Nature*, 444(7120):752–755, Jan 2006.

[12] A.B. Boehm, B.F. Sanders, and C.D. Winant. Cross-shelf transport at huntington beach: implications for the fate of sewage discharged through an ocean outfall. *Environ. Sci. Tech.*, 36:1899–1906, 2002.

[13] P.W. Boyd and P.P. Newton. Does planktonic community structure determine downward particulate organic carbon flux in different oceanic provinces? *Deep-Sea Res Pt I*, 46(1):63–91, Jan 1999.

[14] S.J. Bury, P.W. Boyd, T. Preston, G. Savidge, and N.J.P. Owens. Size-fractionated primary production and nitrogen uptake during a north atlantic phytoplankton bloom: implications for carbon export estimates. *Deep-Sea Res Pt I*, 48(3):689–720, Jan 2001.

[15] J. L. Cairns. Asymmetry of internal tidal waves in shallow coastal waters. *J Geophys Res*, 72(14):3563, 1967.

[16] P. Cermeno, S. Dutkiewicz, R.P. Harris, M. Follows, O. Schofield, and P.G. Falkowski. The role of nutricline depth in regulating the ocean carbon cycle. *P Natl Acad Sci Usa*, 105(51):20344–20349, Jan 2008.

[17] J.L. Collier and B. Palenik. Phycoerythrin-containing picoplankton in the southern california bight. *Deep-Sea Res Pt Ii*, 50(14-16):2405–2422, Jan 2003.

[18] L.H.N. Cooper. Internal waves and upwelling of oceanic water from mid-depths on to a continental shelf. *Nature*, 159(4043):579–580, Jan 1947.

[19] J.J. Cullen, E. Stewart, E. Renger, R.W. Eppley, and C.D. Winant. Vertical motion of the thermocline, nitracline and chlorophyll maximum layers in relation to currents on the southern-california shelf. *J Mar Res*, 41(2):239–262, Jan 1983.

[20] R.E. Davis. Predictability of sea surface temperature and sea level pressure anomalies over the north pacific ocean. *Jour. Phys. Ocean.*, 6(3):249–266, 1976.

[21] E. DiLorenzo, A.J. Miller, N. Schneider, and J.C. McWilliams. The warming of the california current system: Dynamics and ecosystem implications. *J Phys Oceanogr*, 35(3):336–362, Jan 2005.

[22] E. DiLorenzo, N. Schneider, K. M. Cobb, P. J. S. Franks, K Chhak, A. J Miller, J. C McWilliams, S. J Bograd, H Arango, E Curchitser, T. M Powell, and P Riviere. North pacific gyre oscillation links ocean climate and ecosystem change. *Geophys Res Lett*, 35(8):L08607, Jan 2008.

[23] R.C. Dugdale and J.J. Goering. Uptake of new and regenerated forms of nitrogen in primary productivity. *Limnol Oceanogr*, 12(2):196–&, Jan 1967.

[24] R.C. Dugdale and F.P. Wilkerson. The use of n-15 to measure nitrogen uptake in eutrophic oceans - experimental considerations. *Limnol Oceanogr*, 31(4):673–689, Jan 1986.

[25] R.C. Dugdale and F.P. Wilkerson. Silicate regulation of new production in the equatorial pacific upwelling. *Nature*, 391(6664):270–273, Jan 1998.

[26] D.H. Eccles. An internal wave in lake nyasa and its probable significance in the nutrient cycle. *Nature*, 194(4831):832, 1962.

[27] R.W. Eppley. Chlorophyll, photosynthesis and new production in the southern california bight. *Prog Oceanogr*, 30(1-4):117–150, Jan 1992.

[28] R.W. Eppley and O. Holm-Hanson. *Primary production in the Southern California Bight*, pages 176–215. Plankton dynamics in the Southern California Bight. Springer Verlag, 1986.

[29] R.W. Eppley and B.J. Peterson. Particulate organic-matter flux and planktonic new production in the deep ocean. *Nature*, 282(5740):677–680, Jan 1979.

[30] R.W. Eppley, E.H. Renger, and W.G. Harrison. Nitrate and phytoplankton production in southern-california coastal waters. *Limnol Oceanogr*, 24(3):483–494, Jan 1979.

[31] R.W. Eppley, E.H. Renger, W.G. Harrison, and J.J. Cullen. Ammonium distribution in southern-california coastal waters and its role in the growth of phytoplankton. *Limnol Oceanogr*, 24(3):495–509, Jan 1979.

[32] P. G. Falkowski, R. T. Barber, and V. Smetacek. Biogeochemical controls and feedbacks on ocean primary production. *Science*, 281(5374):200–206, 1998.

[33] M.J. Ferris and B. Palenik. Niche adaptation in ocean cyanobacteria. *Nature*, 396(6708):226–228, Jan 1998.

[34] P.J.S. Franks. Spatial patterns in dense algal blooms. *Limnol. Oceanogr.*, 42:1297–1305, 1997.

[35] W. R. Geyer, J. H. Trowbridge, and M. M. Bowen. The dynamics of a partially mixed estuary. *J Phys Oceanogr*, 30(8):2035–2048, 2000.

[36] R. Goericke and J.P. Montoya. Estimating the contribution of microalgal taxa to chlorophyll a in the field - variations of pigment ratios under nutrient- and light-limited growth. *Mar Ecol-Prog Ser*, 169:97–112, Jan 1998.

[37] D. Goodman, R.W. Eppley, and F.M.H. Reid. Summer phytoplankton assemblages and their environmental correlates in the southern-california bight. *J Mar Res*, 42(4):1019–1049, Jan 1984.

[38] B.S. Halpern and K. Cottenie. Little evidence for climate effects on local-scale structure and dynamics of california kelp forest communities. *Global Change Biol*, 13(1):236–251, Jan 2007.

[39] A. Hannachi, I.T. JollIffe, and D.B. Stephenson. Empirical orthogonal functions and related techniques in atmospheric science: a review. *Int. J. Climatol.*, 27:1119–1152, 2007.

[40] L.R. Haury, M.G. Briscoe, and M.H. Orr. Tidally generated internal wave packets in massachusetts bay. *Nature*, 278:312–317, 1979.

[41] K.R. Helfrich. Continuously stratified nonlinear low-mode internal tides. *J Mar Res*, 66(3):299–323, Jan 2008.

[42] K.R. Helfrich and R.H.J. Grimshaw. Nonlinear disintegration of the internal tide. *J Phys Oceanogr*, 38(3):686–701, Jan 2008.

[43] P.M. Holligan, R.D. Pingree, and G.T. Mardell. Oceanic solitons, nutrient pulses and phytoplankton growth. *Nature*, 314:348–350, 1985.

[44] P.E. Holloway. On the semidiurna; internal tide at a shelf break region on the australia north west shelf. *Jour. Phys. Ocean.*, 14(11):1787–1799, 1984.

[45] R.W. Holmes, P.M. Williams, and R.W. Eppley. Red water in la jolla bay. *Limnol. Oceanogr.*, 12(3):503, 1967.

[46] J.D. Horel. Complex principle component analysis: theory and examples. *Jour. Climate App. Metero.*, 23:1660–1673, 1984.

[47] C.H. Hsieh, S.M. Glaser, A.J. Lucas, and G. Sugihara. Distinguishing random environmental fluctuations from ecological catastrophes for the north pacific ocean. *Nature*, 435(7040):336–340, Jan 2005.

[48] M.E. Inall, T.P. Rippeth, and T.L. Sherwin. Impact of nonlinear waves on the dissipation of internal tidal energy at a shelf break. *Jour. Geophys. Res.*, 105(C4):8687–8705, 2000.

[49] J.L. Iriarte, G. Pizarro, V.A. Troncoso, and M. Sobarzo. Primary production and biomass of size-fractionated phytoplankton off antofagasta, chile (23-24 degrees s) during pre-el nino and el nino 1997. *J Marine Syst*, 26(1):37–51, Jan 2000.

[50] K.S. Johnson and L.J. Coletti. In situ ultravoliet spectrophotometry for high resolution and long-term monitoring of nitrate, bromide and bisulfide in the ocean. *Deep-Sea Res. I*, 49:1291–1305, 2002.

[51] M. Kahru, R. Kudela, M. Manzano-Sarabia, and B.G. Mitchell. Trends in primary production in the california current detected with satellite data. *Journal of Geophysical Research*, 114:C02004, Feb 2009.

[52] H.J. Kim and A.J. Miller. Did the thermocline deepen in the california current after the 1976/77 climate regime shift? *J Phys Oceanogr*, 37(6):1733–1739, Jan 2007.

[53] J.W. Krause, D.M. Nelson, and M.W. Lomas. Biogeochemical responses to late-winter storms in the sargasso sea, ii: Increased rates of biogenic silica production and export. *Deep-Sea Res Pt I*, 56(6):861–874, Jan 2009.

[54] R.M. Kudela and W.P. Cochlan. Nitrogen and carbon uptake kinetics and the influence of irradience for a red tide bloom off southern california. *Aquatic Microb. Ecol.*, 21(1):31–47, 2000.

[55] R.M. Kudela and R.C. Dugdale. Nutrient regulation of phytoplankton productivity in monterey bay, california. *Deep-Sea Res Pt Ii*, 47(5-6):1023–1053, Jan 2000.

[56] P.K. Kundu, J.S. Allen, and R.L. Smith. Modal decomposition of a velocity field near the oregon coast. *J. Phys. Ocean.*, 5:683–704, 1975.

[57] E. Kunze, L.K. Rosenfeld, G.S. Carter, and M.C. Gregg. Internal waves in monterey submarine canyon. *J Phys Oceanogr*, 32(6):1890–1913, Jan 2002.

[58] E. Kunze, L.K. Rosenfeld, G.S. Carter, and M.C. Gregg. Internal waves in the monterey submarine canyon. *J. Phys. Oceanogr.*, 32(6):1890–1913, 2002.

[59] J.L. Largier. The internal tide over the shelf inshore of cape point valley, south africa. *Jour. Geophys. Res.*, 99:10023–10034, 1994.

[60] J.R. Ledwell, D.J. McGillicuddy, and L.A. Anderson. Nutrient flux into an intense deep chlorophyll layer in a mode-water eddy. *Deep-Sea Res Pt II*, 55(10-13):1139–1160, Jan 2008.

[61] J.J. Leichter and S.L. Miller. Predicting high frequency upwelling: spatial and temporal patterns of temperature on a florida coral reef. *Cont. Shelf. Res.*, 19:911–928, 1999.

[62] J.J. Leichter, H. L. Stewart, and S.L. Miller. Episodic nutrient transport to florida coral reefs. *Limnol. Oceanogr.*, 48(4):1394–1407, 2003.

[63] J.J. Leichter, S.R. Wing, S.L. Miller, and M.W. Denny. Pulsed delivery of subthermocline water to conch reef (florida keys) by internal tidal bores. *Limnol. Oceanogr.*, 41:1490–1501, 1996.

[64] C.E. Lennert-Cody and P.J.S. Franks. Plankton patchiness in high-frequency internal waves. *Mar. Ecol. Prog. Ser.*, 186:59–66, 1999.

[65] C.E. Lennert-Cody and P.J.S. Franks. Fluorescence patches in high-frequency internal waves. *Mar. Ecol. Prog. Ser.*, 235:29–42, 2002.

[66] J. A. Lerczak and W. R. Geyer. Modeling the lateral circulation in straight, stratified estuaries. *JOURNAL OF PHYSICAL OCEANOGRAPHY*, 34(6):1410–1428, 2004.

[67] J.A. Lerczak. *Internal waves on the Southern California Shelf*. PhD thesis, University of California, San Diego, 2000.

[68] J.A. Lerczak, C.D. Winant, and M.C. Henderschott. Observations of the semidiurnal internal tide on the southern california slope and shelf. *Jour. Geophys. Res.*, 108(C3):3068, 2003.

[69] M.R. Lewis, W.G. Harrison, N.S. Oakey, D. Herbert, and T. Platt. Vertical fluxes of nitrate in the oligotrophic ocean. *Science*, 234:870–873, 1986.

[70] S. MacIntyre, K.M. Flynn, R. Jellison, and J.R. Romero. Boundary mixing and nutrient fluxes in mono lake, california. *Limnol Oceanogr*, 44(3):512–529, Jan 1999.

[71] S. MacIntyre and R. Jellison. Nutrient fluxes from upwelling and enhanced turbulence at the top of the pycnocline in mono lake, california. *Hydrobiologia*, 466:13–29, 2001.

[72] J.A. MacKinnon and M.C. Gregg. Mixing on the late-summer new england shelf - solibores, shear, and stratification. *J Phys Oceanogr*, 33(7):1476–1492, Jan 2003.

[73] A.W. Mantyla, E.L. Venrick, and T.L. Hayward. Primary production and chlorophyll relationships, derived from ten years of calcofi measurements. *CalCOFI Reports*, 36(159-166), 1995.

[74] W Martin, P MacCready, and R Dewey. Boundary layer forcing of a semidiurnal, cross-channel seiche. *J Phys Oceanogr*, 35(9):1518–1537, Jan 2005.

[75] K. Matsumoto, K. Furuya, and T. Kawano. Association of picophytoplankton distribution with enso events in the equatorial pacific between 145 degrees e and 160 degrees w. *Deep-Sea Res Pt I*, 51(12):1851–1871, Jan 2004.

[76] D.J. McGillicuddy, L.A. Anderson, N.R. Bates, T. Bibby, K.O. Buesseler, C.A. Carlson, C.S. Davis, C. Ewart, Paul G Falkowski, Sarah A Goldthwait, Dennis A Hansell, William J Jenkins, Rodney Johnson, Valery K Kosnyrev, James R Ledwell, Qian P Li, David A Siegel, and Deborah K Steinberg.

Eddy/wind interactions stimulate extraordinary mid-ocean plankton blooms. *Science*, 316(5827):1021–1026, Jan 2007.

[77] E.E. McPhee-Shaw and E. Kunze. Boundary layer intrusions from a sloping bottom: A mechanism for generating intermediate nepheloid layers. *J Geophys Res-Oceans*, 107(C6):3050, Jan 2002.

[78] E.E. McPhee-Shaw, D.A. Siegel, L. Washburn, M.A. Brzezinski, J.L. Jones, A. Leydecker, and J. Melack. Mechanisms for nutrient delivery to the inner shelf: Observations from the santa barbara channel. *Limnol Oceanogr*, 52(5):1748–1766, Jan 2007.

[79] E.E. McPhee-Shaw, R.W. Sternberg, B. Mullenbach, and A.S. Ogston. Observations of intermediate nepheloid layers on the northern california continental margin. *Cont Shelf Res*, 24(6):693–720, Jan 2004.

[80] A.F. Michaels and M.W. Silver. Primary production, sinking fluxes and the microbial food web. *Deep-Sea Res*, 35(4):473–490, Jan 1988.

[81] J.N. Moum, D.M. Farmer, W.D. Smyth, L. Armi, and S. Vagle. Structure and generation of turbulence at interfaces strained by internal solitary waves propagating shoreward over the continental shelf. *J Phys Oceanogr*, 33(10):2093–2112, Jan 2003.

[82] J.N. Moum, J.M. Klymak, J.D. Nash, A. Perlin, and W.D. Smyth. Energy transport by nonlinear internal waves. *J Phys Oceanogr*, 37(7):1968–1988, Jan 2007.

[83] M. Mullin. *Spatial and Temporal Patterns in the Southern California Bight*, pages 216–286. Plankton dynamics in the Southern California Bight. Springer Verlag, 1986.

[84] W. Munk, F. Snodgrass, and M. Wimbush. Tides off-shore: Transition from california coastal to deep-sea waters. *Geophysical Fluid Dynamics*, 1:161–235, 1970.

[85] J.D. Nash, M.H. Alford, and E. Kunze. Estimating internal wave energy fluxes in the ocean. *J Atmos Ocean Tech*, 22(10):1551–1570, Jan 2005.

[86] J.D. Nash, E. Kunze, J.M. Toole, and R.W. Schmitt. Internal tide reflection and turbulent mixing on the continental slope. *Jour. Phys. Ocean.*, 34:1117–1134, 2004.

[87] T.R. Osborn. Estimates of the local rate of vertical diffusion from dissipation measurements. *Jour. Phys. Ocean.*, 10:83–89, 1980.

[88] B. Palenik, B. Brahamsha, F.W. Larimer, M. Land, L. Hauser, P. Chain, J. Lamerdin, W. Regala, E.E. Allen, J. McCarren, I. Paulsen, A. Dufresne, F. Partensky, E.A. Webb, and J. Waterbury. The genome of a motile marine synechococcus. *Nature*, 424(6952):1037–1042, Jan 2003.

[89] J. Pineda. Predictable upwelling and the shoreward transport of planktonic larvae by internal tidal bores. *Science*, 253:548–551, 1991.

[90] R.D. Pingree and G.T. Mardell. Slope turbulence, internal waves and phytoplankton growth at the celtic sea shelf-break. *Phil. Trans. Royal Soc. London. Ser. A*, 302(1472):663, 1981.

[91] J.M. Pringle and K. Riser. Remotely forced nearshore upwelling in southern california. *Jour. Geophys. Res. Oceans*, 108(C4):3131, 2003.

[92] L. Rainville and R. Pinkel. Wirewalker: An autonomous wave-powered vertical profiler. *Jour. Atmos. Ocean. Tech.*, 18(6):1048–1051, 2001.

[93] L. Rainville and R. Pinkel. Baroclinic energy flux at the hawaiian ridge: Observations from the r/p flip. *Journal of Physical Oceanography*, 36(6):1104–1122, 2006.

[94] L. Rainville and R. Pinkel. Propagation of low-mode internal waves through the ocean. *Journal of Physical Oceanography*, 36(6):1220–1236, 2006.

[95] M. Rattray. On the coastal generation of internal tides. *Tellus*, 12(1):54–62, 1960.

[96] F.M.H. Reid, E. Stewart, R.W. Eppley, and D. Goodman. Spatial-distribution of phytoplankton species in chlorophyll maximum layers off southern-california. *Limnol Oceanogr*, 23(2):219–226, Jan 1978.

[97] J.L. Reid, G.I. Roden, and J. Wyllie. Studies of the california current system. *Cal. Coop. Fish. Rep.*, 6:28pp, Aug 1958.

[98] T.L. Richardson and G.A. Jackson. Small phytoplankton and carbon export from the surface ocean. *Science*, 315(5813):838–840, Jan 2007.

[99] T.P. Rippeth, M.R. Palmer, J.H. Simpson, N.R. Fisher, and J. Sharples. Thermocline mixing in summer stratified continenetal shelf seas. *Geophys. Res. Letters*, 32(5):L05602, 2005.

[100] D. Roemmich and J.A. Mcgowan. Climatic warming and the decline of zooplankton in the california current. *Science*, 267(5202):1324–1326, Jan 1995.

[101] L.K. Rosenfeld. *WHOI Technical Report*, 85(35):1–50, 1983.

[102] D. L. Rudnick, T. J. Boyd, R. E. Brainard, G. S. Carter, G. D. Egbert, M. C. Gregg, P. E. Holloway, J. M. Klymak, E. Kunze, C. M. Lee, M. D. Levine, D. S. Luther, J. P. Martin, M. A. Merrifield, J. N. Moum, J. D. Nash, R. Pinkel, L. Rainville, and T. B. Sanford. From tides to mixing along the hawaiian ridge. *Science*, 301(5631):355–357, 2003.

[103] D. L. Rudnick and R. A. Weller. The heat-budget in the north-atlantic subtropical frontal zone. *J Geophys Res-Oceans*, 98(C4):6883–6893, 1993.

[104] D.L. Rudnick and R.E. Davis. Mass and heat budgets on the northern california shelf. *J Geophys Res*, 93(C11):14,013–14,024, 1988.

[105] R.R. Rykaczewski and D.M. Checkley. Influence of ocean winds on the pelagic ecosystem in upwelling regions. *P Natl Acad Sci Usa*, 105(6):1965–1970, Jan 2008.

[106] H. Sandstrom and J.A. Elliott. Internal tide and solitons on the scotian shelf: a nutrient pump at work. *Jour. Geophys. Res.*, 89(C4):6415–6426, 1984.

[107] H. Sandstrom and N.S. Oakey. Dissipation in internal tides and solitary waves. *Jour. Phys. Ocean.*, 25(4):604–614, 1995.

[108] A. Scotti and J. Pineda. Plankton accumulation and transport in propagating nonlinear internal fronts. *J Mar Res*, 65(1):117–145, 2007.

[109] A.L. Shanks. Surface slicks associated with tidally forced internal waves may transport pelagic larvae of benthic invertebrates shoreward. *Mar. Ecol. Prog. Ser.*, 13:311–315, 1983.

[110] J. Sharples. Potential impacts of the spring-neap tidal cycle on shelf sea primary production. *Journal of Plankton Research*, 30(2):183–197, Jan 2008.

[111] J. Sharples, C.M. Moore, and E.R. Abraham. Internal tide dissipation, mixing, and vertical nitrate flux at the shelf edge of ne new zealand. *J Geophys Res-Oceans*, 106(C7):14069–14081, Jan 2001.

[112] J. Sharples, C.M. Moore, T.P. Rippeth, P.M. Holligan, D.J. Hydes, and N.R. Fisher. Phytoplnakton distribution and survival in the thermocline. *Limnol. Oceanogr.*, 46(3):486–496, 2001.

[113] J. Sharples, J.F. Tweddle, J. A. Mattias Green, M.R. Palmer, Y.N. Kim, A.E. Hickman, P.M. Holligan, C.M. Moore, T.P. Rippeth, J.H. Simpson, and V. Krivtsov. Spring-neap modulation of internal tide mixing and vertical nitrate fluxes at a shelf edge in summer. *Limnol Oceanogr*, 52(5):1735–1747, Jan 2007.

[114] P.E. Smith and R.W. Eppley. Primary production and the anchovy population in the southern-california bight - comparison of time-series. *Limnol Oceanogr*, 27(1):1–17, Jan 1982.

[115] H.U. Sverdrup and W.E. Allen. Distribution of diatoms in relation to the character of water masses and currents off southern california in 1938. *J Mar Res*, 2(2):131–144, Jan 1939.

[116] V. Tai and B. Palenik. Temporal variation of synechococcus clades at a coastal pacific ocean monitoring site. *ISME J*, 3(8):903–915, Jan 2009.

[117] M.J. Tegner, P.K. Dayton, P.B. Edwards, and K.L. Riser. Large-scale, low-frequency oceanographic effects on kelp forest succession: A tale of two cohorts. *Mar Ecol-Prog Ser*, 146(1-3):117–134, Jan 1997.

[118] Hayward T.L. and E.L. Venrick. Nearsurface pattern in the california current: coupling between physical and biological structure. *Deep-Sea Res. II*, 45:1617–1638, 1998.

[119] R.E. Todd, D.L. Rudnick, and R.E. Davis. Monitoring the greater san pedro bay region using autonomous underwater gliders during fall of 2006. *J Geophys Res*, 114(C6):1–13, Jun 2009.

[120] S.A. Tont. Short-period climatic fluctuations - effects on diatom biomass. *Science*, 194(4268):942–944, Jan 1976.

[121] G.M. Torgrimson and B.M. Hickey. Barotropic and baroclinic tides over the continental slope and shelf off oregon. *J Phys Oceanogr*, 9(5):945–961, Jan 1979.

[122] H.B. Torrey. An unusual occurence of dinoflagellata on the california coast. *Am. Nat.*, 36:187–192, 1902.

[123] G. Tremblay, C. Belzile, M. Gosselin, M. Poulin, S. Roy, and J.E. Tremblay. Late summer phytoplankton distribution along a 3500 km transect in canadian arctic waters: strong numerical dominance by picoeukaryotes. *Aquatic Microbial Ecology*, 54:55–70, Jan 2009.

[124] D.H. Turpin and P.J. Harrison. Limiting nutrient patchiness and its role in phytoplankton ecology. *Jour. Exp. Mar. Biol. Ecol.*, 39:151–166, 1979.

[125] L.J. Twomey, A. M. Waite, V. Pez, and C. B. Pattiaratchi. Variability in nitrogen uptake and fixation in the oligotrophic waters off the south west coast of australia. *Deep-Sea Res Pt II*, 54(8-10):925–942, Jan 2007.

[126] A. Valle-Levinson, C. Y. Li, K. C. Wong, and K. M. M. Lwiza. Convergence of lateral flow along a coastal plain estuary. *J Geophys Res-Oceans*, 105(C7):17045–17061, 2000.

[127] J.M. Wallace and R.E. Dickinson. Empirical orthogonal representation of time series in the frequency domain. part i: theoretical consideration. *Jour. Appl. Meteor.*, 11:887–892, 1972.

[128] C. D. Winant. Three-dimensional tidal flow in an elongated, rotating basin. *J Phys Oceanogr*, 37(9):2345–2362, Sep 2007.

[129] C. D. Winant. Three-dimensional residual tidal circulation in an elongated, rotating basin. *J Phys Oceanogr*, 38(6):1278–1295, Jun 2008.

[130] C.D. Winant. Internal surges in coastal waters. *Jour. Geophys. Res.*, 79(30):4523–4526, 1974.

[131] C.D. Winant. Two-layer tidal circulation in a fricitonal, rotating basin. submitted, 2009.

[132] C.D. Winant and A.W. Bratkovich. Temperature and currents in the southern california shelf: A description of the variability. *Jour. Phys. Ocean.*, 11:71–86, 1981.

[133] C.D. Winant and C.E. Dorman. Seasonal patterns of surface wind stress and heat flux over the southern california bight. *J Geophys Res-Oceans*, 102(C3):5641–5653, Jan 1997.

[134] C.D. Winant and J.R. Olson. The vertical structure of coastal currents. *Deep-Sea Res. I*, 23:925–936, 1976.

[135] A. Worden, J. Nolan, and B. Palenik. Assessing the dynamics and ecology of marine picophytoplankton: The importance of the .... *Limnol Oceanogr*, Jan 2004.

[136] C Wunsch. Progressive internal waves on slopes. *J Fluid Mech*, 35:131–144, Jan 1969.